CRYOGENIC BOILING AND TWO-PHASE CHILLDOWN PROCESS UNDER TERRESTRIAL AND MICROGRAVITY CONDITIONS

By

KUN YUAN

A DISSERTATION PRESENTED TO THE GRADUATE SCHOOL
OF THE UNIVERSITY OF FLORIDA IN PARTIAL FULFILLMENT
OF THE REQUIREMENTS FOR THE DEGREE OF
DOCTOR OF PHILOSOPHY

UNIVERSITY OF FLORIDA

2006

Copyright 2006

by

Kun Yuan

ACKNOWLEDGMENTS

First, I would like to express my greatest appreciation to my advisor, Dr. Jacob N. Chung, for his continuous support, encouragement, motivation, and guidance. Without his direction and support, this work would not have been possible.

My sincere thanks are extended to my committee members, Drs. James F. Klausner, Renwei Mei, William E. Lear, Jr., and Gary G. Ihas. Thank you for your time, encouragement, valuable advices, and wonderful classes you gave. Special thanks go to Dr. Ihas for the help on design of the experimental apparatus, and to Dr. Mei for his guidance on numerical computation.

I would also like to recognize my fellow graduate associates Renqiang Xiong, Adam Robinson, and Yun Whan Na for their kindly assistance. Special appreciation is given to Dr. Jun Liao for the interesting discussion and his helpful suggestion on code validation.

I am deeply indebted to my parents and my brother for their never-ending love, dedication, and support through my long journey of study. Finally, I would like to thank my wife Yan Ji for her continual support, encouragement, and love.

TABLE OF CONTENTS

page

LIST OF TABLES

LIST OF FIGURES

NOMENCLATURE

a	Acceleration [ms^{-2}]
A	Area [m^2]
Ca	Capillary number
C_D	Drag coefficient
CFL	Courant number
C_p	Specific heat capacity [$J\ kg^{-1}\ K^{-1}$]
d	Diameter of liquid droplets [m]
D	Diameter of the flow channel [m]
E	Liquid droplet entrainment fraction
f	Friction factor
F_D	Drag force [N]
F_L	Time averaged fraction of bottom wall surface that is associated with liquid filaments
g	Gravitational acceleration constant 9.8[ms^{-2}]
G	Mass flux [$kgm^{-2}s^{-1}$]
h	Heat transfer coefficient [$Wm^{-2}K^{-1}$]; Enthalpy [Jkg^{-1}]; Water level [m]
h_L	Liquid filament height [m]

h_{lv} latent heat of evaporation[$\mathrm{Jkg^{-1}K^{-1}}$]

h'_{lv} Latent heat plus vapor sensible heat content [$\mathrm{Jkg^{-1}K^{-1}}$]

Ja Jacob number

k Thermal conductivity [$\mathrm{Wm^{-1}K^{-1}}$]

m''_l Mass transfer rate per unit area [$\mathrm{kgm^{-2}s^{-1}}$]

m'''_l Mass transfer rate per unit volume [$\mathrm{kgm^{-3}s^{-1}}$]

Nu Nusselt number

P Pressure [Pa] ; Perimeter [m]

Pr Prandtl number

q'' Heat flux [$\mathrm{Wm^{-2}}$]

R Ridius of the flow channel [m]

R_g Gas constant

Ra Rayleigh number

Re Reynolds number

S Slip velocity; Suppression factor in flow nucleate boiling

S_2 Shock speed [$\mathrm{ms^{-1}}$]

t Time [s]

T Temperature [K]

ΔT_w wall superheat [K]

u Velocity [$\mathrm{ms^{-1}}$]

$\dot{V}$ Volume flow rate [$\mathrm{m^3s^{-1}}$]

We	Webber number
x	Quality
X_{tt}	Martinelli parameter
z	Position

Greek letters

α	Void fraction; Thermal diffusivity $[\mathrm{m^2 s^{-1}}]$
δ	Vapor film thickness $[\mathrm{m}]$
δ_0	Bottom wall vapor film thickness $[\mathrm{m}]$
ε	Emissivity
μ	Viscosity $[\mathrm{kg m^{-1} s^{-1}}]$
ρ	Density $[\mathrm{kg\ m^{-3}}]$
σ	Surface tension $[\mathrm{N\ m^{-1}}]$
σ_B	Stefen Boltzmann constant 5.67×10^{-8} $[\mathrm{W\ m^{-2} K^{-4}}]$
τ	Shear stress $[\mathrm{N\ m^{-2}}]$

Subscripts

0	Initial value
2ϕ	Two-phase
b	Bottom wall
Ber	Berenson's correlation
CHF	Critical heat flux
con	Convection

crit	Critical
d	Droplet
e	Equilibrium
evap	Evaperation
fb	Film boiling
g	Gas
i	Interfacial; Inner
in	Inlet
j	Vacuum jacket
l	Liquid phase
lh	Liquid heating
max	Maximum
min	Minimum
o	Outer
pool	Pool boiling
r	Radiation
rw	Rewet
s	Saturation
u	Upper wall
v	Vapor phase
vd	Vapor to droplet
vl	Vapor to liquid
vs	Vapor saturated

w Wall

wd Wall to droplet

wv Wall to vapor

Superscripts

" Quantity per unit area

''' Quantity per unit volume

Abbreviations

CHF Critical heat flux

DFFB Dispersed flow film boiling

QF Quenching front

IAF Inverted annular flow

IAFB Inverted annular film boiling

IHCP Inverse heat transfer problem

LOCA Loss of coolant accident

SOU Second order upwind

TDMA Tri-diagonal matrix algorithm

TVS Thermodynamic vent system

Abstract of Dissertation Presented to the Graduate School
of the University of Florida in Partial Fulfillment of the
Requirements for the Degree of Doctor of Philosophy

CRYOGENIC BOILING AND TWO-PHASE CHILLDOWN PROCESS UNDER TERRESTRIAL AND MICROGRAVITY CONDITIONS

By

Kun Yuan

August 2006

Chair: Jacob N. Chung
Major Department: Mechanical and Aerospace Engineering

Chilldown or quenching is a complicated process that initiates the cryogenic fluids transport, and it involves unsteady two-phase heat and mass transfer. To advance understanding of this process, we conducted both experimental and modeling investigations.

An experimental apparatus was designed and fabricated to investigate the cryogenic chilldown process under both 1-g and microgravity conditions. Liquid nitrogen was used as the working fluid. We found that the chilldown process can be generally divided into three regions: film boiling region, transition boiling region and nucleate boiling region, and each region is associated with a different flow regime and heat transfer mechanism.

Under low flow conditions, we observed that the two-phase flow regime is dispersed flow in the film boiling region. The dispersed liquid phase is in the form of long filaments as the tube is chilled down, and the vapor phase is generally superheated. Statistic feature of the liquid filaments was studied and a phenomenological model, in which the heat transfer at the bottom is considered as a sum of vapor and liquid components, was developed.

Microgravity tests were conducted for chilldown in the film boiling region. Bottom wall heat flux was found to decrease under microgravity condition. Under current experimental conditions, the gravity effect does not show a strong dependence on wall temperature and inlet flow rate.

A cryogenic chilldown model was also developed. The model focuses on both vertical tube chilldown and microgravity chilldown. In this model, the chilldown process is characterized as four distinct regions, which are fully vapor region, dispersed flow film boiling region, inverted annular film boiling region, and nucleate boiling region. Two-fluid equations were applied to the dispersed flow film boiling region and the inverted annular film boiling region, while the fully vapor region and nucleate boiling region are depicted by single-phase correlations. The model results show a good agreement with previous experimental data.

CHAPTER 1
INTRODUCTION

Cryogenic fluids are widely used in industrial, aerospace, and cryosurgery systems and so on. In these systems, proper transport, handling and storage of cryogenic fluids are of great importance. The chilldown or quenching process which initiates cryogenic fluids transport is complicated, involving unsteady two-phase heat and mass transfer, and was not fully understood until now. Cryogenic chilldown shares many common features with other industrial processes such as the reflooding process, which is often encountered in Pressurized Water Reactors (PWR) and Boiling Water Reactors (BWR). Therefore, further knowledge of the cryogenic chilldown process may be applicable to those processes also.

In this study, we experimentally investigated the cryogenic two-phase chilldown process under terrestrial and microgravity conditions, and a numerical model was also developed to predict the chilldown process.

1.1 Research Background

One important application of cryogenic fluids is in space exploration. Efficient and safe use of cryogenic fluids in thermal management, power and propulsion, and life-support systems of a spacecraft during space missions involves transport, handling, and storage of these fluids under both terrestrial and microgravity conditions. Uncertainties about the flow regime and heat transfer characteristics pose severe design concerns. Moreover, the thermo-fluid dynamics of two-phase systems in microgravity encompass a wide range of complex phenomena that are not understood sufficiently for engineering design to proceed.

Cryogenic fluids are also widely used in industrial systems. Until the early 1970s, liquid hydrogen was mainly used by NASA as a rocket fuel; however, development and growth of commercial markets have since outpaced this use. For example, liquid hydrogen is used in industrial applications such as metal processing, plate glass production, fat and oil hardening, semiconductor manufacturing, and pharmaceutical and chemical manufacturing. Today, the commercial market is many times larger than the government market.

For any process using cryogenic fluids, chilldown is inevitably the initial stage; therefore, efficiency of the chilldown process is a significant concern since the cryogen used to cool down the system is not utilized for propulsion, power generation or other applications. In a hydrogen economy, chilldown must be accomplished with a minimum consumption of cryogen for the overall energy efficiency to be within tolerable limits.

Current understanding on chilldown process is, however, very limited. For example, there is considerable disagreement over the chilldown heat fluxes and whether a unique rewetting temperature exists (Dhir et al. 1981; Piggott and Porthouse 1975). For similar experimental observations, quite different explanations were also suggested by different researchers. For example, it was reported that the rewetting velocity increased with increasing inlet flow rate, given the same initial wall temperature (Yamanouchi 1968; Duffey and Porthouse 1973). Duffey and Porthouse (1973) suggested that this flow rate effect is resulted from increasing the wet side heat transfer coefficient with higher inlet flow. This improves the rate of axial heat conduction and hence leads to a faster rewetting rate. Thompson (1974), however, argued that the inlet flow rate affects precooling on the dry side rather than the heat transfer in the wet side.

Another driven force of present investigation comes from the need for further understanding of the cryogenic chilldown process under low mass flux in a thermodynamic vent system (TVS) on spacecrafts. A TVS is a system where a small amount of liquid is withdrawn from a cryogenic propellant tank and vented to remove heat from the bulk liquid cryogen in the tank and thus lower the tank pressure (Lin et al. 1991; Van Dresar et al. 2001, 2002). The mass flux in TVS system is generally very low. Systematic experiments for steady state low mass flux cryogenic two-phase flow were conducted by Van Dresar et al. (2001, 2002), the highly transient chilldown process was, however, not included.

1.2 Research Objectives

For liquid hydrogen to be adopted as a routine fuel, the chilldown process must be fundamentally understood. The objective of the experimental investigations in this research work is to seek a fundamental understanding on the boiling regimes, two-phase flow regimes, and heat transfer characteristics for chilldown in pipes under both terrestrial and microgravity conditions. Further more, a cryogenic chilldown model is to be developed based on the experimental observations and will contribute to the prediction of the chilldown process.

1.3 Scope

In Chapter 2, background of boiling heat transfer, two-phase flow pattern and heat transfer regime is briefly introduced. Then previous experimental works for two-phase flow, chilldown and microgravity boiling are reviewed, followed by a short discussion of the two-phase flow modeling.

In Chapter3, the experimental system, experimental conditions, and experimental procedure for current study are introduced. The uncertainties of the data measurements are evaluated. The design and working conditions of the drop tower, which is used to provide the microgravity condition, are also given.

Chapter 4 presents the ground test results of cryogenic chilldown process. Visualized flow regimes and heat transfer data with different mass fluxes are discussed. A phenomenological model is developed based on the experimental observation.

Chapter 5 gives the experimental results of cryogenic two-phase chilldown under microgravity condition.

In Chapter 6, a two-fluid cryogenic chilldown model is developed for both microgravity chilldown and vertical tube chilldown. Four regions of the chilldown process, namely the fully vapor region, dispersed flow film boiling region, inverted annular film boiling region, and nuclear boiling region, are included in this model.

Chapter 7 concludes the research with a summary of the overall work and suggests future works.

CHAPTER 2
BACKGROUND AND LITERATURE REVIEW

Cryogenic chilldown involves complex interaction of energy and momentum transfer among the two phases and the solid wall. Understanding of the boiling phenomenon, flow regime and heat transfer regime provides foundation for further insight into this dynamic process. This chapter gives background information of boiling, two-phase flow regime and heat transfer regime. Previous works on both experimental and modeling part that related to chilldown and microgravity boiling are reviewed and qualitatively assessed.

2.1 Background

2.1.1 Boiling Curve

A boiling curve shows the relationship between the heat flux that the heater supplies to the boiling fluid and the heater surface temperature. According to the typical boiling curve (Figure 2-1), a chilldown (quenching) process usually starts from point E, and then goes towards point D in the film boiling regime as the wall temperature decreases. Point D is called the Leidenfrost point which signifies the minimum heater temperature required for the film boiling. For the film boiling process, the wall is so hot that liquid will vaporize before reaching the heater surface which causes the heater to be always in contact with vapor. When cooling beyond the Leidenfrost point, if a constant heat flux heater was used, then the boiling would shift from film to nucleate boiling (somewhere between points A and B) directly with a substantial decrease in the wall temperature because the transition boiling is an unstable process.

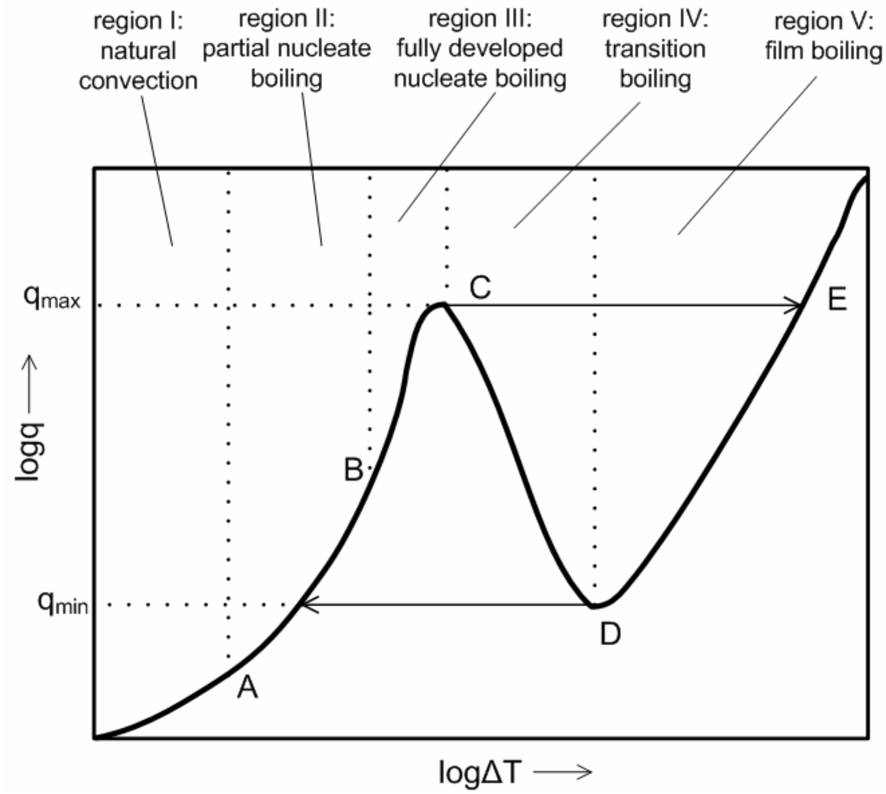

Figure 2-1. Typical boiling curve.

2.1.2 Two-Phase Flow Regimes and Heat Transfer Regimes

The flow in cryogenic chilldown process is typically two-phase flow, because the wall temperature usually exceeds the liquid boiling temperature to several hundred Celsius in the beginning. The topology of two-phase flow has an important effect on heat transfer and pressure drop in the flow channel. Therefore, generally the first step in two-phase flow experiment or modeling is to determine the two-phase flow regime. Commonly observed flow regimes in horizontal tubes are shown in Figure 2-2.

General descriptions of the two-phase flow regimes can be referred from Carey (1992) and Van Dresar and Siegwarth (2001). Flow regimes of common two-phase flow such as air-water have been extensively mapped from experiments. However, the published data for cryogens are limited.

It is also noted that definitions of the flow regimes are somewhat arbitrary. Qualitative assessment has not been done yet, and transition criteria between different flow regimes are not fully understood.

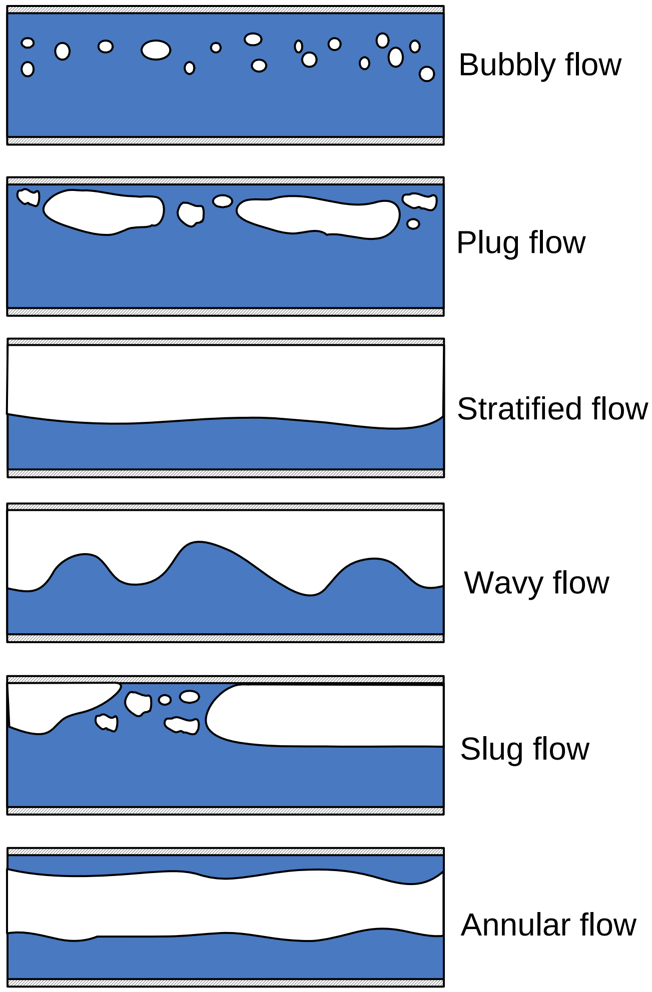

Figure 2-2. Two-phase flow regimes inside a horizontal tube.

Different flow regimes are often associated with different heat transfer regimes. When phase change occurs as two-phase mixture flows along the channel, as that encountered in chilldown process, the situation is even more complicated (Carey 1992): different flow regimes are generally observed at different positions along the channel length. The sequence of flow regimes will primarily depend on the flow rate, channel orientation, fluid properties, and wall heat flux.

Some general information could be drawn from the findings of reflooding experiments designed for hypothetical loss-of-coolant accident (LOCA) in nuclear reactors, for example, Chan and Banerjee's result for horizontal tube (1981a, b, c) and Cheng et al.'s work for vertical tube (1978).

When the two-phase flow first enters the hot tube, the liquid phase evaporates very quickly and forms a vapor film that separates the liquid phase from touching the tube wall, and the two-phase flow is in film boiling state. Depends on the local quality and other thermo-hydraulic parameters, the flow regime can be dispersed flow or inverted annular flow. The corresponding heat transfer regime will be dispersed flow forced convection, which is also called dispersed flow film boiling (DFFB) in literature (Yadigaroglu et al. 1993; Andreani and Yadigaroglu 1996; Hammouda et al. 1997; Shah and Siddiqui 2000), or inverted annular film boiling (IAFB).

As the wall temperature decreases under certain degree, the liquid phase is able to contact the tube wall. The liquid-wall contacting front, which is often referred as quenching front (QF) or sputtering region, is characterized by violent boiling associated with significant wall temperature decrease, and propagates downstream with the flow. The heat transfer mechanism at the QF is transition boiling, which is more effective than the film boiling heat transfer. This establishment of liquid-wall contact is called rewetting phenomenon and has been a research interest for several decades.

After the QF, nucleate boiling heat transfer dominates. For vertical tube, the flow regime can be annular flow, slug flow or bubbly flow; for horizontal tube, the flow regime is generally stratified flow. With further wall temperature decrease, the nucleate boiling stage gradually changes to pure convection until the wall temperature reaches the steady state, which denotes the end of the chilldown process.

2.1.3 Gravity Effect

Because of the differences in density and inertia, the two phases in two-phase flow are usually non-uniformly distributed across the pipe under terrestrial condition. The absence of gravity has important effects on flow regimes, pressure drop, and heat transfer of the two-phase flow. Surface-tension-induced forces and surface phenomena are likely to be much more important in space than they are on earth. Actually, all flow-regime-specific phenomena will be influenced by gravity level. As an example, Figure 2-3 compares the flow regime under both terrestrial and microgravity conditions; the difference is obvious.

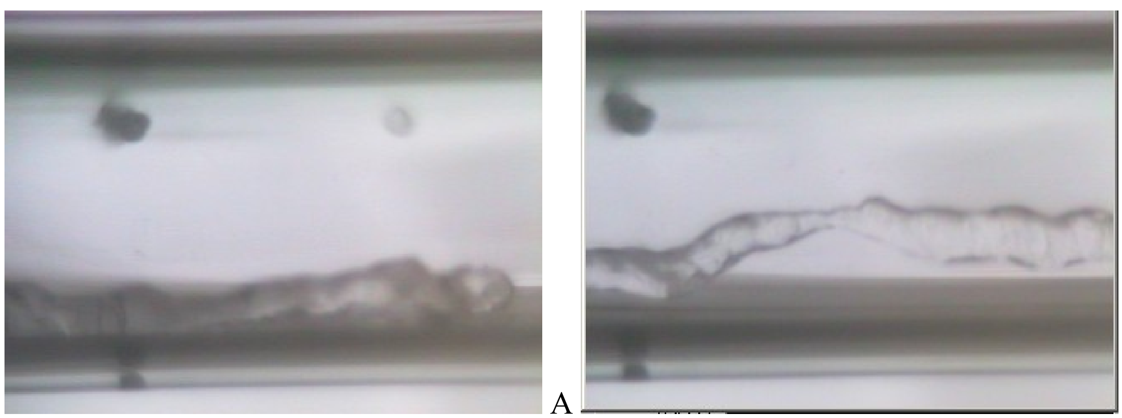

A B

Figure 2-3. Gravity effect on flow regimes. A) Flow regime in 1-g test. B) Flow regime in microgravity test.

Following is a simple scaling analysis that examines the gravity effects. For annular flow film boiling in a horizontal tube, the effect of gravity is assessed based on the ratio of Gr/Re^3, where Gr is the Grashof number and Re is the Reynolds number. The gravity effect is measured by the natural convection contribution characterized by the Gr, while the forced convective film boiling is scaled by the Reynolds number. According to

Gebhart et al. (1988), Re^3 is used in the denominator when the flow is perpendicular to gravity for a horizontal tube. Re^2 is used when the flow is in the same direction of gravity. All the thermal properties are those of vapor because of film boiling. Figure 2-4 shows this ratio with the vapor flow velocity range of 0-0.5 m/s and a ΔT of 100 °C for the Gr estimation.

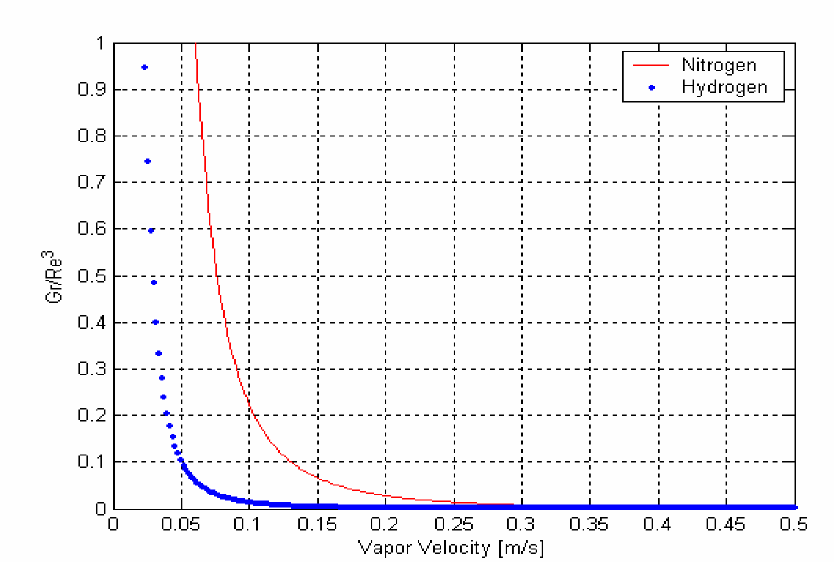

Figure 2-4. Scaling analysis of gravity effects on two-phase flow.

Based on Figure 2-4, if the vapor velocity is greater than 10 cm/s, then the Gr/Re^3 is less than 0.2. The natural convection is negligible for Gr/Re^3 less than 0.225 according to Gebhart et al. (1988). Therefore, a terrestrial gravity experiment with the vapor velocity greater than 10 cm/s would provide results that mimic the microgravity phenomenon.

2.2 Literature Review

Cryogenic two-phase flow and chilldown process is a complex problem for the scientific community to solve. The following summarizes the previous accomplishments on both experimental and modeling aspect.

2.2.1 Experimental Studies

2.2.1.1 Terrestrial cryogenic boiling and two-phase flow experiments

Numerous studies of cryogenic boiling in 1-g environment were conducted in the 1950s and 1960s. Brentari et al. (1965) gave a comprehensive review of the experimental studies and heat transfer correlations. For the fluids of oxygen, nitrogen, hydrogen and helium, it was found that for pool boiling, the Kutateladze (1952) correlation had the greatest reliability for nucleate boiling, while the Breen and Westwater (1962) correlation was best for film boiling. Maximum nucleate flux data were reasonably well predicted by the Kutateladze (1952) correlation. Although these correlations were selected as the best available, neither has particularly good agreement with experimental data. For the case of forced convection boiling, Brentari et al. (1965) reported that no correlation was found to be distinctly better. Some simple predictive methods were found to work as well as more complex schemes. In all boiling cases, it was questioned as to whether or not the predictive correlations include all of the significant variables that influence the boiling process. In particular, it was suggested that more detailed and better controlled experiments are needed and that more attention to surface and geometry effects is required.

Another comprehensive review of cryogenic boiling heat transfer addressing hydrogen, nitrogen and oxygen is given by Seader et al. (1965). It was reported that nucleate pool boiling results cannot be correlated by a single line but cover a range of temperature difference for a given heat flux. The spread is attributed to surface condition and geometry, and orientation. Maximum heat flux can be reduced by about 50% when going from 1-g to near 0-g. Seader et al. (1965) reported a fair amount of data for film pool boiling. Film boiling heat flux is reduced considerably at near 0-g conditions. Only a very limited amount of data is available for subcooled or saturated forced convective boiling and few conclusions were drawn. The lack of data for cryogenic forced convective boiling was also reported by Brentari and Smith (1965).

Relatively recent correlations have been published for 1-g saturated flow boiling of cryogens (Shah 1984; Gungor and Winterton 1987; Klimenko et al. 1989; Kandlikar 1990; Van Dresar et al. 2002) using the Convection number Co, Boiling number Bo and Froude number Fr as correlating parameters. Klimenko et al. (1989) investigated the effects of tube diameter and orientation on two-phase nitrogen flow and concluded that in vertical channels diameter effect was revealed in a transition from convective to less intensive nucleate boiling when the Froude number of a mixture Fr_m decreases from 40 to 10. On the contrary, in horizontal non-stratified flow, the reduction of the Fr_m number was accompanied by cross-section averaged heat transfer coefficient incensement of 20-30% in the nucleate boiling region. With $Fr_m \geq 40$, the geometry and orientation did not affect the heat transfer coefficient. Van Dresar et al. (2001) experimentally studied the near-horizontal two-phase flow of nitrogen and hydrogen. Unlike most of the other works which based on turbulent liquid flow, their work focused on laminar liquid flow and the results for low mass and heat flux flow were correlated with Froude number.

2.2.1.2 Terrestrial chilldown experiments

Research on cryogenic chilldown began in the 1960s with the development of rocket launching systems. Burke et al. (1960) studied the chilldown process of stainless-steel transfer lines of 60, 100 and 175 ft long with a 2.0 in. OD. The transfer lines were quenched by flowing liquid nitrogen. A sight glass was located near the discharge end for flow phenomena observation. Based on the wall temperature, liquid flow rate, and the observation, the chilldown process was simply divided into three stages: gas flow, two-phase flow and liquid flow. However, the flow regime information was lack in the experiments; moreover, the averaged wall temperature was used in their study. While other researchers (Bronson et al. 1962) pointed out that circumferential temperature gradient could be very large in cryogenic chilldown process. Early visualized study of flow regimes in a horizontal pipe during chilldown can be retrospect to Bronson et al. (1962). A 50 ft long with $1\frac{3}{8}$ in. ID test section was quenched by liquid hydrogen in this work. Results showed that the stratified flow is prevalent in the cryogenic chilldown process. Based on their experiments, rudimental models (Burke et al. 1960; Bronson et al. 1962) were also suggested to calculate chilldown time. Differences in flow regimes were not considered in these models; instead a gross effect was used. The work of both Burke et al. (1960) and Bronson et al. (1962) based on extremely long transfer lines, it is doubtful that their results can be applied over a short tube.

Chi and Vetere (1964) studied the chilldown process of hydrogen flowing through a 2-ft long thin wall copper tube. Thermocouples were installed on the outside wall and in the center of the tubing to measure the wall and stream temperatures at both the inlet and the outlet of the test section. The thermocouple beads in the center of the tubing were treated as control volume and their responses were used to identify different flow regimes. Chi and Vetere (1964) found that the void fractions were much larger, more than five times in some cases, than those given by previous investigators (Wright and Walters 1959; Hsu and Graham 1963). They attributed this difference to the effect of non-equilibrium nature of the chilldown process and concluded that thermodynamic equilibrium cannot exist in film boiling and transition regimes during chilldown. Another research work by Chi (1965) used several 26-in long aluminum tubes with $3/16$-in ID and ODs from $1/2$ to 2 inch. Unlike the thin wall copper tubing experiments (Chi and Vetere 1964), the temperature responses showed that slug flow was not observed until the aluminum test sections were almost cooled down, and the dominant flow regime was mist flow.

As mentioned before, chilldown of a hot surface or tube is of fundamental importance for the re-establishment of normal and safe temperature level following dryout in a LOCA in nuclear reactors. Liquid water or common refrigerant are usually used in this type of experiments. For example, Chan and Banerjee (1981a, b, c) and later Abdul-Razzak et al. (1992) used water to chilldown a preheated horizontal tubes. In their experiments, the chilldown process was divided into three regions, namely film boiling region, partially quenched region and totally quenched region. Different heat transfer mechanisms were involved in different regions.

Kawaji et al. (1985) experimentally investigated the chilldown process inside a vertical tube with different flow rates. Their results showed that for high flow rate, the entering liquid will initially boil through film boiling mechanism and then develop into inverted annular flow, dispersed flow and fully vapor flow, for low flow rate, the corresponding sequence was saturated boiling, annular flow, dispersed flow and fully vapor flow.

Recently, Velat (2004) experimentally studied the cryogenic chilldown in a horizontal pipe using nitrogen as working fluid. Pyrex glass tube with vacuum jacket was used for visualization. The flow regimes were recorded by high speed camera. Wall temperature histories and pressure drop along the pipe were recorded and associated with the visualized images.

2.2.1.3 Reduced gravity boiling and two-phase flow experiments

Because of the experimental difficulties there are very little heat transfer data for cryogenic flow boiling in reduced gravity. We were able to find just one report done by Antar and Collins (1997) investigated the cryogenic flow boiling in low gravity condition. The experimental results of two-phase flow under reduced gravity conditions using regular working fluids, such as R113, are also summarized here.

Adham-Khodaparast et al. (1995) investigated the flow film boiling during quenching of a hot flat surface with R-113. Micro-sensors were used to record instantaneous heat flux and heater surface temperature. They reported lower heat transfer rates during microgravity as compared to normal gravity and contributed that to thickening of the vapor layer. The wall superheat and the surface heat flux at the onset of rewetting and the maximum heat flux were found to increase with the inlet liquid subcooling, mass flux and gravity level. The effect of gravity was determined to be more important for low flow rates and less relevant for high flow rates. The two-phase flow regimes were not reported in their work.

Another quenching test under microgravity was done by Westbye et al. (1995). A hot thin-walled stainless steel tube was quenched by injection of subcooled R113 into the tube under both 1-g and microgravity conditions. The injection mass flux was 160-850 kg/m^2s. It was found that the rewetting temperatures were 15^0C-25^0C lower in microgravity than those obtained in 1-g, and the film boiling heat transfer coefficients in microgravity were less than those in 1-g tests. This resulted in much longer cooling periods in microgravity. It was also reported that once the tube was cooled sufficiently to allow axial propagation of the QF, the rewetting velocity was slightly greater in microgravity. The nucleate and transition boiling curves under microgravity were reported to be shifted to lower wall superheats as compared to 1-g results.

Antar and Collins (1997) reported cryogenic chilldown process under 1-g condition and on board a KC-135 aircraft. They observed that a sputtering leading core followed by a liquid filament annular flow regime. This flow regime is composed of a long and connected liquid column that is flowing in the center of the tube and is surround by a thick vapor layer. They attributed the filamentary flow to the lack of difference in the speed of vapor and liquid phases. On the heat transfer side, they reported that the quench process was delayed in low gravity and the tube wall cooling rate was diminished under microgravity conditions. The QF speed was found to be slower under the low gravity conditions.

2.2.2 Modeling of Chilldown Process

Mainly two types of flow models were developed for chilldown process modeling. Homogeneous model treats the two-phase mixture as homogeneous fluid, while two-fluid model considers the difference of the two phases and solves the equations for the conservation of mass, momentum and energy for each phase.

2.2.2.1 Homogeneous model

The primary assumptions of the homogeneous model are: (1) the fluid, either single-phase or two-phase mixture is homogeneous; (2) incompressible flow; (3) one-dimensional flow; (4) thermal equilibrium exists between the two phases.

Burke et al. (1960) developed a crude chilldown model based on their experiments of quenching large cryogenic piping system. The model was one-dimensional and the entire transfer line was treated as a single control volume. This lumped system provided a simple estimation of chilldown time but lacked accuracy due to its broad assumptions and averaging of fluid properties and flow rates over the chilldown time. Bronson et al. (1962) developed a one-dimensional model by assuming constant wall-to-coolant temperature difference along the entire transfer line. This model was used to estimate the chilldown time, however, it did not permit the estimation of the instantaneous wall and bulk fluid temperature. Chi (1965) developed an analytical model for mist-flow-dominated chilldown based on the assumptions of constant flow rate, constant heat transfer coefficient, constant fluid properties, homogeneous flow and film-boiling-dominated heat transfer. Steward et al. (1970) modeled chilldown numerically using a finite difference formulation of the one-dimensional, unsteady mass, momentum and energy equations. Cross et al. (2002) used the homogeneous model to solve three chilldown cases with hydrogen as the working fluid: the first case got a simplified analytical solution; the second case treated superheated vapor flow and the third case modeled the initially subcooled liquid flow.

In LOCA research, a so-called conduction controlled model was used by many researchers. By assuming constant wet front speed and introducing coordinate transformation, the main focus in conduction controlled model was shifted to solve the steady state conduction equation of the tube wall within a moving reference frame.

The conduction controlled model was first studied by Yamanouchi (1968). The phenomenon was described by one-dimensional quasi-steady heat conduction in a wall with two distinct regions. The region covered by the liquid film had a constant heat transfer coefficient, while the bare region was adiabatic. The major flaw of this model is the absence of the sputtering region and this leads to unreasonable heat transfer coefficient. Thompson (1972) suggested the liquid film can be characterized by a temperature-dependent nucleate boiling heat transfer coefficient, and numerically solved the two-dimensional heat conduction equation. However, the sputtering region and the film boiling region were still not considered distinctively. Sun et al. (1974) was the first one to distinguish and attribute different heat transfer coefficient to these two different regions. In their model, the one-dimensional heat conduction equation was solved analytically. Figure 2-5 schematically compares the above three models. Tien and Yao (1975) further developed the conduction controlled model to two-dimensional and analytically solved the limiting cases for both small and large Peclet numbers.

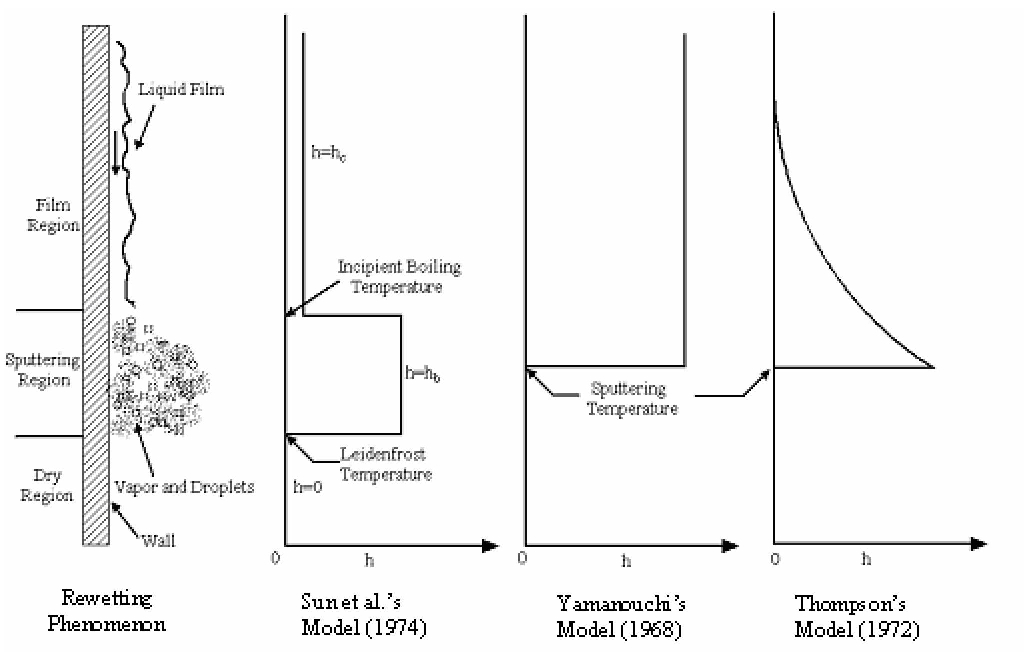

Figure 2-5. Different conduction controlled models.

2.2.2.2 Two-fluid model

Although homogeneous model is simple and has gained success in certain applications, its drawback is obvious: it can not describe the thermal and hydraulic differences between the two phases. In the homogeneous model, it is assumed that thermal equilibrium exists between the two phases, however, for IAFB and DFFB in chilldown process the vapor phase is generally superheated (Chen et al. 1979; Guo et al. 2002; Tian et al. 2006). The vapor superheat can up to several hundred Kelvin under some operating conditions. In that situation, predictions by homogeneous model will inevitably lead to large discrepancy from the experimental results. Moreover, for stratified two-phase flow, the homogeneous assumption is not valid. Therefore, the homogenous model is generally not applicable to horizontal pipe chilldown.

In engineering applications, usually only the averaged quantities are of engineering interest. Thus one of the main approaches for two-phase flow modeling is to average the local instantaneous conservation equations, while the information lost in the averaging process is supplied in the form of auxiliary relationships. This leads to the two-fluid model or separated flow model (Ishii 1975; Banerjee and Chan 1980; Ardron 1980; Ishii and Mishima 1984). Two-fluid model consists of two sets of conservation equations for the mass, momentum and energy of each phase. Since the averaged fields of one phase are not independent of the other phase, interaction terms appear in the field equations as source terms. For most practical applications, the model can be simplified to the following forms (Ishii and Mishima 1984):

Continuity equation:

$$\frac{\partial \alpha_k \rho_k}{\partial t} + \nabla \cdot \left(\alpha_k \rho_k \mathbf{v}_k \right) = \Gamma_k \tag{2.1}$$

Momentum equation:

$$\begin{aligned} &\frac{\partial \alpha_k \rho_k \mathbf{v}_k}{\partial t} + \nabla \cdot \left(\alpha_k \rho_k \mathbf{v}_k \mathbf{v}_k \right) = -\alpha_k \nabla p_k + \nabla \cdot \alpha_k \left(\overline{\overline{\tau}}_k + \tau_k^t \right) \\ &+ \alpha_k \rho_k \mathbf{g} + \mathbf{v}_{ki} \Gamma_k + \mathbf{M}_{ik} - \nabla \alpha_k \cdot \tau_i \end{aligned} \tag{2.2}$$

Enthalpy energy equation:

$$\frac{\partial \alpha_k \rho_k H_k}{\partial t} + \nabla \cdot \left(\alpha_k \rho_k H_k \mathbf{v}_k \right) = -\nabla \cdot \alpha_k \left(\overline{\overline{q}}_k + q_k^t \right)$$
$$+\alpha_k \frac{D_k}{Dt} p_k + H_{ki} \Gamma_k + q''_{ki} / L_s + \Phi_k \tag{2.3}$$

Here the subscribe k denotes k-phase and i stands for the value at the interface. L_s denotes the length scale at the interface. Γ_k, $\mathbf{M}_{ik}$, τ_i, q''_{ki} and Φ_k are the mass generation, generalized interfacial drag, interfacial shear stress, interfacial heat flux and dissipation, respectively. These interfacial transfer terms should obey the balance laws at the interface given as:

$$\left.\begin{aligned} &\sum_k \Gamma_k = 0 \\ &\sum_k \mathbf{M}_{ik} = 0 \\ &\sum_k \left(\Gamma_k H_{ki} + q''_{ki} / L_s \right) = 0 \end{aligned}\right\} \tag{2.4}$$

Chan and Banerjee (1981a, b, c) developed a two-fluid model for horizontal chilldown process based on the experimental results of quenching a hot Zircaloy-2 tube, and pointed out that the propagation of the QF was largely controlled by hydrodynamic mechanisms instead of by conduction mechanism. The model was one-dimensional and the vapor phase was assumed to be at saturated temperature. The occurrence of rewetting at the bottom of the tube was evaluated based on studying of the Kelvin-Helmholtz instability at the vapor film-liquid interface in the film boiling region. The results agreed reasonably well with experimental data. Later, a new rewetting criterion based on vapor film collapse was added into the horizontal two-fluid chilldown model by Abdul-Razzak et al. (1993).

For vertical tube, Kawaji and Banerjee (1987, 1988) employed the two-fluid model to predict the thermo-hydraulic criteria for the bottom reflooding problem in steam-water system. Their model was further developed by Hedayatpour et al. (1993) to model the chilldown mechanism in a vertical tube with four distinct regimes: fully liquid, inverted annular flow (IAF), dispersed flow and fully vapor flow. The IAF, which comprised of a liquid core surrounded by a vapor film next to the tube wall, was considered as immediately downstream of the quench front. The two-fluid model was used in the IAF and dispersed flow regimes. A one-dimensional energy equation was formulated for predicting the temperature history of the tube wall. The model was consistent with the experimental results. The major drawback of this approach was the requirement of knowing both the flow pattern as well as the QF speed.

Recently, Liao (2005) did a comprehensive study in modeling the cryogenic pipe chilldown and achieved good agreement with the experimental data. Three models were used for different situations. A simple homogeneous model was suggested for simulating vertical pipe chilldown. A pseudo-steady chilldown model, which is similar to conduction-controlled model to some extent, was developed to simulate horizontal chilldown. Coordinate transformation was introduced to eliminate the transient term and resulted in a two-dimensional parabolic equation. By assuming constant wet front speed, the main emphasis was to model the heat transfer coefficients for the stratified flow and the thermal field within the solid pipe. Correlations for film boiling and forced convection boiling were used for different flow regimes. The study showed that the current film boiling correlations are not appropriate for the cryogenic pipe chilldown due to neglecting the information of the flow regime, and a new film boiling correlation was proposed. The predicted pipe wall temperature history matched well with the experimental results. To include the prediction of the flow fields, a more comprehensive two-fluid model was also developed and combined with three-dimensional heat conduction in the solid wall to study the stratified flow regime in a horizontal pipe. The predicted wall temperature variations showed good agreement with the experimental measurements.

CHAPTER 3
EXPERIMENTAL SYSTEM

To investigate the cryogenic chilldown process, a cryogenic two-phase flow experimental facility has been designed, fabricated and tested under both terrestrial and microgravity conditions. A drop tower is used to provide the microgravity condition. The experimental system, experimental condition and procedure are introduced in this chapter.

3.1 Experimental Setup

3.1.1 System Overview

Most two-phase flow experimental apparatus are designed as a close loop. The vapor phase is usually cooled back to liquid through the condenser and then sent back into the loop. However, the close loop design is not suitable for current cryogenic two-phase flow experiment. The reasons are first the boiling temperatures of the cryogens are extremely low, to condense the vapor phase back to liquid phase, special cryocooler must be used, and this will highly increase the complicity of the system; secondly no common commercial pump can work at the cryogenic temperature and using cryogenic pump is not economically possible.

Considering the above reasons, the experimental system is designed as a once-through flow pass using motor-driven bellows as flow generator. Figure 3-1 shows the schematic of the experimental system, which locates in two side-by-side aluminum cubicles and is fabricated for both terrestrial and microgravity experiments. The experimental system mainly consists of a nitrogen tank, a motor-driven bellows, test section inlet portion, test section, test section outlet portion, vacuum jacket, vacuum pump, data acquisition system, lighting and video system. A photographic view of the apparatus is shown in Figure 3-2.

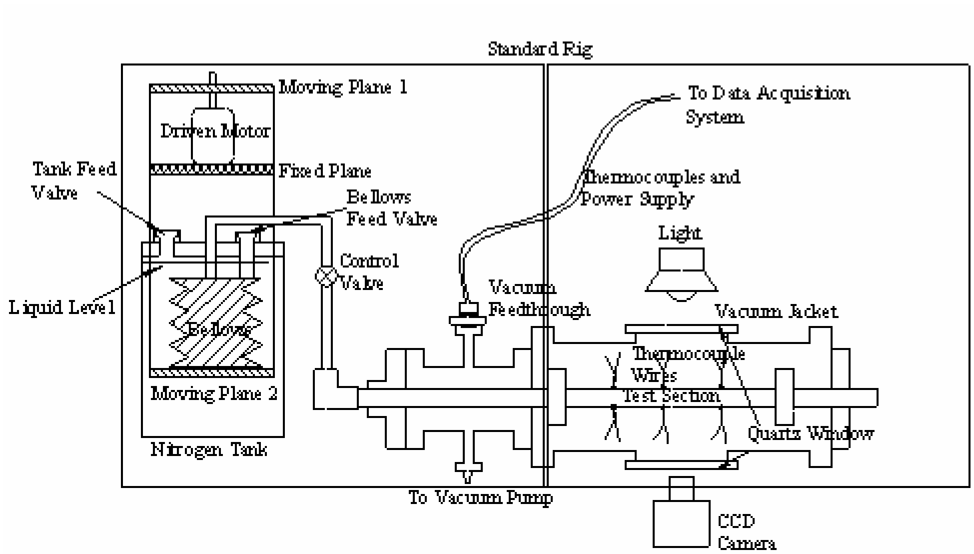

Figure 3-1. Cryogenic boiling and two-phase flow test apparatus.

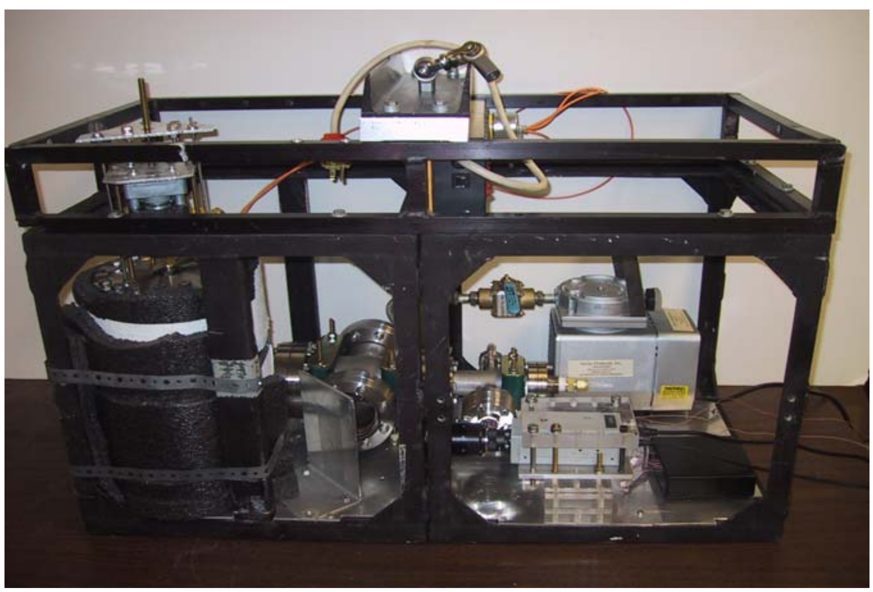

Figure 3-2. Photographic view of cryogenic boiling and two-phase flow test apparatus.

Nitrogen flow is generated by a motor-driven stainless steel bellows. The test section is transparent. Temperature measurements are taken at different downstream locations along the test section when the two-phase nitrogen flow is passing through; video images are also recorded simultaneously.

3.1.2 Flow Driven System

Following the traditional method to control cryogenic flow (Swanson et al. 2000), nitrogen flow is generated by a motor-driven stainless steel bellows (Figure 3-3). The basic idea is using a constant speed motor to pull a moving plate which is attached to the bottom of a bellows filled with liquid nitrogen. Therefore, a constant volumetric flow rate can be achieved when the motor is turned on.

The bellows used in the experiment is made by thin-wall stainless steel. It has an OD of 4.0 inch and a free length of about 7.5 inch. The bellows is inside of a stainless steel tank, which has an OD of 6.75 inch, ID of 6.35 inch and inner depth of 10.24 inch. A stainless steel flange is fabricated as the tank cap and a copper O-ring is used to seal between the tank and the cap. There are two opening on the tank cap, one for feeding liquid nitrogen to the tank and the other for feeding the bellows. After assembling, the bellows is at the lower part of the tank, so that the liquid nitrogen in the tank will flow into the bellows when the tank liquid level is high enough, therefore, a full tank will be a sufficient condition for the bellows is also full and immersed in liquid nitrogen. The experimental time is usually only several minutes, during which only a little amount of the liquid nitrogen surrounds the bellows will be boiled off, and it is assumed that the flow from the bellows is pure liquid at saturation temperature.

A stainless steel connector welded with a valve is designed and fabricated to assemble the bellows to the tank cap. The valve is used to fill the bellows and will be closed manually when the bellows is full. Copper O-ring and Teflon gasket seal are adopted at top and bottom of the connector, respectively. The bottom of the bellows is attached to an aluminum plate. The top of the bellows is stationary while the bottom travels.

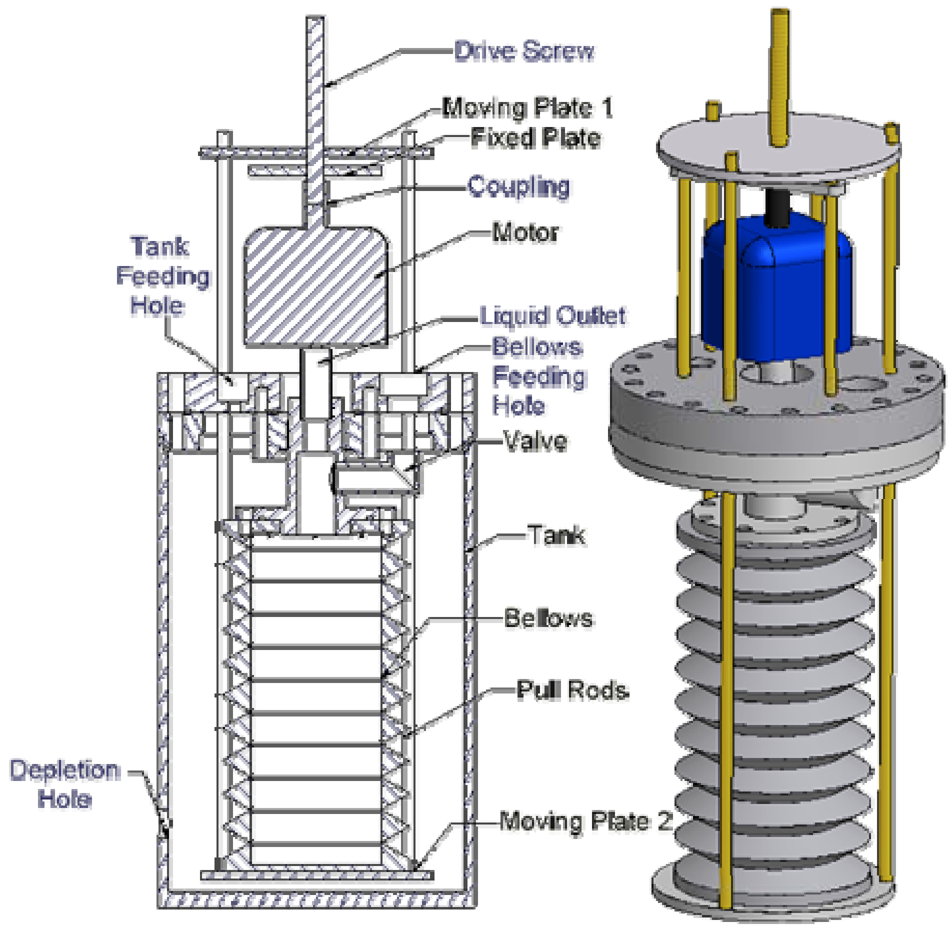

Figure 3-3. Cryogenic flow driven system.

A commercial constant speed motor is mounted on the tank cap by three brass rods. The shaft of the motor is coupled with a drive screw, which pulls the bottom moving plate by three pull rods and therefore compresses the bellows with constant speed when the motor is turned on. Totally three motors with different speed are used in the experiments. The bellows compression speed is determined by the motor speed and the pitch of the drive screw. Foam insulation is applied around the outside of the whole tank to reduce the heat loss.

Before using the bellows driven system, an insulated reservoir was also used for ground tests, and the flow is driven by the hydraulic head of the reservoir. With this configuration the system is easy to control, and the experimental time can be extended much longer, however, the major drawback is the larger uncertainty of the flow rate compared with bellows driven system.

3.1.3 Test Section

The test section is a Pyrex glass tube of 25.4 cm long. The ID and OD of the test section are 11.1 mm and 15.8 mm, respectively. The test section inlet and outlet are stainless steel tubes. At both ends of the test section, stainless steel adaptors and Teflon ferrules are used to connect the test section to the test section inlet and outlet portion.

There are 9 drilled holes of approximately 2mm depth in the test section. The diameter of each hole is 1mm. A total of 15 type-T thermocouples are placed on the test section, 9 are embedded very close to the inner surface through drilled holes at three downstream cross-sections. At each cross-section, three thermocouples are located circumferentially at equal separation distance. The other 6 thermocouples are used to measure the outside wall temperatures at two cross-sections, also located circumferentially at equal separation distance. The test section can be rotated along its axis before being fastened at two ends. Figure 3-4 sketches the test section and the thermocouple locations in one of the tests.

The test section inlet, test section and test section outlet are enclosed in a vacuum jacket built from stainless steel vacuum components. Two transparent quartz windows in the vacuum jacket enable the observation and record of the two-phase flow regimes inside the test section. The diameter of each window is 7.62 cm. A ceramic sealed vacuum feed-through flange is used to connect the thermocouple wires from the vacuum side to the air side. The vacuum is maintained by a potable vacuum pump during the experiments.

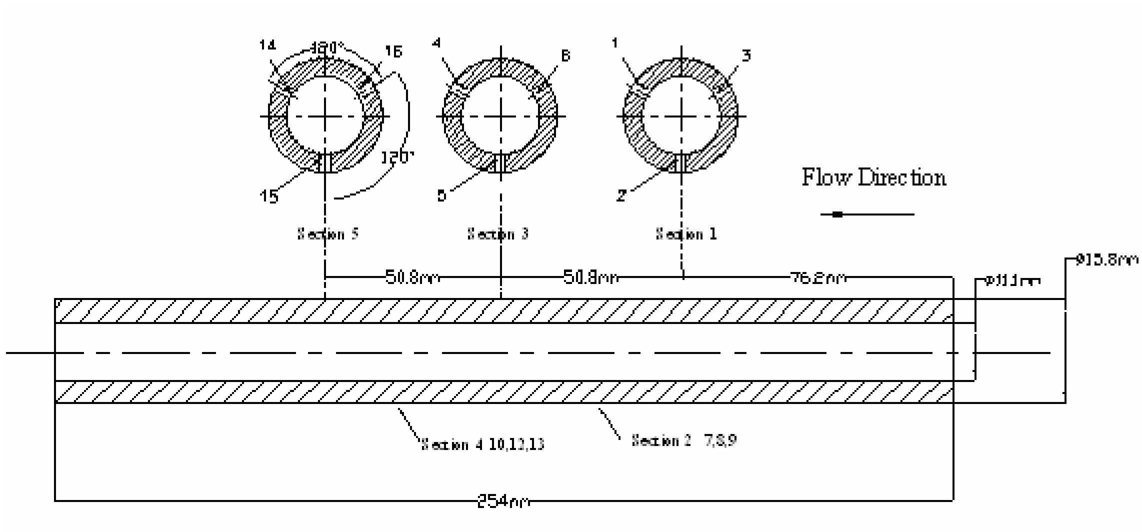

Figure 3-4. Test section and thermocouple locations.

A CCD camera (CV-730 from Motion Analysis Inc.) set with 1/1,000 sec shutter speed faces one of the quartz windows to record flow images, while lighting is provided by a fluorescent light at the other widow.

3.1.4 Experimental Rig

A rig consists of an aluminum frame that houses the experimental apparatus. The main function of the rig is to secure all the equipment during the microgravity tests. The important qualities of a rig are:

- Strong enough to withstand the deceleration (with all equipment attached).
- Have sufficient room to house the necessary equipment.
- Minimize weight as much as possible.

Two rigs of 16 inch wide, 32 inch long and 20 inch high are connected and used in the experiments. Bottom of the two rigs is covered by two thin aluminum plates. For ground experiments, the flow driven system and the vacuum jacket are fastened to the bottom aluminum plates. For microgravity experiments, all the equipment include the light, the CCD camera and the vacuum pump are fastened to the bottom plates and no part of the equipment can stretch out the rigs. A mirror is used in this situation for adjusting light path so that the camera can be set inside the rig. To ensure smooth drop process the equipment need also to be evenly distributed.

3.2 Data Acquisition System

A data acquisition system is built for recording temperatures and flow images during experiments. Type T thermocouples (Omega) with Teflon insulation are used for temperature measurement. The gauge size of the thermocouple wires is 30 AWG. The thermocouples are wired to a screw terminal board and then connected to a 16-channel thermocouple board (PCI-DAS-TC from Measurement Computing) plugged into the PCI slot of a computer. The thermocouple board has built in cold junction compensation and programmable gain ranges. All the thermocouples are tested and calibrated with boiling nitrogen prior to the chilldown experiments. A Labview program is developed to read the temperature measurements to the computer. The program has a friendly graphical user interface and updates the temperature profiles simultaneously during the tests.

Video images are monitored and recorded by connecting the CCD camera to a frame grabber board (FlashBus MV Lite from Integral) plugged into the PCI slot of the computer. A commercial software records the flow images and also shows the real-time images on the computer screen.

For microgravity tests, thermocouple extension wires about 20 m long are used to connect the thermocouples to the temperature acquisition board, so that temperature data can be collected during the drop with comparable accuracy.

3.3 Drop Tower for Providing Microgravity Condition

3.3.1 Introduction of Microgravity Facilities

There are mainly four facilities that can provide microgravity environment: sounding rocket, spacecraft, aircraft flying parabolic trajectories and drop tower. With continuing increase in microgravity research, many researchers have found, and will continue to find, the high cost and distant locations associated with many of the world's microgravity facilities limit their progress. This is especially true for lower-budget, small-scale research projects. It is also very difficult for many researchers to quickly develop and perform rough microgravity testing on a new concept or idea. However, drop towers can be built on-site, are relatively inexpensive to operate, and provide good to excellent microgravity levels. Compared with other facilities, the available microgravity time from drop tower is relatively short, however, for many research applications especially those in the preliminary testing stages, this is not a limiting factor.

3.3.2 Drop Tower Design and Microgravity Condition

An empty elevator shaft located in the Nuclear Science Building at the University of Florida is used as the foundation for the drop tower. The drop tower is 5-story high and has a maximum drop height of 15.25 m, which approximately equals to free fall time of 1.7 seconds. This drop tower is a reconstruction of the 2.1 seconds drop tower in the Washington State University. Many parts came from that 2.1 seconds drop tower and most of the designs are similar to the 2.1 seconds drop tower also. For more detail of the drop tower design can refer to the Master Thesis of Snyder (1993).

Figure 3-5 gives the sketch and some dimensions of the drop tower. The drop tower mainly consists of a release-retrieve mechanism, a drag shield, an airbag deceleration system, power and experimental control system.

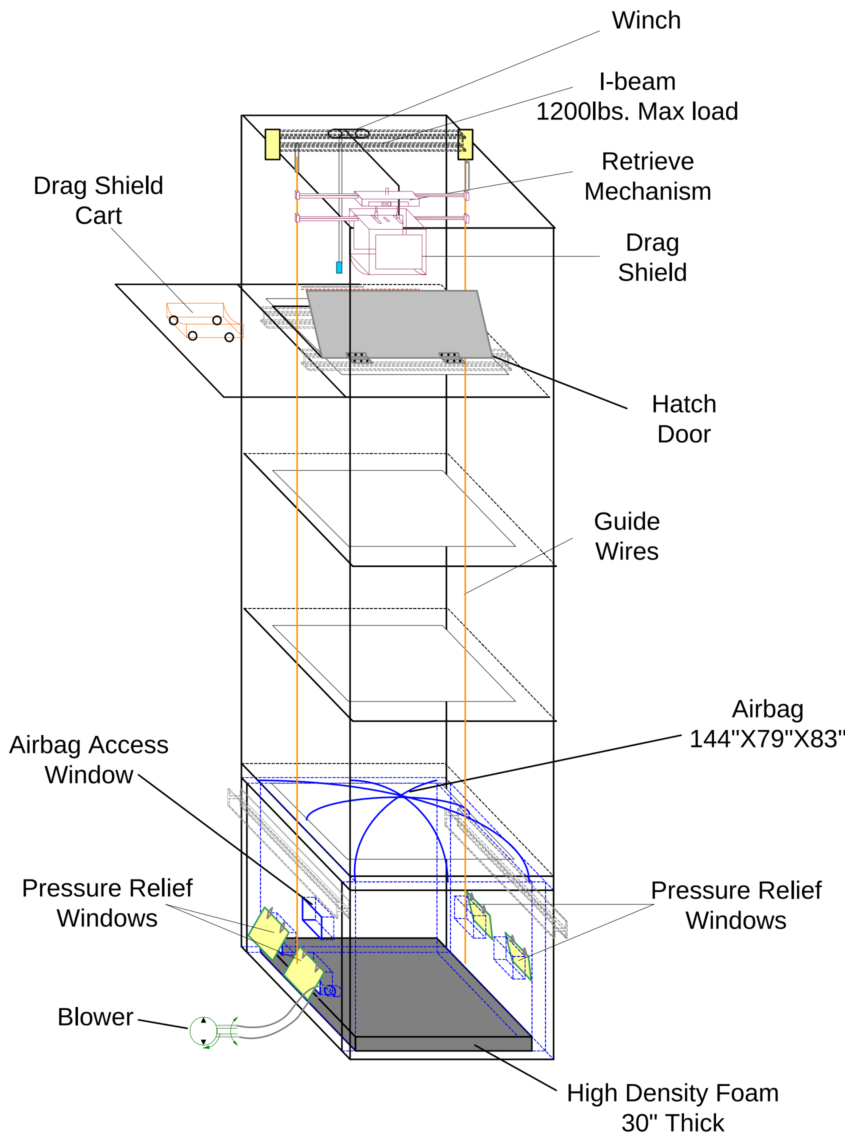

Figure 3-5. Drop tower system.

3.3.2.1 Release-retrieve mechanism

The release-retrieve mechanism is composed of a steel cross member with two arms extending out the sides similar to that of the drag shield (Figure 3-6). Before a drop, the release-retrieve mechanism can lower the experiment and the drag shield down the shaft to any drop height desired. After a drop, the release-retrieve mechanism can remotely retrieve the experimental system and drag shield with its self-locking hitches. A tapered pin release mechanism is designed that uses frictional forces to hold the experimental system and the drag shield before release. The tapered pin is pounded into place similar to that of a drill chuck. A solenoid is used to release the frictional forces by simply allowing the chuck to split open as shown in Figure 3-6. During the release the tapered pin glides along the chuck and provides a symmetrical release which helps avoid any rotation. The connection from the tapered pin to the experimental system is also specially designed to reduce the adverse effects during the release.

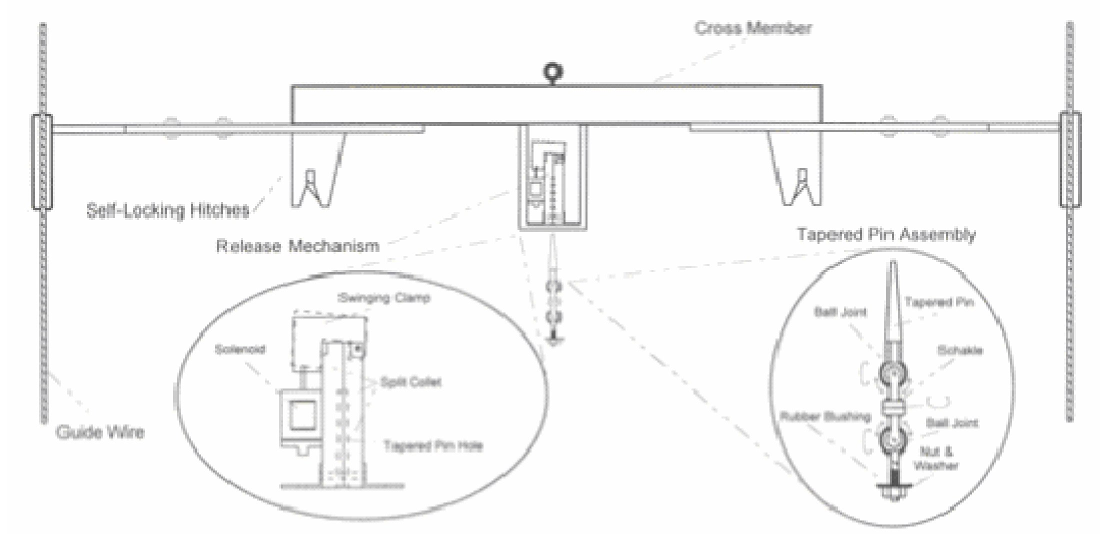

Figure 3-6. Release-retrieve mechanism of the drop tower.

3.3.2.2 Guide wires

Two guide wires stretch the length of the shaft on both sides of the drag shield. The guide wires are used to keep the drag shield vertical during deceleration and also insure that the release-retrieve mechanism and the drag shield are aligned for remote retrieval after a drop.

3.3.2.3 Drag shield

The drag shield is used to isolate the exterior drags that come from the guide wire, the friction of the air and etc. Bottom section of the drag shield is a semi cylinder filled with sand as ballast. The purpose of this design is to ensure the impact can be evenly distributed to the airbag deceleration system during the deceleration period. A cart matches the shape of the bottom section is used to slide the drag shield. Top section of the drag shield is rectangular with two arms extending outside to the guide wires. The bottom section of the drag shield is connected to the top section with the use of 6 enclosed latches, so that the drag shield can be taken apart. When disconnected, the bottom semi cylinder section can stay on the sliding cart and be slid out from under the top section. This allows the experimental apparatus to be placed onto the bottom section and then slid back into place under the drag shield top again, thus, loading the experiment apparatus. A similar process is followed when unloading the experimental apparatus. There are two doors on both side of the drag shield, and can also be used for loading experimental apparatus with light weight.

Figure 3-7 gives the sketch and some dimensions of the drag shield and the experimental system. Before each drop, the drag shield and the experimental system are held to the release-retrieve mechanism by the tapered pin. The tapered pin is released when the drop button is pushed to trigger the solenoid. During the drop, the drag shield moves slower than the inside experimental system, because there are some resistant forces on the drag shield from the guide wires and the exterior air while the only resistant force on the experimental system comes form the inside air, which is also moving with the drag shield. Therefore, high microgravity level can be achieved on the experimental system.

To minimize the deceleration impact, it is desirable that the experimental system hits the drag shield at the same time when the drag shield hits the airbag. However, there is no effective method to evaluate the drags on the drag shield during the drop. So this is just ensured by trial and error to find the best drop distance of the experimental system.

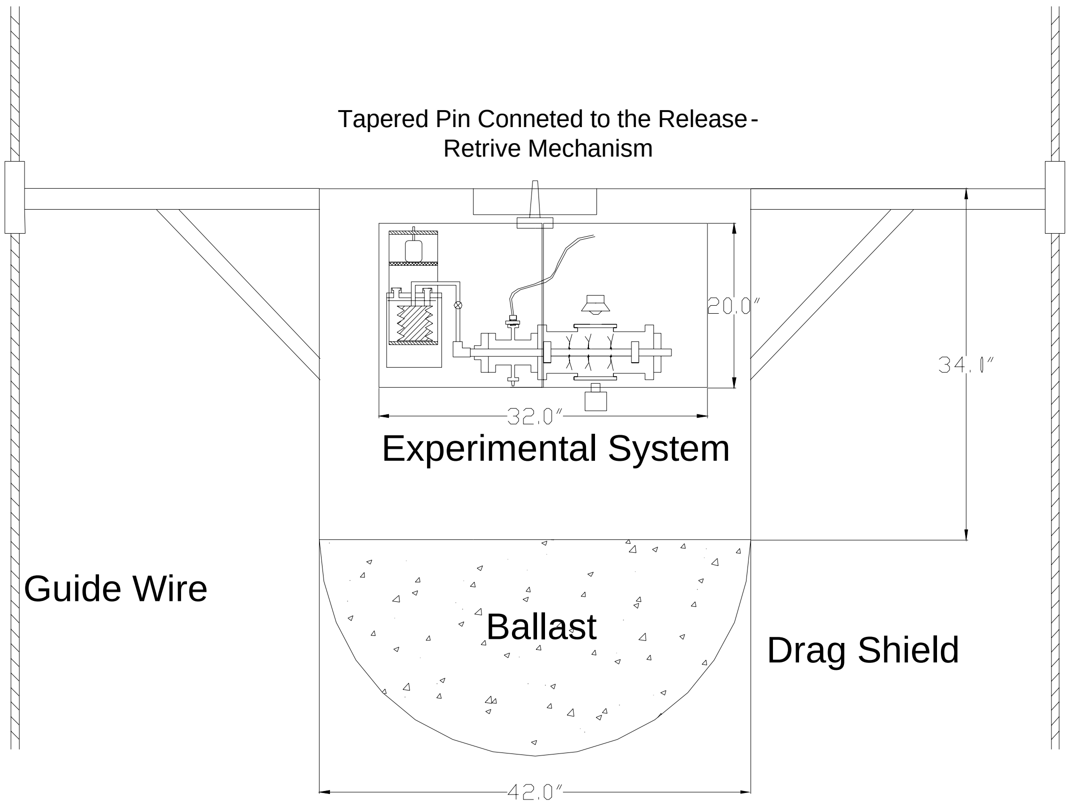

Figure 3-7. Drag shield and the experimental system before a drop.

3.3.2.4 Airbag deceleration system

Airbag deceleration system built at the bottom of the drop tower is used to decelerate the drag shield at the end of the drop with relatively small impact. The system consists of $144 \times 79 \times 83$ inch wooden box which encloses a vinyl coated polyester airbag of approximately the same dimension. High density foam of 30 inch thick is laid down between the ground and the airbag. There are four pressure relief windows on the box with two on each side. The windows open at the deceleration period to insure smooth deceleration process. Windows at opposite sides of the wooden box are connected together with high tension bungee cord. A one horsepower blower is used to fill the airbag. The test results show that the airbag deceleration system works efficient and is simple to use. The same air venting settings can cover a large variety of drop weight and drop height with no more than 20-g deceleration.

3.3.2.5 External connections

Power, video, data acquisition, and experimental control are all connected externally in this design. Thus less equipment has to be on the experimental system, and the data acquisition can be accomplished on a standard PC.

3.3.2.6 Microgravity condition

The drop tower described here is inexpensive to build, easy to operate, has relatively low deceleration, low release vibration and rotation, and has a good microgravity level. This drop tower can provide a maximum microgravity time of 1.7 seconds with the microgravity level between 10^{-5} to 10^{-4} g.

3.3.3 Safety Summary

Safety is the most important issue in the drop tower microgravity tests. A brief summary concerning safety issues is given below.

To release the drag shield, a 5V pulse is needed to be sent to the release mechanism by the computer. A control circuit, which consists of two switches, is added between the computer and the release mechanism. The first switch is controlled by a key that insures no one can operate the drop tower without permission. The second is a spring type switch that is activated only when it is pushed down. Thus if the computer sends a 5V pulse to the release mechanism “on accident” the solenoid will not get power unless this button is also pushed.

Four aluminum bars are installed to the ground floor door to enhance and lock the door while the drop tower is in operation. As mentioned earlier, the two guide wires insure that the drag shield cannot come off course during the drop. Safety railing is installed at three sides of the drag shield. The other side is secured when the hatch door is open. An expanded wire mesh is installed completely around the guide wires in the drop level in case the wires come loose during a drop. Four cameras are installed to monitor the drop process, three on the ground level one on the drop level. The drop process is shown on the computer screen, and a copy is also recorded in the computer, which could be used for reviewing and improving the design of the drop tower.

3.4 Experimental Condition and Procedure

3.4.1 Experimental Condition

In the experiment, liquid nitrogen is chosen as the working fluid because of its non-flammable and non-toxic nature. Liquid nitrogen is also inexpensive to use. Before each test, the tank and the bellows are fed several times until the liquid nitrogen inside the tank and the bellows is in a quasi-steady state. Since the bellows is totally immersed in liquid nitrogen, it is assumed that the exit state from the bellows is saturated liquid nitrogen at 1atm. The pipes before the test section are also pre-cooled by liquid nitrogen through bypass lines before the test.

Efforts have been tried to control the back pressure at the exit of the flow. A tank installed with a check valve is used for this purpose; however, it is found that this method is not applicable for cryogenic fluids: the liquid boils off very quickly inside the tank and causes the check valve to open and close frequently, and thus introduces large fluctuation to the back pressure. So the flow is vented to the atmosphere directly during the tests.

Three constant speed motors are used to drive the bellows. The speed of the motor is 5 rpm, 10rpm and 15 rpm, respectively. The bellows compression speed is determined by the driven motor rotation speed and the pitch of the drive screw:

$$V_{bel} = V_{rot} L_{pit} \tag{3.1}$$

in which V_{bel} is the bellows compression speed, V_{rot} is the motor rotation speed, L_{pit} is the pitch of the drive screw, and the mass flux inside the test section can be expressed as:

$$G = \rho_l \left(\frac{D_{bel}}{D} \right)^2 V_{rot} L_{pit} \tag{3.2}$$

where G is the mass flux, ρ_l is the saturation liquid density of the nitrogen, D is the ID of the test section and D_{bel} is ID of the bellows.

Table 3-1 shows the working condition of the experiments. The vacuum level during the test is maintained at about 0.9 by a portable vacuum pump.

Table 3-1. Working condition of the experiments.

Motor speed (rpm)	Liquid velocity entering the test section (cm/s)	Mass flux $\left(\mathrm{kg/m^2s}\right)$	Approximated test duration limit (minute)
5	0.446	3.606	15
10	0.891	7.205	7.5
15	1.337	10.811	5

3.4.2 Ground Test Procedure

The ground test procedure is as follows:

1. Install the top moving plane at the bottom position of the drive screw.
2. Turn on the light and the camera.
3. Turn on the vacuum pump; make sure the vacuum level is normal.
4. Close the control valve to the test section, open the feeding valve to the bellows and the tank, and open the valve on the bellows.
5. Feed liquid nitrogen to both the bellows and the tank. This step is repeated several times until the tank is cooled down.
6. Close the feeding valve and the valve on the bellows.
7. Begin to collect data, run the data acquisition and video record programs.
8. Open the control valve to the test section.

9. Turn on the motor to compress the bellows and liquid nitrogen is introduced to the test section.

10. Finish one test, turn off everything and loose the bellows.

3.4.3 Microgravity Test Procedure

The microgravity test procedure includes the operation of the drop tower, and is much more complicated compared with the ground test. The procedure is summarized as follows:

1. Open the blower to inflate the airbag; check and make sure the air bag and the windows at the 1st floor work properly. This step is very important for the safe operation of the drop tower. The airbag must strong enough to provide proper deceleration for the drag shield and the experimental setup, yet it can not be too stiff to bounce the drag shield back and cause damage. The stiffness of the airbag is determined by the tension of the bungee cords connected the relief windows. The tension of the bungee cords is checked before each drop.

2. Insert and knock in the tapered pin connector to the release-retrieve mechanism.

3. Open the doors on the drag shield and load the experimental apparatus to the drag shield.

4. Raise the experimental apparatus until it reach the top of the drag shield.

5. Connect the experimental apparatus to the threaded head of the tapered pin.

6. Lift the drag shield up a little so that the sliding card under the drag shield can be moved out of the space.

7. Lift the drag shield just high enough to open the hatch door on the 5th floor, and then lower it down for feeding the liquid nitrogen.

8. Follow the ground test procedure from step 1 to step 10. The only difference is that the feeding pipes are removed after finish. So there is no equipment stretches out the rigs.

9. Replace the doors on the drag shield; open the two self-locking hitches on the release-retrieve mechanism. Now the drag shield and the experimental apparatus are hung by the tapered pin.

10. Raise the drag shield to the drop position and wait the drag shield to stabilize, recheck every thing on the 5th floor (external wiring video equipment, data acquisition program, etc.).

11. Turn the first switch, the key switch, on the control. Now the release mechanism will work and release the drag shield whenever the second switch, the drop button, is pressed.

12. Turn on the bellows driven motor to generate the nitrogen flow. The driven motor uses a power cable connects externally to the drag shield. A power outlet with on/off switch connects the power cable to the wall. So the driven motor can be controlled at the drop level.

13. Wait for the desired working condition. The temperatures and the flow images are shown simultaneously on the monitor, so the release can be made at desired working condition.

14. Push the drop button and release the drag shield.

15. Turn off the driven motor to stop the nitrogen flow.

16. Close the two self-locking hitches on the release-retrieve mechanism; retrieve the drag shield and the experimental apparatus at the ground floor.

17. Stop the data acquisition program.

18. Check the drag shield and the experimental apparatus when they are retrieved back to the drop level, and loose the bellows.

19. Check the airbag deceleration system at the ground level and finish one test.

3.5 Uncertainty Analysis

For single sampled experiments, the method introduced by Kline and McClintock (1953) has been widely used to determine the uncertainty. In current experiments, one needs to solve the inverse heat conduction problem (IHCP) to get the surface heat flux from temperature measurements (Ozisik 1993; Ozisik and Orlande, 2000), and simple equation that relates the measured data to the heat flux does not exist. Therefore, only the uncertainty of the measurement itself and the uncertainty from the experimental apparatus will be given here.

3.5.1 Uncertainties of Temperature Measurement

The type T thermocouples used for temperature measurement have the uncertainty of $\pm 0.5^0 C$ declared by the manufacturer. For highly transient process like chilldown the response time of the thermocouples is also important. To get quick response, the tip style of the thermocouples is chosen as exposed and the wire diameter of the thermocouples is used as smaller as possible. With the wire diameter of 0.25 mm the responding time is less than 0.2 second according to the chart given by the manufacturer.

Another uncertainty source of temperature measurement comes from the data acquisition (DAQ) system. The DAQ board for temperature measurement has programmable gain ranges and A/D pacing, and accepts all the thermocouple types. The accuracy of the measurement depends on the gain, the sample rate and the thermocouple type. The uncertainty of type T thermocouple is $\pm 0.9^0 C$ for worst case from the product specification. For current experiment, the gain is set at 400 and the sample rate is about 60 Hz. It is found that the uncertainty for current settings is about $\pm 0.3^0 C$.

3.5.2 Uncertainty of Mass Flux

The uncertainty of mass flux δ_G is evaluated as (Kline and McClintock, 1953):

$$\delta_G = \left[\left(\frac{\partial G}{\partial \rho} \delta_\rho \right)^2 + \left(\frac{\partial G}{\partial D} \delta_{d_{bel}} \right)^2 + \left(\frac{\partial G}{\partial D_{\sec}} \delta_{d_{\sec}} \right)^2 + \left(\frac{\partial G}{\partial V_{rot}} \delta_{V_{rot}} \right)^2 + \left(\frac{\partial G}{\partial L_{pit}} \delta_{L_{pit}} \right)^2 \right]^{\frac{1}{2}} \quad (3.3)$$

where δ is the absolute error. The relative error for mass flux measurement is then:

$$\frac{\delta_G}{G} = \left[\left(\frac{\delta_\rho}{\rho} \right)^2 + 2^2 \left(\frac{\delta_{d_{bel}}}{D_{bel}} \right)^2 + 2^2 \left(\frac{\delta_{d_{\sec}}}{D} \right)^2 + \left(\frac{\delta_{V_{rot}}}{V_{rot}} \right)^2 + \left(\frac{\delta_{L_{pit}}}{L_{pit}} \right)^2 \right]^{\frac{1}{2}} \quad (3.4)$$

The diameter of the test section has an ID of 11.1 ± 0.2 mm given by the manufacturer. The absolute error of the bellows ID is within ± 0.2 mm. The error of the motor rotation speed is not given by the manufacturer. Simple tests have been conducted to calibrate the motor rotation speed. For each motor used, let the motor run for a relatively long time and record the time and the total revolution times, then calculate the motor speed. It is found that the relative error of the motor rotation speed is with in 5%. The error of the drive screw pitch can be estimated by measuring the length of several screw threads and then divide the number of threads. The relative error of the drive screw pitch is found to be approximately 3%. The error of quoted density data can be formed by comparing values from different sources. In Appendix II of the book written by Carey (1992) gives the saturation liquid density of the nitrogen as $807.10 \mathrm{kg/m^3}$, while another book (Flynn 1996) gives the value of $808.9 \mathrm{kg/m^3}$. So the relative error of the saturation liquid nitrogen density is evaluated as 0.22%. From Equation 3.4, the relative error for mass flux measurement is 6.88%.

Because the diameter of the test section is relatively small and in Equation 3.3 the diameter term is squared, the error of the test section ID contributes most to the total error. The uncertainty of the mass flux can be greatly reduced by using tubes with higher accuracy.

3.5.3 Other Uncertainties

The vacuum level is measured by a vacuum gauge that has the minimum scale of 0.02 bar, so the uncertainty of the vacuum level is approximately 0.01 bar.

Thermocouple feed-through is used to connect the thermocouple wires from the vacuum side to the air side. For this situation, a third metal other than the two metals (copper and constantan) used in the thermocouples is introduced in, this will cause error in temperature measurement unless the third metal in both wires are identical, have the same length, and are kept at same temperature. These requirements are satisfied in the experiment, so the error introduced by the thermocouple feed-through is comparably negligible. However, attention must be paid to avoid large temperature gradient along the feed-through flange during the tests.

CHAPTER 4
CRYOGENIC TWO-PHASE CHILLDOWN UNDER TERRESTRIAL CONDITION

Cryogenic two-phase chilldown under terrestrial condition are experimentally studied in this chapter. Three different experimental methods have been performed. Gravity-driven experiments enhance the basic understanding of the chilldown process, while bellows-driven experiments have more accurate flow control. In rewetting tests, the test section is pre-cooled so that transition flow boiling and nuclear flow boiling stages can also be covered. Based on the experimental results, a phenomenological model is developed. Good agreement is achieved between the model predictions and the experimental results.

4.1 Gravity-Driven Experiment

In gravity-driven experiments, an insulated reservoir is used to generate the flow with estimated mass flux of 18-23 $\mathrm{kg/m^2s}$ by reviewing the recorded flow images. The results show that the cryogenic chilldown process can be divided into three stages associated with different heat transfer mechanisms.

4.1.1 Heat Transfer Study

For horizontal tube orientation, the two-phase flow is generally stratified because of the gravitational force. Therefore bottom of the tube is chilled down first. The heat transfer mechanism at the bottom of the tube includes film boiling, transition boiling, and nucleate boiling, while the heat transfer mechanism at the top of the tube is mainly convection to superheated vapor.

4.1.1.1 Wall temperature profiles

Wall temperatures are measured by 16 thermocouples, 9 are embedded very close to the inner surface of the tube wall; the other 7 thermocouples measure the outside wall temperature of the test section. The thermocouple locations are shown in Figure 4-1 and different from that described in Chapter 3. The unit for dimension is mm.

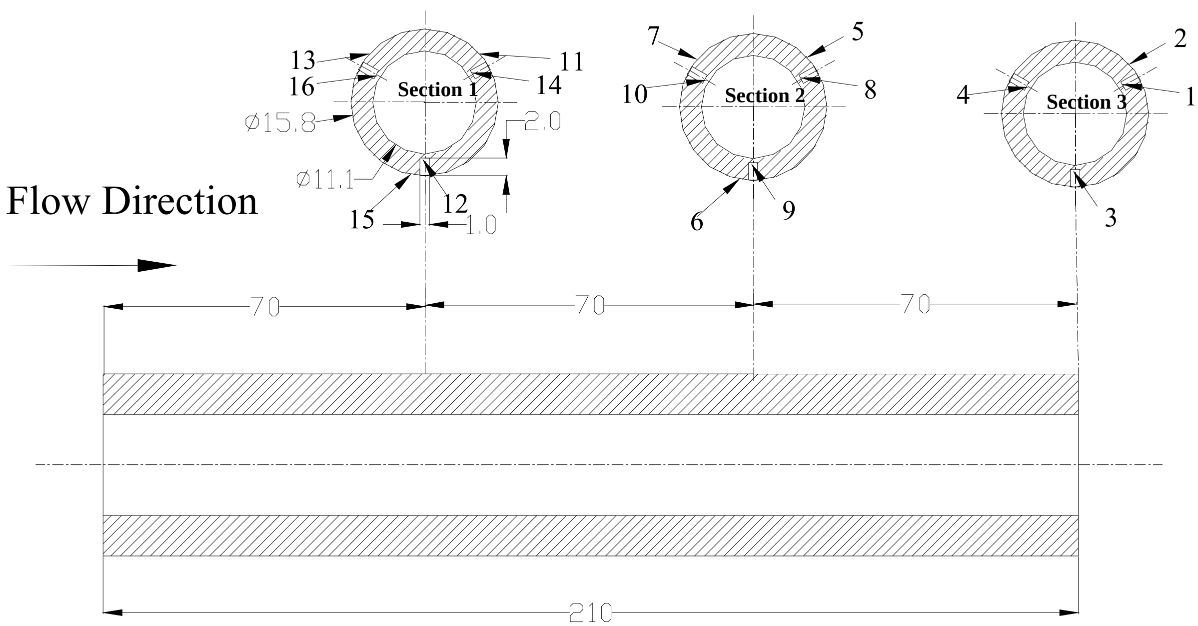

Figure 4-1. Sketch of the test section and thermocouple locations for gravity-driven test.

Figure 4-2 gives the temperature profiles at the inlet and middle section. It is found that large temperature difference exists between the top and bottom of the test section, which was also reported by Bronson (1962) in the experiments of chilldown heavy-wall transfer line. This temperature difference suggests different heat transfer mechanisms are encountered at the top and the bottom of the test section. Since the two phases are separated by gravitational force, the heat transfer mechanism at the bottom is boiling heat transfer, while the heat transfer at the top is forced convection to the vapor phase.

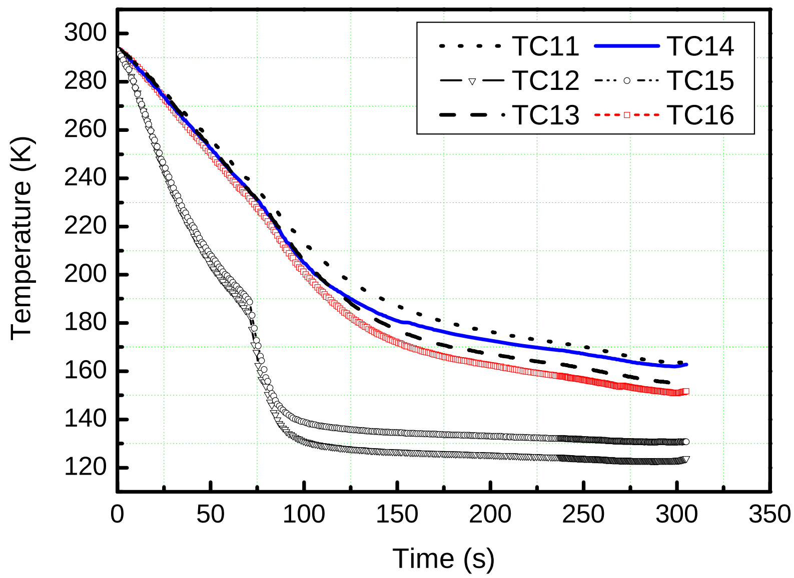

A

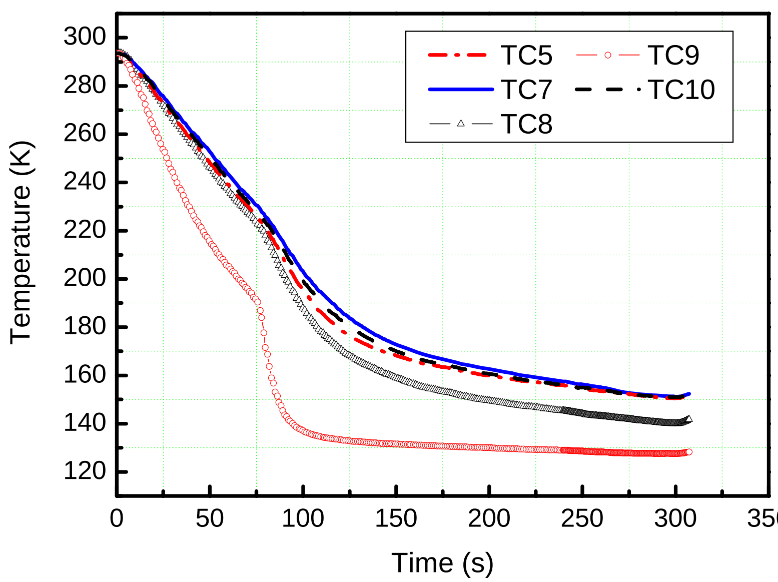

B

Figure 4-2. Temperature profiles of gravity-driven test at different cross-sections. A) Inlet section. B) Middle section.

4.1.1.2 Data reduction

In boiling heat transfer experiments, surface heat flux as a function of wall super heat is often of particular interest, because it denotes different heat transfer mechanisms and is crucial for engineering applications. However, in chilldown or quenching experiments surface heat flux is not controllable. The surface heat flux can be inferred from the temperature history by solving the IHCP. For quenching of vertical tube, in which axial-symmetrical assumption is generally held, the situation is much simpler. Based on exact solution of the IHCP, Burggraf (1964) developed a method to obtain the temperatures and heat fluxes at the inside tube wall from the temperature history data of the thermocouple welded on the outside of the test section:

$$
\begin{aligned}
T_i = T &+ \left(\frac{r_o^2}{4\alpha} \left(\left(\frac{r_i}{r_o} \right)^2 - 1 - 2\ln\frac{r_i}{r_o} \right) \right) \frac{dT}{dt} \\
&+ \left(\frac{1}{64\alpha^2} \left(r_i^4 - 5r_o^4 \right) - \frac{r_o^2 r_i^2}{8\alpha^2} \ln\frac{r_i}{r_o} - \frac{r_o^4}{16\alpha^2} \ln\frac{r_i}{r_o} + \frac{r_o^2 r_i^2}{16\alpha^2} \right) \frac{d^2T}{dt^2} + \ldots
\end{aligned}
\tag{4.1}
$$

where r_i and r_o denote the inner and outer radius, respectively; T_i and T are the inside wall temperature and temperature measured by thermocouple, respectively; α is the thermal diffusivity of the wall. Then the inside wall heat flux with the first three leading terms can be written as (Iloeje et al. 1975):

$$
\begin{aligned}
q''_w = \rho c \left(\frac{r_i^2 - r_o^2}{2r_i} \right) \frac{dT}{dt} &+ \left(\frac{(\rho c)^2}{k} \left(\frac{r_i^3}{16} - \frac{r_o^4}{16r_i} - \frac{r_o^2 r_i}{4} \ln\frac{r_i}{r_o} \right) \right) \frac{d^2T}{dt^2} \\
&+ \frac{(\rho c)^3}{k^2} \left(\frac{r_i^5}{384} - \frac{3r_o^4 r_i}{128} + \frac{3r_o^2 r_i^3}{128} - \frac{r_o^6}{384r_i} - \frac{r_o^2 r_i^3}{32} \ln\frac{r_i}{r_o} - \frac{r_o^4 r_i}{32} \ln\frac{r_i}{r_o} \right) \frac{d^3T}{dt^3}
\end{aligned}
\tag{4.2}
$$

For horizontal chilldown experiments, the axial-symmetrical assumption is not valid, and the solution of the IHCP surfers from ill-posedness. In order to calculate heat transfer data from the transient temperature profiles, an energy balance is performed locally on a control volume of the tube wall at thermocouple location. The change in stored heat in the control volume is equated to the heat transported to the fluid and heat transferred by conduction, minus losses to the environment. This method was used by many researchers in analyzing data from quenching tests (Abdul-Razzak et. al 1992;

Westbye and Kawaji 1995; Chen et al. 1979). The inside wall heat flux is then given as:

$$q''_w = -\rho c\left(\frac{r_o^2 - r_i^2}{2r_i}\right)\frac{dT}{dt} + \frac{k}{U^2}\left(\frac{r_o^2 - r_i^2}{2r_i}\right)\frac{d^2T}{dt^2} - \left(\frac{r_o}{r_i}\right)\left(q''_{conv} + q''_{rad}\right) + \frac{\left(r_o - r_i\right)}{r_o d\varphi} q''_{cond} \quad (4.3)$$

The first term in the right-hand-side (RHS) of Equation 4.3 comes from the change of the stored heat in the control volume and is the dominant term in chilldown experiments. It is also interesting to note that this term equals the first term from the IHCP solution given in Equation 4.2.

To estimate the axial heat conduction term in rewetting experiments, Chen et al. (1979) assumed a constant rewetting velocity U, and the axial temperature gradient $\left(dT/dz\right)$ was represented by $\left(1/U\right)\left(dT/dz\right)$. Then the effect of the axial conduction on the inside wall heat flux can be evaluated from the second term in the RHS of Equation 4.3. The axial conduction term is generally very small, and it is only important at location near the quenching front, where maximum axial temperature gradient exists between the dry side and the wet side of the wall. A comparison between heat fluxes based on a 2-D heat transfer model (Cheng 1978), which considers the axial heat conduction, with those obtained by neglecting axial conduction was given by Cheng et al. (1979). The comparison for the copper test section showed that the two mid-plane boiling curves were approximately the same and the net axial conduction at the mid-section is negligible small. In our experiments, the temperature measurements show that the axial temperature gradient is relatively small, and additionally the heat conductivity of the glass is much smaller than that of the copper used by Cheng et al.(1979), therefore the axial heat conduction along the test section is neglected in heat flux calculation. It is left in Equation 4.3 only for integrity.

The third term in Equation 4.3 accounts for the contribution from the radiation and natural convection inside the vacuum jacket. The details of how they are evaluated will be given later.

The last term in Equation 4.3 comes from the circumferential heat transfer. Here, $d\varphi$ is the azimuthal angle of the control volume and depends on the size of the control volume. In our calculation, the control volume is approximately assumed to be in thermal equilibrium with the embedded thermocouple. Based on this assumption, the control volume size is chosen with an average arc length of 2.0mm. The circumferential temperature gradient is calculated by linear interpolation between the thermocouple measuring points.

Derivative of the temperature history is needed in calculating the first term in Equation 4.3. Generally, the finite difference method is not suitable to obtain the temperature derivatives, because it is very susceptive to small fluctuations, which are inevitable in measurements. Therefore, a least square technique, proposed by Iloeje et al. (1975) in similar situation, is used to get smooth profiles. To increase accuracy, the temperature data are divided into segments and the order of the curve fit used for each segment is made as high as possible (but less than 6, otherwise will subject to temperature fluctuations) without reintroducing irregularities inherent in the pure data. Figure 4-3 shows a typical result obtained with the least square fit procedure, and Figure 4-4 compares the first term in Equation 4.3 calculated from the least square fit line with that from the finite difference method. It is clear that the finite difference method is not suitable for calculating the derivatives of measured temperature profiles.

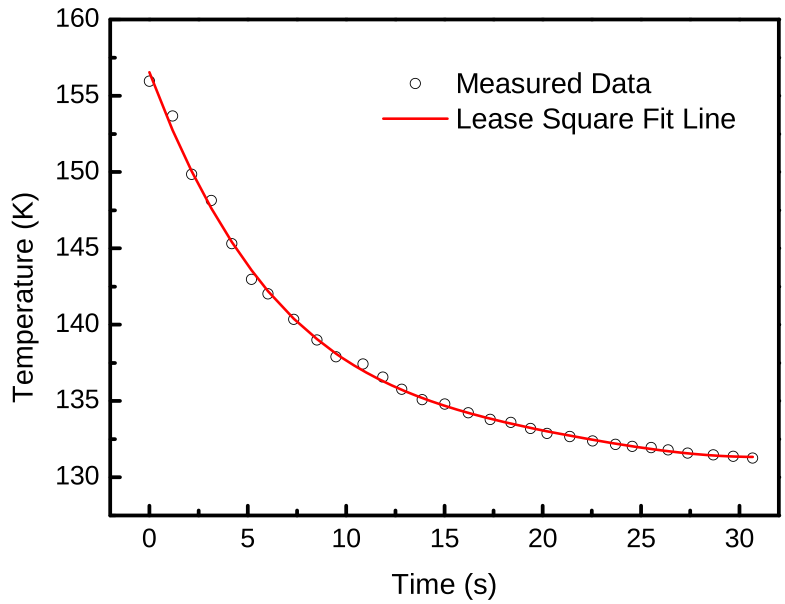

Figure 4-3. Typical curve fit line of the experimental data.

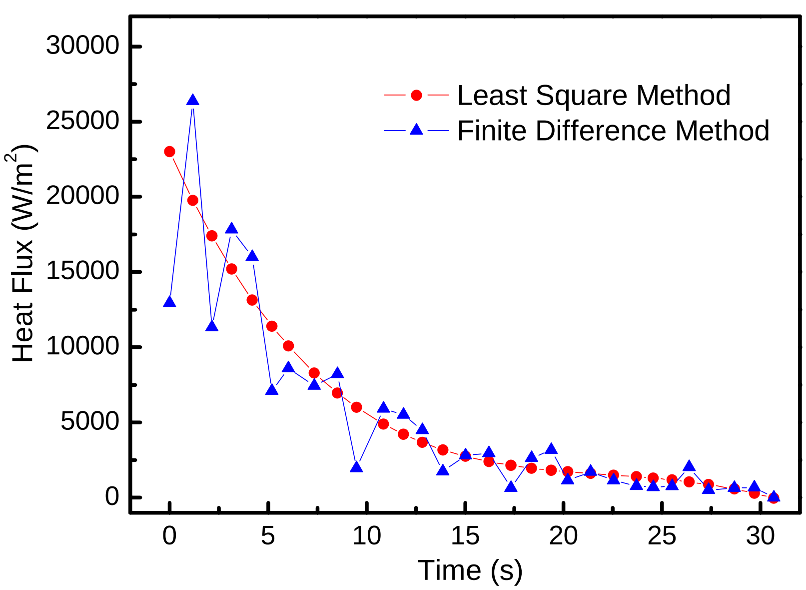

Figure 4-4. Temperature derivatives calculated by least square fit method and by finite difference method.

Assume the vacuum jacket and the test section as long concentric cylinders, the radiation contribution to the heat flux, q''_{rad} , is obtained by (Incropera and Dewitt 2002; Liao 2005):

$$q''_{rad} = \frac{\sigma_B \left(T_j^4 - T_o^4\right)}{\frac{1}{\varepsilon_t} + \frac{1-\varepsilon_j}{\varepsilon_j}\left(\frac{r_o}{r_j}\right)} \tag{4.4}$$

where σ_B is Stefen Boltzmann constant, T_j is the temperature of the vacuum jacket, and is assumed to equal room temperature, T_o is the outer wall temperature of the test section, ε_j and ε_t are emissivity of the vacuum jacket and the test section, respectively, and r_o and r_j are outer radius of the test section and the inner radius of the vacuum jacket, respectively.

To evaluate the natural convection heat transfer due to the residual air inside the vacuum jacket, Raithby and Hollands' correlation (Raithby and Hollands 1975; Liao 2005) is used:

$$q''_{conv} = \frac{k_{eff}}{r_o \ln\left(r_j / r_o\right)}\left(T_j - T_o\right) \tag{4.5}$$

where k_{eff} is the effective thermal conductivity given by Raithby and Hollands (1975).

4.1.1.3 Heat transfer mechanisms

The data reduction method given above is used to analyze the transient temperature measurements. Left part of Figure 4-5 shows the calculated bottom wall heat flux as a function of bottom wall temperature at the outlet cross-section, while the right part represents the corresponding temperature profiles.

The shape of bottom heat flux is similar to the boiling curve from steady-state pool boiling experiments. This suggests that the chilldown process may share many common features with pool boiling experiments. Following the method to characterize different heat transfer mechanisms in pool boiling experiments, a maximum or critical heat flux

(CHF) q''_{CHF} and a minimum heat flux $q''_{\min}$ are used to divide the chilldown heat transfer into three stages, which are film boiling, transition boiling and nucleate boiling, as shown in Figure 4-5.

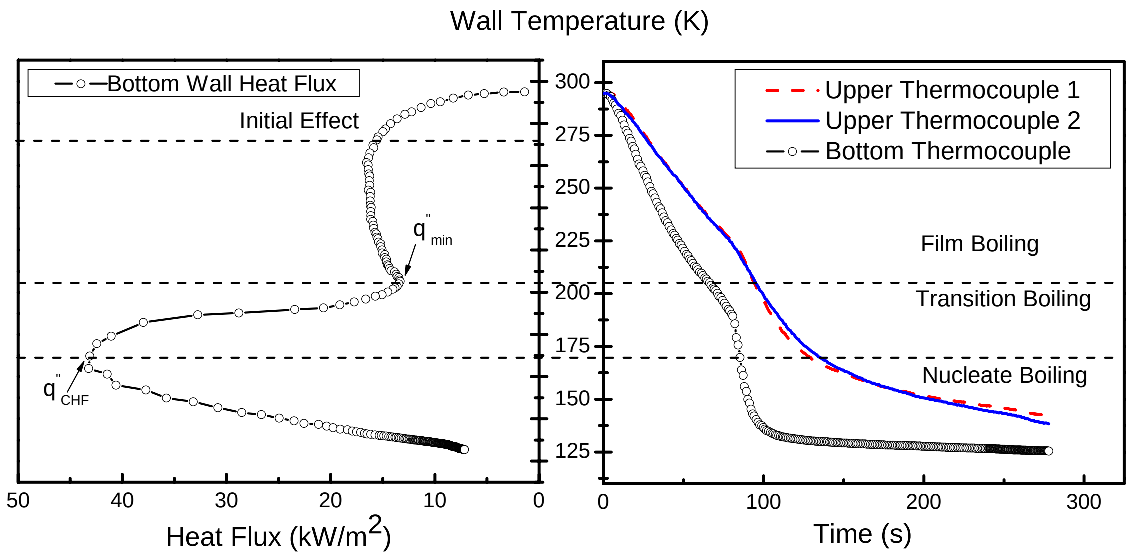

Figure 4-5. Bottom wall heat flux and transient wall temperature profiles at the outlet cross-section.

Initially, the wall temperature is very high, liquid nitrogen evaporates drastically when enters the test section; a vapor film will form and separate the liquid from contacting the wall, the two-phase flow is therefore in film boiling state. At decreased wall temperature, the liquid begins to contact the wall; the heat transfer mechanism is transition boiling, which is characterized by increasing wall heat flux with decreasing wall superheat that contrary to what in the film boiling region and nucleate boiling region. After passing the CHF point the heat transfer mechanism then changes to nucleate boiling.

The calculated bottom wall heat flux as a function of time is shown in Figure 4-6. It is obvious that the time of transition boiling is very short compared with the other two boiling stages.

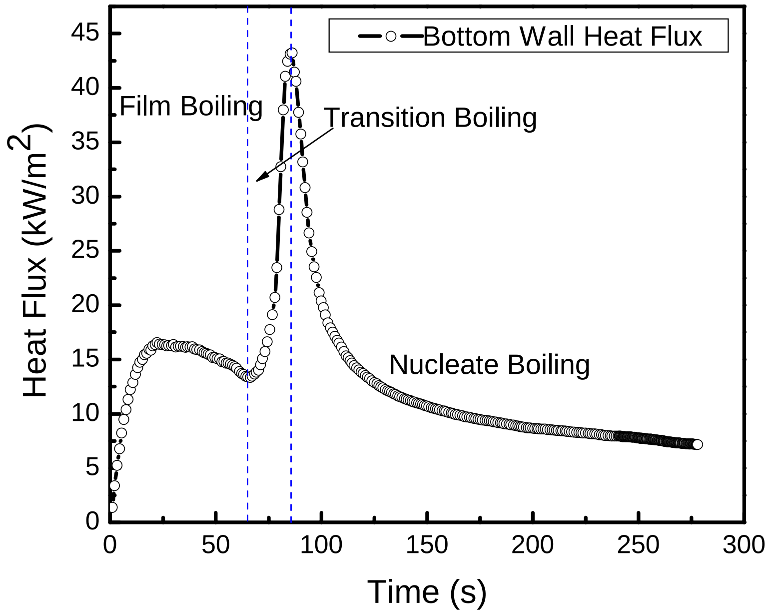

Figure 4-6. Bottom wall heat flux at the outlet cross section as a function of time.

Similarity between the chilldown boiling curve and the pool boiling curve naturally leads one to compare the chilldown data with pool boiling correlations. The comparisons between the two turning points, namely the minimum heat flux and the CHF, are given below.

For steady state film boiling, the correlation developed by Zuber (1959) is widely used to predict the minimum heat flux:

$$q''_{\min} = C h_{lv} \rho_v \left[\frac{\sigma g \left(\rho_l - \rho_v\right)}{\left(\rho_l - \rho_v\right)^2} \right]^{1/4} \tag{4.6}$$

here, σ is surface tension; g is gravitational acceleration; h_{lv} is the latent heat of vaporization, while C was variously given as 0.177 (Zuber 1959), 0.13 (Zuber 1958), or 0.09 (Berenson 1961). The resulting $q''_{\min}$ is then $13.0\,\mathrm{kW/m^2}$, $9.6\,\mathrm{kW/m^2}$, and $6.6\,\mathrm{kW/m^2}$, respectively. In Figure 4-5, the $q''_{\min}$ for chilldown is calculated as $13.3\,\mathrm{kW/m^2}$, which is a slightly larger than steady state prediction with $C = 0.177$.

Based on the similarity between the CHF condition and column flooding, Kutateladze (1948) derived the following relation for the pool boiling CHF:

$$q''_{CHF} = 0.131 h_{lv} \rho_v \left[\frac{\sigma g \left(\rho_l - \rho_v \right)}{\rho_v^2} \right]^{1/4} \tag{4.7}$$

Zuber (1959) got the identical correlation based on the analysis of Taylor and Helmholtz instability. For liquid nitrogen under atmospheric pressure, Equation 4.7 gives a CHF value of $160.7\,\mathrm{kW/m^2}$. The chilldown measurement in Figure 4-6 is only about 27% of this value. This big discrepancy is believed to come from the different experimental condition between the chilldown and the pool boiling tests. In pool boiling experiments, the heat supplied to the fluid is maintained by a heater, while in chilldown tests it comes from the stored heat in the tube wall. In the film boiling region, the heat flux is generally small, therefore the tube wall can maintain a near constant heat flux condition and function like the heater used in the pool boiling tests. However, in the transition boiling region, the stored energy in the tube wall is depleted so quickly that the experimental condition is very different form that of the pool boiling tests. The limited energy stored in the tube wall put a restriction on the value of CHF, which, therefore, is much less than the pool boiling data. Previous work by Bergles and Thompson (1970) also concluded that quantitively the differences between chilldown and steady-state boiling curves can be very large.

In Equation 4.6 and Equation 4.7 the minimum heat flux and CHF are not correlated with the thermal properties of the wall for pool boiling tests. However, as seen from above, the available heat flux to the flow is closely related to the energy stored in the wall. Therefore, the thermal properties, e.g. thermal conductivity, heat capacity, of the wall are expected to play a role in the chilldown process. For example, for a wall with higher thermal conductivity, the energy transferred to the flow can be more quickly supplied by the surroundings, and therefore will result a higher value of CHF.

Figure 4-7 shows the calculated heat flux in different axial locations. It is found that both the CHF and the minimum heat flux decrease with increasing axial distance from the inlet. This is also associated with an increase in the rewetting temperature.

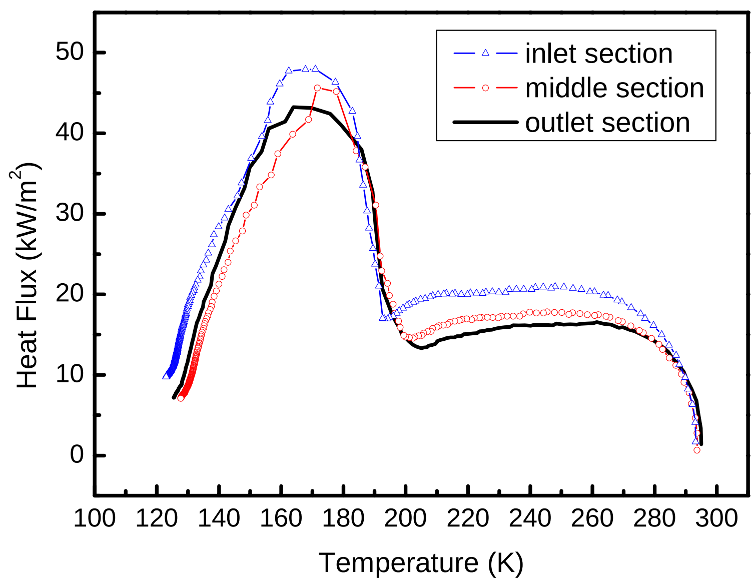

Figure 4-7. Bottom wall heat fluxes at different axial locations.

In most of the previous quenching experiments, the film boiling heat flux was reported as either keeps a relatively constant value (Westbye et al. 1995; Cheng and Ragheb 1979) or decreases as the test section is chilled down (Ganić and Rohsenow 1977; Bergles and Thompson 1970). In our experiments, however, the local heat flux first increases in a short period then decreases gradually. This is consistent with the transient nature of the experiments. Generally the increasing period is expected to be shorter at higher mass flux if the other conditions are kept the same. The mass fluxes in previous investigations were much larger than that in current experiments, and therefore associated with very short increasing time of the heat flux in the film boiling regime. This might be the reason that the increases of the heat flux were not recorded before.

4.1.2 Visualization Study

Heat transfer analysis shows the chilldown process can be divided into three stages with each stage associated with different heat transfer mechanisms. The visualization study casts more light on the characteristic of flow regimes during the chilldown process.

Figure 4-8 illustrates the overall chilldown sequence in our experiments, while some selected flow images in different region of chilldown are shown in Figure 4-9. In the beginning of the film boiling region, the flow pattern is basically dispersed flow, in which the liquid phase is dispersed as near spherical drops within a continuous vapor phase. The void fraction of the two-phase flow decreases as the tube is chilled down, and long liquid filaments, separated from wall by a thin vapor film, are observed to flow along the tube bottom. The length of the liquid filaments generally increases with decreasing wall temperature. For short liquid filaments, the flow regime is close to dispersed flow, while for very long filaments, the flow regime can be classified as highly skewed inverted annular flow. In the film boiling region, heat is primarily transferred from the wall by conduction through the vapor film and thus evaporate the liquid filaments, and by convection to the vapor phase.

Once the bottom wall temperature has been reduced low enough, transient boiling, characterized by intermittent liquid-wall contact and violent bubble generation, is observed. Shortly after the transient boiling, a continuous liquid-wall contact is established and the liquid nitrogen begins to pile up on the bottom wall. Many nucleation sites are observed to be suppressed as the wall temperature keeps decreasing. The prevailing boiling regime is nucleate boiling and the flow pattern is stratified flow or wavy flow.

Previous horizontal quenching tests (Chan and Banerjee1981a; Abdul-Razzak et al. 1992) showed the same sequence as our experiments, however, with different flow regimes mainly in the film boiling region. In their experiments, the flow regime in film boiling was inverted annular flow. The thickness of the liquid core increases with decreasing wall temperature, and then follows the stratified flow regime. While in our experiments, the thickness of the liquid filament is generally a constant, instead the liquid thickness increases in the nucleate boiling region as shown in Figure 4-8.

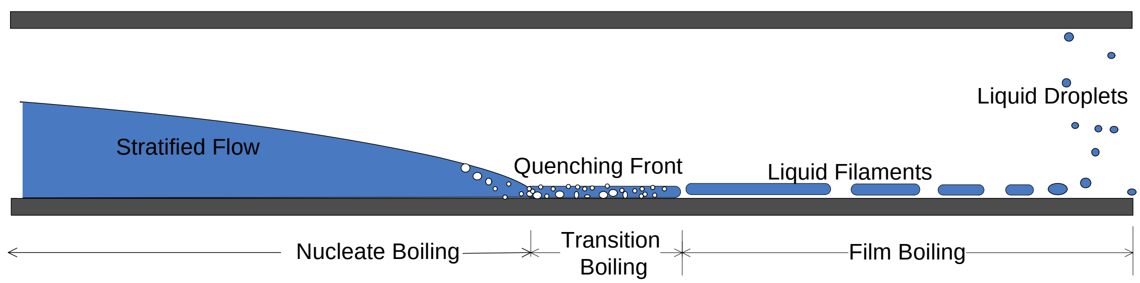

Figure 4-8. Characteristics of horizontal chilldown under low flow rate.

The difference in flow regimes is believed mainly due to different flow rates. The flow rate in the test of Chan and Banerjee (1981a) was about 150~450 $\mathrm{kg/m^2s}$, while it was even higher (400~1300 $\mathrm{kg/m^2s}$) in the experiments by Abdul-Razzak et al. (1992). In current chilldown test, the flow rate is much lower. The heat stored in the tube wall causes dry-out of the liquid phase in the film boiling region and thus leads to the dispersed flow.

The visualization study also gives the detail of propagation the quenching front and how the liquid rewets the tube wall (Figure 4-10). The arrow in Figure 4-10 indicates the limit between the quenching front and the nucleate boiling region.

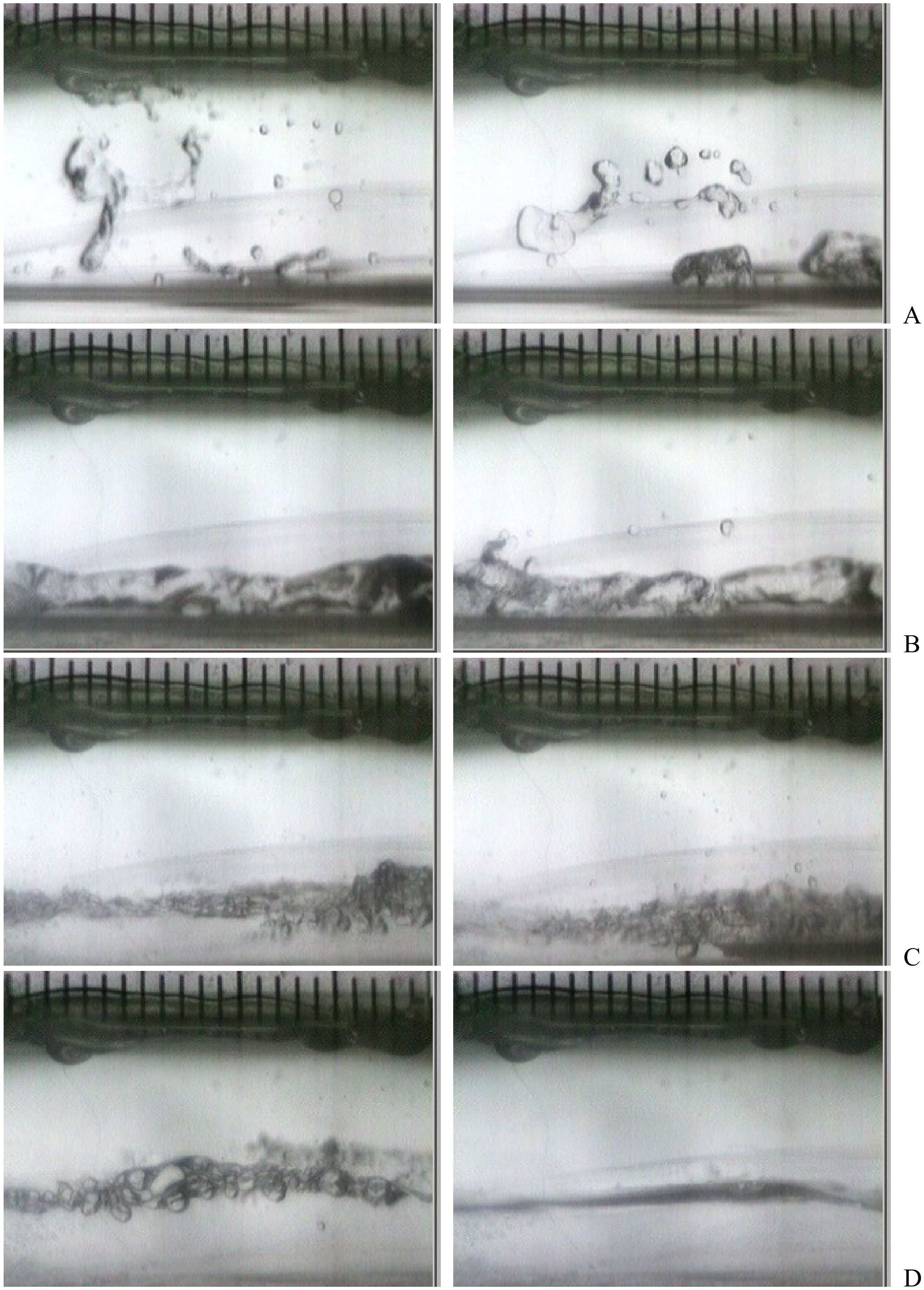

Figure 4-9. Flow visualizations at different stages of chilldown. A) Initial stage. B) Film boiling stage. C) Transition boiling stage. D) Nucleate boiling stage.

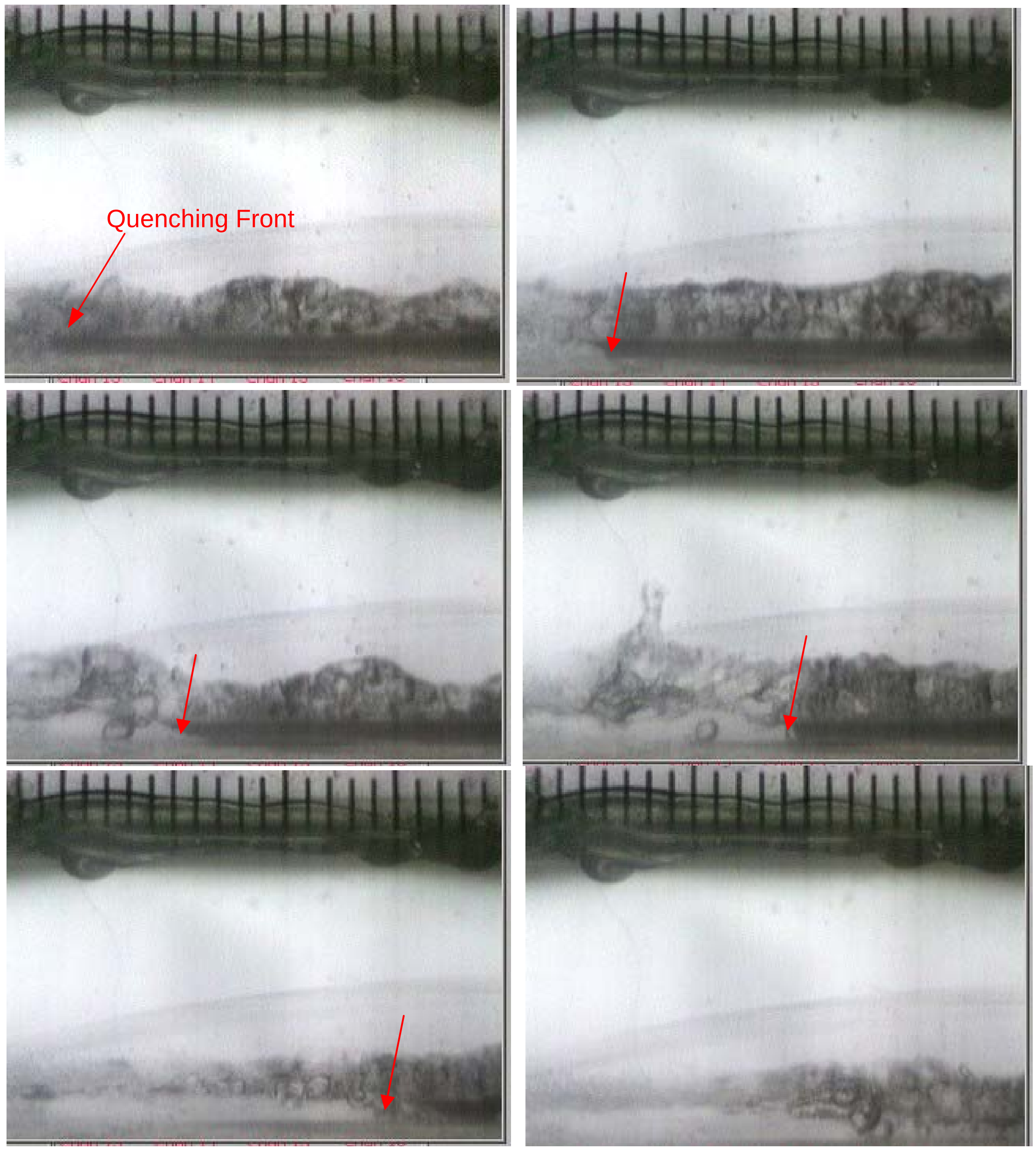

Figure 4-10. Propagation of the quenching front.

As shown in Figure 4-10, the quenching front is characterized by vehement bubble generation and intermittent liquid-wall contact. Following the quenching front, a continuous liquid-wall contact is established, the flow regime changes to stratified flow, and many nucleation sites are suppressed.

4.2 Bellows-Driven Experiment

4.2.1 Introduction

The flow rates in current bellows-driven experiments are very low. As a comparison, previous quenching experiments were generally conducted with flow rates higher than 40 $\mathrm{kg/m^2s}$. For example, the liquid nitrogen flow rate was in the range of 550-1940 $\mathrm{kg/m^2s}$ in the experiments of Antar and Collins (1997) and was 40.7-271.3 $\mathrm{kg/m^2s}$ in the experiments of Iloeje et al. (1982), while the flow rate of R-113 used by Westbye et al. (1995) was from 160 to 850 $\mathrm{kg/m^2s}$. No experimental work has been reported for cryogenic chilldown process under relatively low flow rate.

On the other hand, further understanding of the cryogenic chilldown process at low flow rate is of crucial importance for some applications, for example the cooling process in the TVS on a spacecraft. The mass flux in a TVS system is generally very low, in steady state test by Van Dresar et al. (2001, 2002) the nitrogen mass flux ranged from3.3 to 33 $\mathrm{kg/m^2s}$. The highly transient chilldown process under low flow condition has not been fully studied.

In present study a horizontal test section is quenched by the liquid nitrogen flow with mass flux form 3.6 to 10.8 $\mathrm{kg/m^2s}$, the flow regimes and heat transfer behavior are studied experimentally, and a phenomenological model is developed based on the experimental observations.

4.2.2 Visualization Study

The test section is initially at room temperature. The visualization study shows that in the film boiling region the flow regimes are similar to that illustrated in Figure 4-8. When the chilldown is initiated, the liquid phase is in the form of droplets that bounce back and forth on the bottom wall while traveling downstream. As the wall temperature decreases, the liquid droplets tend to form filaments and settle down on the bottom wall. Images of typical liquid filament at different mass fluxes are shown in Figure 4-11.

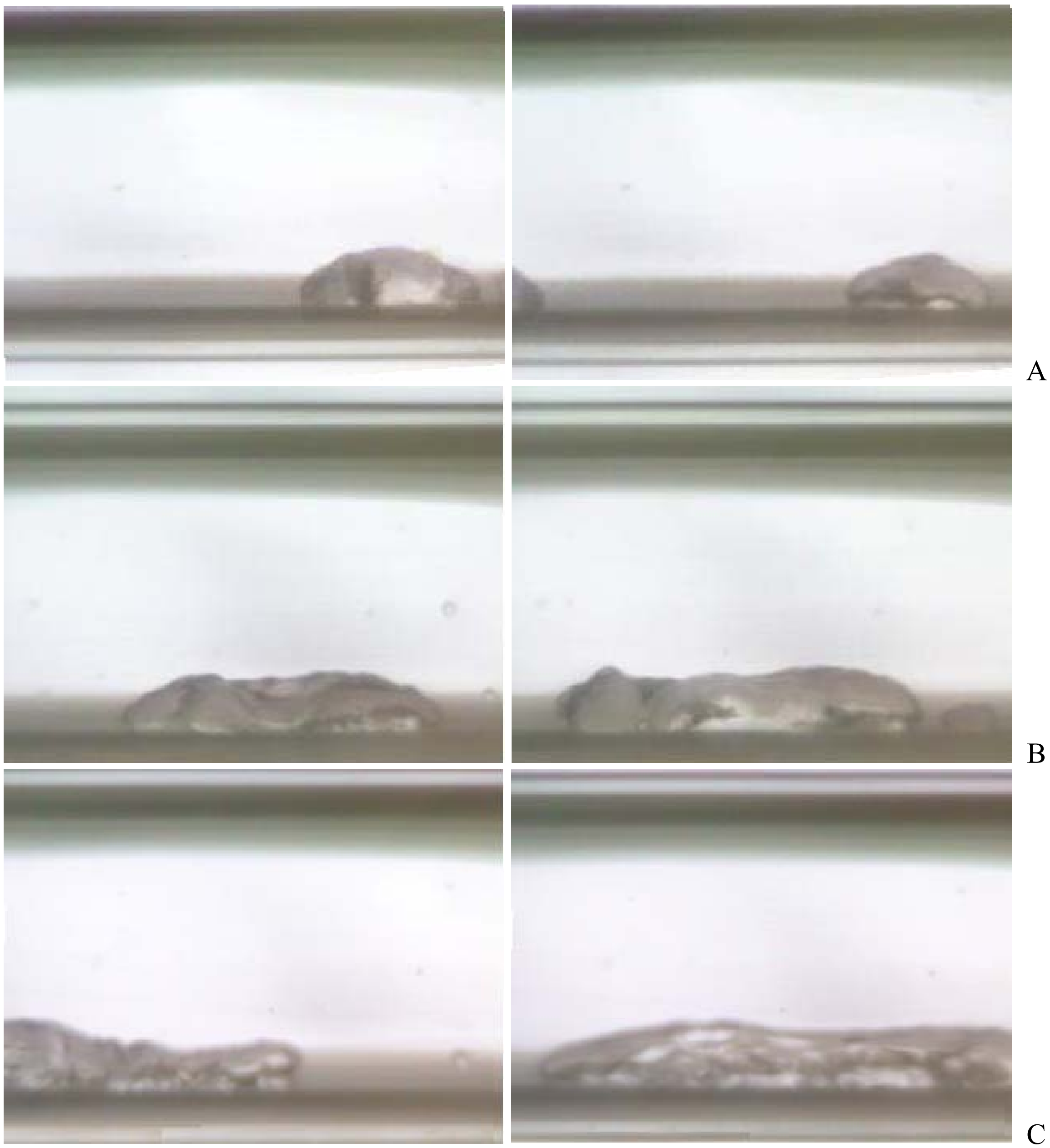

Figure 4-11. Typical flow images under different mass flux. A) Mass flux of 3.6kg/m^{2}s. B) Mass flux of 7.2 kg/m^{2}s. C) Mass flux of 10.8 kg/m^{2}s.

Generally, the thickness of the liquid filaments does not change much as the test section is chilled down; however, the length of the filaments increases with increasing mass flux and decreasing wall temperature. The drop-wall interaction from several experiments was summarized by Ganić and Rohsenow (1977). They listed the most frequently observed states of drop-wall interaction and the interaction sequence, as the wall is cooled down. Current observations generally agree with their summarization.

The statistic feature of the liquid filaments is shown in Figure 4-12 and Figure 4-13. It is clear that the thickness of the filaments shows very limited increase with increasing mass flux and does not present a strong correlation with the wall temperature; the length of the filaments, however, is more scattered at higher mass fluxes and lower wall temperatures. In other wards, the probability of observing a longer liquid filament is larger under higher mass flux and lower wall temperature.

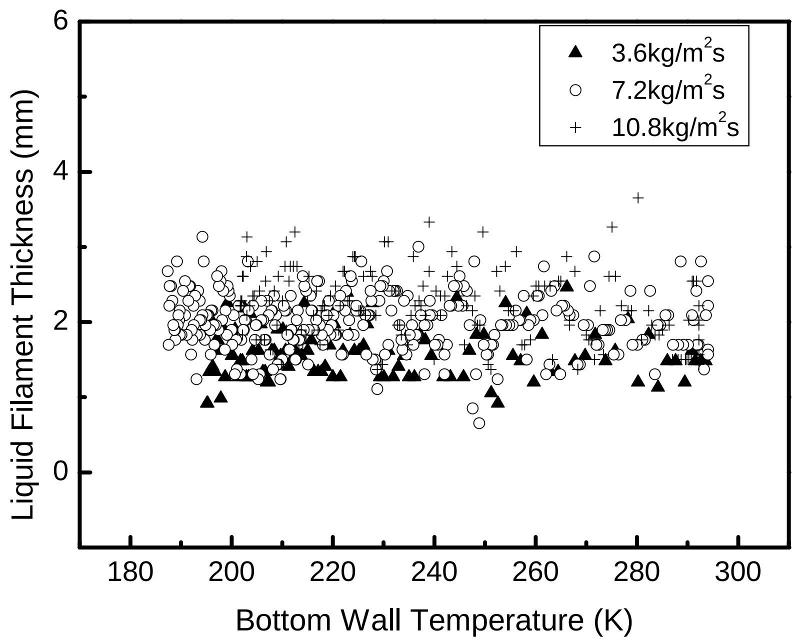

Figure 4-12. Thickness of the liquid filaments at different mass fluxes.

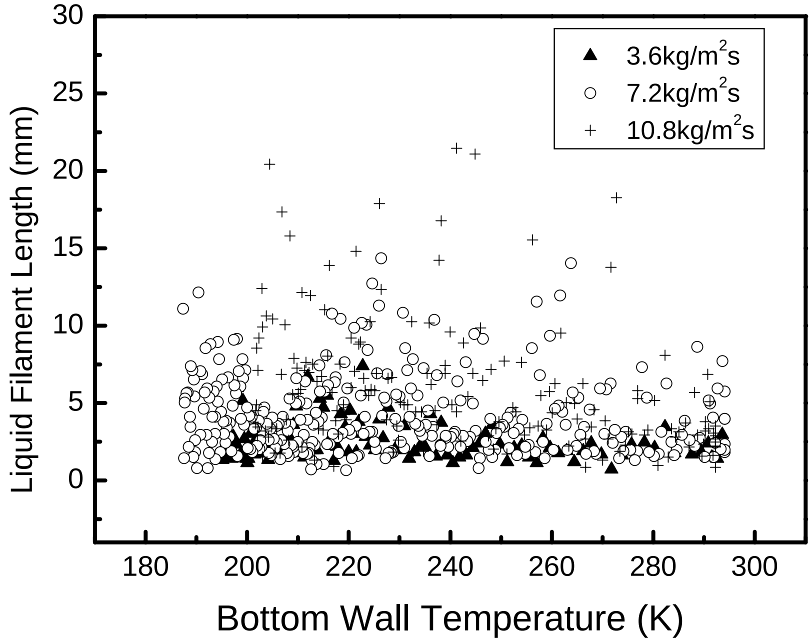

Figure 4-13. Length of the liquid filaments at different mass fluxes.

4.2.3 Heat Transfer Study

The temperature profiles measured from the embedded thermocouples at the inlet and the outlet cross-sections with different mass fluxes are shown in Figure 4-14 and Figure 4-15, respectively.

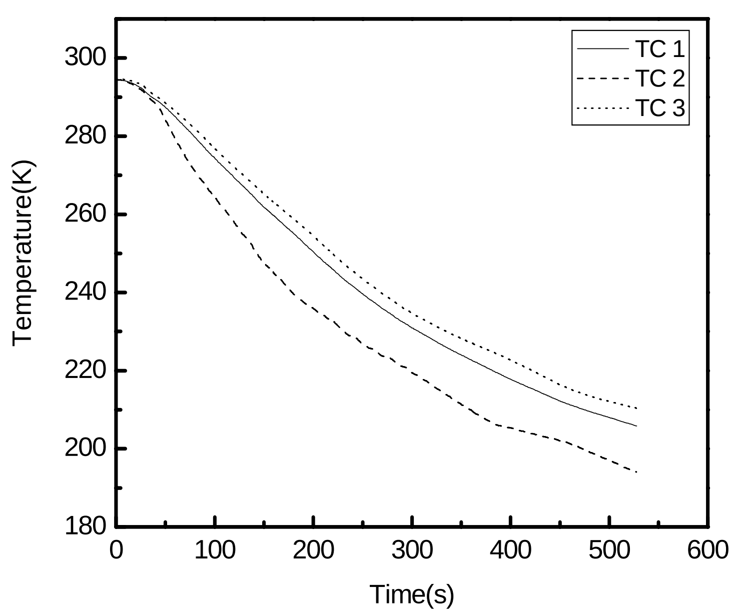

A

Figure 4-14. Temperature profiles of the inlet section with different mass flux. A) Mass flux of 3.6 kg/m^{2}s. B) Mass flux of 7.2 kg/m^{2}s. C) Mass flux of 10.8 kg/m^{2}s.

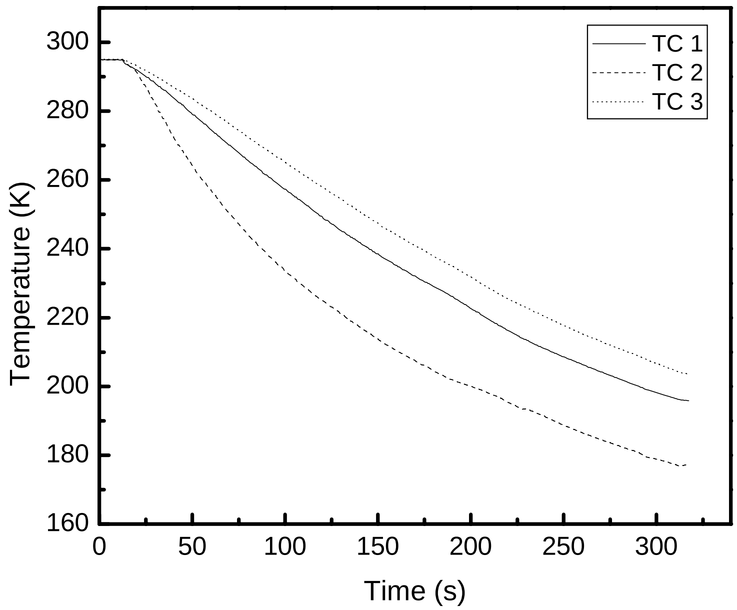

B

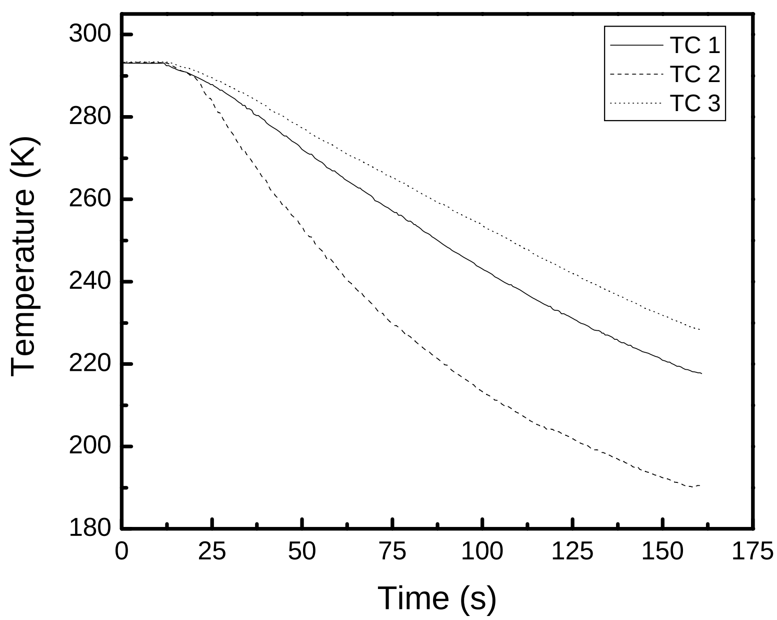

C

Figure 4-14. Continued.

It is obvious that the bottom wall of the test section is chilled down more quickly, because most of the liquid phase is confined at the bottom. The temperature difference between the bottom and the top of the test section is found to increase with increasing mass flux at each cross section.

The quality of the two-phase flow and vapor superheat generally increase along the test section, consequently, the temperature difference between the top and bottom wall is expected to be smaller at further downstream locations. This is confirmed by comparing Figure 4-14 with Figure 4-15.

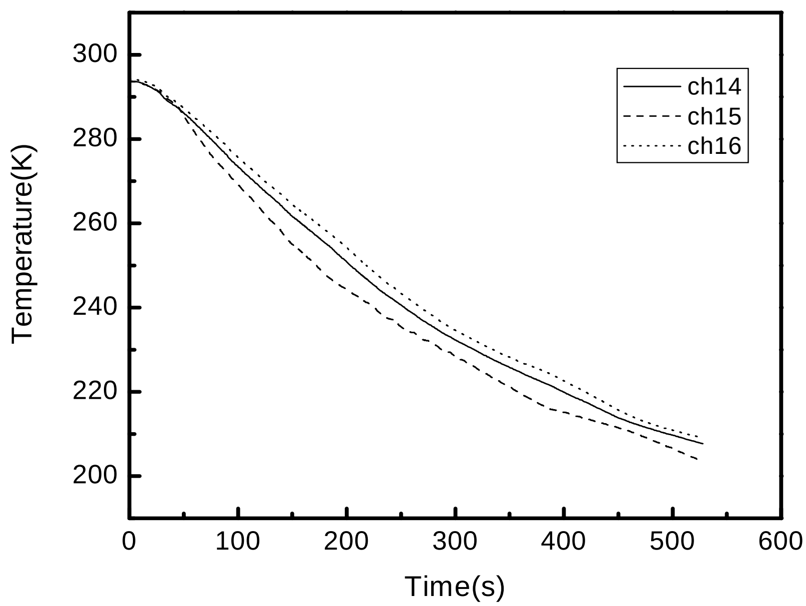

A

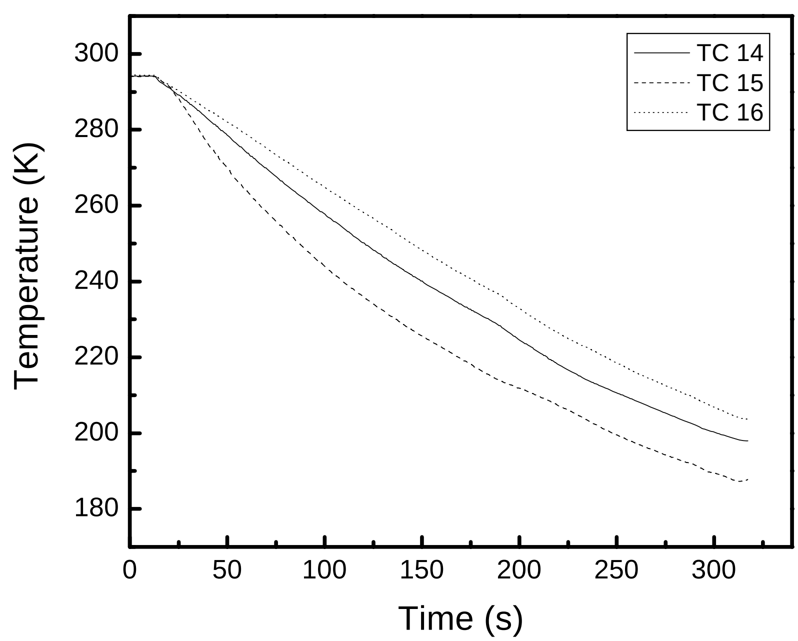

B

Figure 4-15. Temperature profiles of the outlet section with different mass flux. A) Mass flux of 3.6 kg/m^{2}s. B) Mass flux of 7.2 kg/m^{2}s. C) Mass flux of 10.8 kg/m^{2}s.

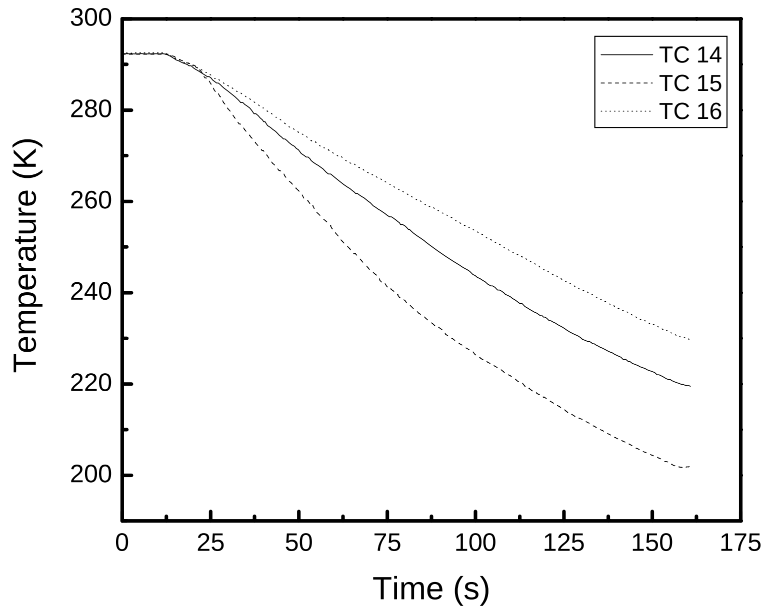

C

Figure 4-15. Continued.

The calculated middle section bottom wall heat fluxes under different mass fluxes are shown in Figure 4-16 as a function of the local wall temperature. The bottom wall heat fluxes first increase during the initial stage, and then decreases gradually with decreasing wall temperature.

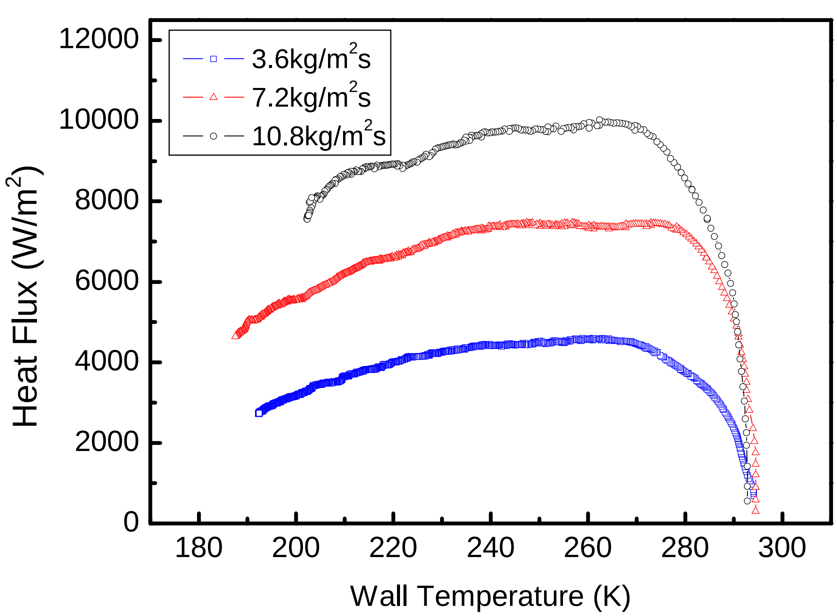

Figure 4-16. Middle section bottom wall heat fluxes under different mass fluxes.

Figure 4-17 shows the local heat fluxes at three circumferential locations at the middle cross-section as a function of local wall temperature under a mass flux of $7.2\,\mathrm{kg/m^2s}$. It is found that the two heat fluxes at the upper portion of the test section increase at the beginning during the chilldown process, and then maintain at almost constant values. The heat fluxes at the upper portion of the test section are much smaller than the bottom wall heat flux in a wide wall temperature range. Because the upper wall losses heat mainly by convection to the superheated vapor, while the main heat transfer mechanism at the bottom wall is film boiling, and is more efficient than convection.

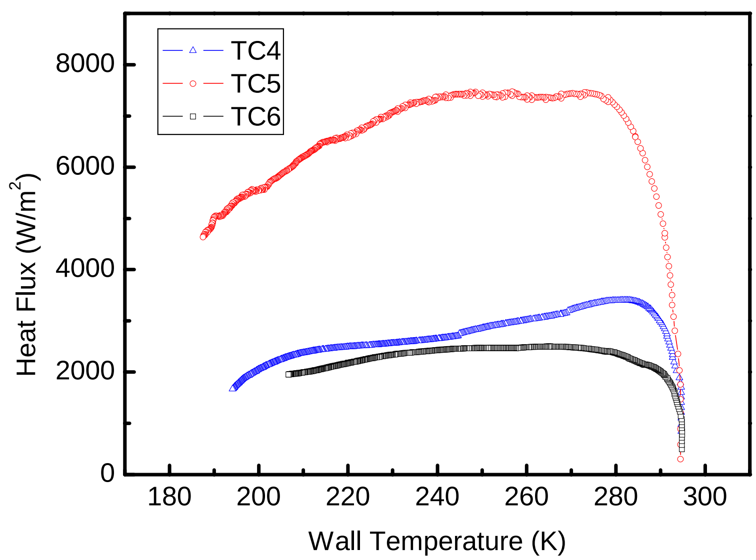

Figure 4-17. Middle section local wall heat fluxes under mass flux of 7.2 kg/m^{2}s.

4.2.4 Phenomenological Model of the Film Boiling Region

For dispersed flow film boiling (DFFB), it is widely accepted that a significant thermodynamic non-equilibrium condition exists between the vapor phase and the liquid phase (Laverty and Rohsenow 1967; Koizumi et al. 1978; Chen et al. 1979; Chung and Olafsson 1984; Tian et al. 2006). A model for vertical dispersed flow boiling suggested by Koizumi et al. (1978) assumed that heat transfer takes place in steps: from the wall to the vapor and then from the vapor to the droplets suspended in the stream; and from the wall to the droplets in contact with the wall. Chen et al. (1979) proposed a model for post-CHF region that considered the total heat transfer as a sum of vapor and liquid components and ignored radiation heat transfer to the two-phase mixture.

During the chilldown process, the inlet quality and vapor superheat are not constants but change with time and mass flux, and are hard to identify from the experiments. Therefore, a phenomenological model, which also includes information form visualization results, is developed to analyze the dispersed flow boiling heat transfer.

4.2.4.1 Model description

As mentioned before, the visualization shows that except in the very beginning stage, most of the liquid filaments are flowing along the bottom of the tube. Consequently, in this model the heat transfer mechanism at the bottom of the test section is considered as the sum of vapor and liquid components, while the heat transfer mechanism at the upper portion of the test section is forced convection to superheated vapor. It has been shown (Guo and Mishima 2002; Tian et al. 2006) that for wall superheat up to several hundreds Kelvin the radiation heat transfer in post-dryout dispersed flow is generally negligibly small. It is also judged that thermal radiation is minor in our case; therefore radiation heat transfer is ignored in this model.

The heat transfer mechanisms in this model are illustrated in Figure 4-18. As an idealization, the liquid filaments are modeled as half cylinders in a film boiling state and move along the bottom of the tube. The filaments are at the saturation temperature and separated from the tube wall by a thin vapor film. The bottom wall heat flux is a sum of vapor and liquid components, and can be written as:

$$q''_b = q''_{b1}F_L + q''_{b2}\left(1-F_L\right) = q''_{fb}F_L + q''_{b,\,con}\left(1-F_L\right) \tag{4.8}$$

where q''_b is the effective bottom wall heat flux, and q''_{fb} is the heat flux from the portion of the bottom surface where a liquid filament is in the vicinity and separated from the wall by a thin vapor film, therefore, q''_{fb} is a film boiling heat flux. $q''_{b,\,con}$ is the heat flux from the bottom surface where there is no liquid filament around, so it is due to pure forced convection to the superheated vapor. F_L is defined as the time averaged fraction of bottom wall surface that is associated with liquid filaments.

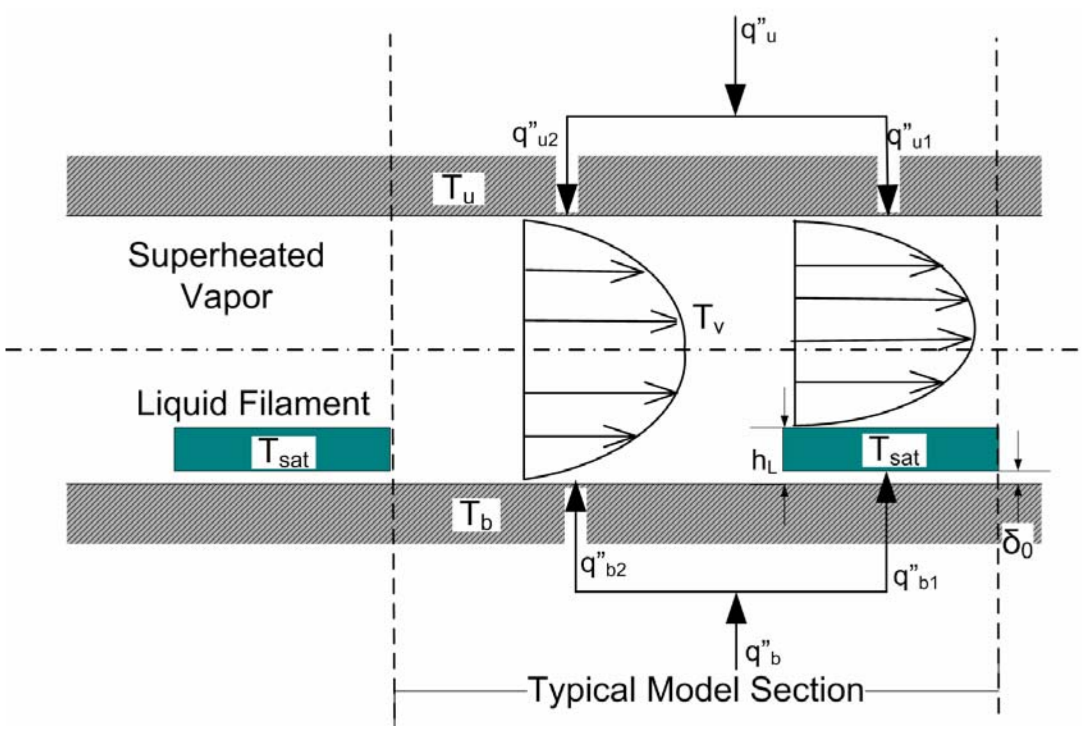

Figure 4-18. Description of the heat transfer mechanism under horizontal dispersed flow condition.

The upper wall of the test section is fully in contact with the vapor phase, and the upper wall heat flux is described as:

$$q''_u = q''_{u1}F_L + q''_{u2}(1-F_L) = q''_{u,\,con1}F_L + q''_{u,\,con2}(1-F_L) \tag{4.9}$$

where q''_u is the effective upper wall heat flux, and $q''_{u,\,con1}$ is the convective heat flux to the superheated vapor for the portion that is directly opposite to the bottom portion that is associated with liquid filaments as shown in Figure 4-18. $q''_{u,\,con2}$ is for the portion that is directly opposite to the bottom portion that is not associated with liquid filaments. $q''_{u,\,con1}$ and $q''_{u,\,con2}$ are different due to different bulk vapor velocities in their respective sections.

The fractional of liquid filament associated area F_L is expected to increase with increasing mass flux and decreasing wall temperature. The transient liquid fractions in recorded frames are widely scattered. Therefore F_L is calculated by averaging over a certain time period, the result is shown in Figure 4-19. The fitted linear curves in Figure 4-19 are used in the model calculation.

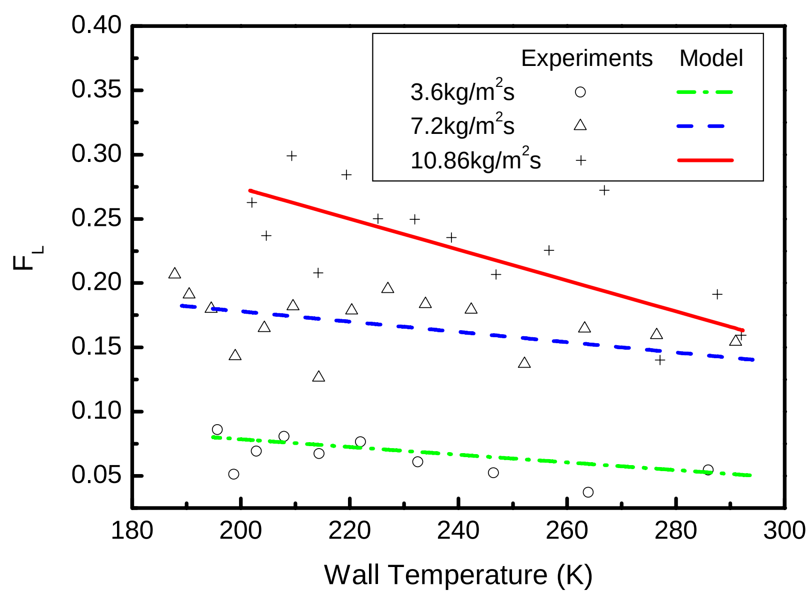

Figure 4-19. Fractional of liquid filament associated area at different wall temperature and mass flux.

Another information referred from the recorded images is the local void fraction α. Generally, the vapor film between the liquid filament and the tube wall is very thin, therefore at a cross-section that contains liquid filament, the local void fraction can be approximately expressed as:

$$\alpha = 1 - \left(\frac{\arccos(1 - h_L/R) - (1 - h_L/R)\sqrt{2h_L/R - (h_L/R)^2}}{\pi} \right) \tag{4.10}$$

here, h_L is the measured thickness of the liquid filament, and *R* is tube inner radius.

The forced convective heat transfer to the vapor phase is evaluated by Dittus-Boelter equation as:

$$q''_{con} = 0.023 \frac{k_v}{D} Re_D^{0.8} Pr^{0.4} (T_w - T_v) \tag{4.11}$$

in which k_v is the vapor phase thermal conductivity; D is the hydraulic diameter of the vapor flow; Re_D is Reynolds number; Pr is the vapor Prandtl number; T_w and T_v are the wall temperature and balk vapor phase temperature, respectively. It is noted that both $q''_{u,\,con1}$ and $q''_{u,\,con2}$ are evaluated using Equation 4.10, the difference is that each is evaluated based on the respective bulk vapor velocity in its section as shown in Figure 4-18. For the cross-section contains only vapor phase, the vapor velocity is simply evaluated by:

$$u_v = G/\rho_v \tag{4.12}$$

in which *G* is the mass flux, while for the cross section contains both liquid filament and vapor phase, the vapor velocity is calculated by:

$$u_v = G/\left[\rho_v \alpha + \rho_l (1-\alpha)/S\right] \tag{4.13}$$

where *S* is two phase slip velocity, it is defined as u_v/u_l , and can be evaluated as (Zivi 1964):

$$S = (2.5\,\rho_l/\rho_v)^{1/3} \tag{4.14}$$

In current model, upper wall heat flux is described as containing only convective heat transfer; the vapor phase temperature can be calculated by matching the measured upper wall heat flux. Then the bottom heat flux can be calculated from Equation 4.8 if the film boiling heat flux to the liquid filament q''_{fb} is known. The correlation used to evaluate this heat flux is given below.

4.2.4.2 Film boiling correlation

Film boiling, in which a thin vapor film blankets the heating surface due to the high wall superheat, is often encountered in the handling of cryogenic fluids. Many studies have been conducted on stable film boiling on external geometries, such as vertical surface, (Bromley 1950; Chang 1959) horizontal surface (Bromley 1950; Chang 1959; Berenson 1961), outer surface of horizontal cylinders (Bromley 1950; Breen and Westwater 1962), and spheres (Merte and Clark 1964; Frederking et al. 1964). However, not enough effort has been paid to film boiling inside of a horizontal tube, which is common in engineering systems, the known investigations include research work by Chan (1995) and Liao (2005). In both of these two works, it was assumed that the vapor phase flows in a thin channel as shown in Figure 4-20, and a linear temperature profile exists in the vapor layer, then an analytical solution of the local vapor film thickness δ and vapor velocity in the vapor channel in the circumferential direction were derived, and the local film boiling heat transfer coefficient was obtained as:

$$h_{fb} = \frac{k_g}{\delta} \tag{4.15}$$

here, to differ from the vapor phase that is not inside of the vapor film, subscript g is used to denote the gas in the vapor film.

In Liao's study (2005), the vapor flow was simplified to boundary-layer type flow, and by neglecting the vapor thrust pressure and surface tension, the film boiling heat transfer coefficient was given as:

$$h_{fb} = \frac{k_g}{\delta} = 0.6389 \frac{k_g}{DF(\theta)} \left(\frac{\text{Ra}}{\text{Ja}} \right)^{\frac{1}{4}} \tag{4.16}$$

in which $\text{Ra} = gD^3 \left(\rho_l - \rho_g \right) / \mu_g \rho_g$ is the Raleigh number, $\text{Ja} = C_{pg} \left(T_w - T_s \right) / h_{\text{lg}}$ is the Jacob number, and $F(\theta)$ is a geometry influence factor needs numerical integration.

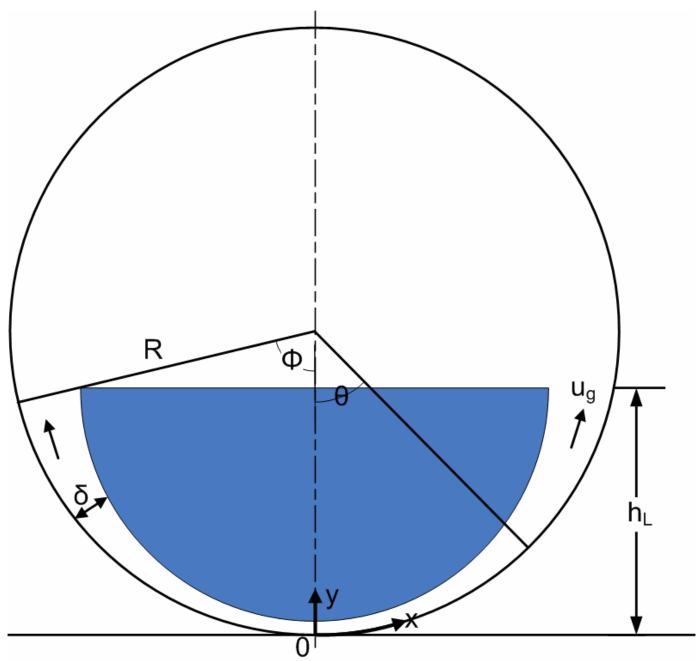

Figure 4-20. Stable film boiling inside a horizontal tube.

As a comparison, in deriving the analytical solution for film boiling inside a horizontal tube, Chan (1995) included the vapor thrust effect but assumed a constant vapor velocity in the cross section of the vapor channel, and obtained a simpler expression for the heat transfer coefficient at the bottom of the tube. In this derivation the interfacial velocity is assumed to be half of the vapor velocity, however, in most of the research works, the interfacial velocity is assumed to equal the liquid phase velocity, which is often much smaller than the vapor velocity. Therefore, in current study, the interfacial velocity is assumed to be zero. The vapor film thickness and the vapor velocity are then calculated based on this modified boundary condition. For stable film boiling of liquid nitrogen inside a horizontal tube, Figure 4-21 shows typical results for different liquid level h_L.

One can find that approximately in the first half of the vapor channel, the vapor film thickness remains almost a constant value, and the vapor velocity increases linearly; while in the second half of the channel, the vapor film thickness increases very fast accompanied with a fast decrease of the vapor velocity, and the vapor velocity drops to zero at the top of the liquid filament.

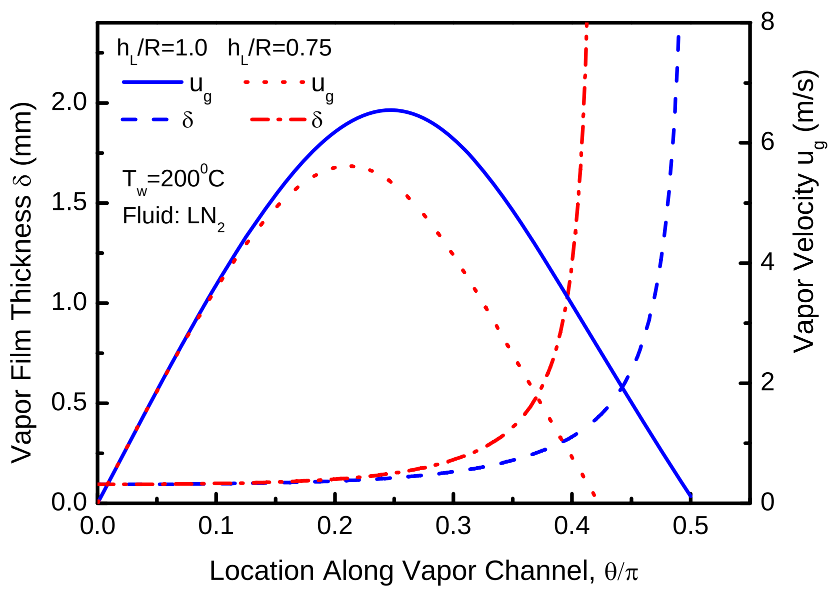

Figure 4-21. Vapor film thickness and vapor velocity along the vapor channel.

Calculation of the local vapor film thickness and vapor velocity requires numerical solution as finite difference method (Chan 1995), however, a simple expression exists for the vapor film thickness at the bottom of the tube as:

$$\delta_0 = 1.189\left[\left(\frac{R}{g\rho_l\rho_g}\right)\left(\frac{k_g\Delta T_w}{h'_{lg}}\right)^2\right]^{\frac{1}{4}} \tag{4.17}$$

in which ΔT_w is the wall superheat, and h'_{lg} is defined as the latent heat plus vapor sensible heat content:

$$h'_{lg} = h_{lg} + 0.5C_{pg}\Delta T_w \tag{4.18}$$

It should be noted that in the above equations, all the thermodynamic properties of the gas in the vapor film are evaluated at an average film temperature given by:

$$T_g = 0.5(T_w + T_{sat}) \tag{4.19}$$

Because the vapor film remains essentially constant over a relatively long distance from the bottom of the tube as shown in Figure 4-21, the heat transfer to the liquid filament at the bottom of the tube can be evaluated by:

$$q''_{fb} = k_g\frac{\Delta T_w}{\delta_0} \tag{4.20}$$

4.2.4.3 Model evaluation

The phenomenological model described above permits calculation of bottom wall heat flux with known upper wall heat flux. Figure 4-22 compares the experimental results with the model prediction of the bottom wall heat fluxes at the outlet section under different mass fluxes.

It is seen that the model over predicts the heat fluxes in the beginning stage of chilldown, after that the model is reasonably accurate. The flow visualization shows that in the beginning stage the liquid droplets bounce back and forth on the wall rather than settle down on the bottom wall, therefore the above film boiling model with a stable liquid filament in the wall vicinity is not adequate for the beginning period. Because of the much higher heat flux for a stable film boiling condition than that of bouncing liquid droplets, the current model over-predicts the heat transfer in the beginning stage.

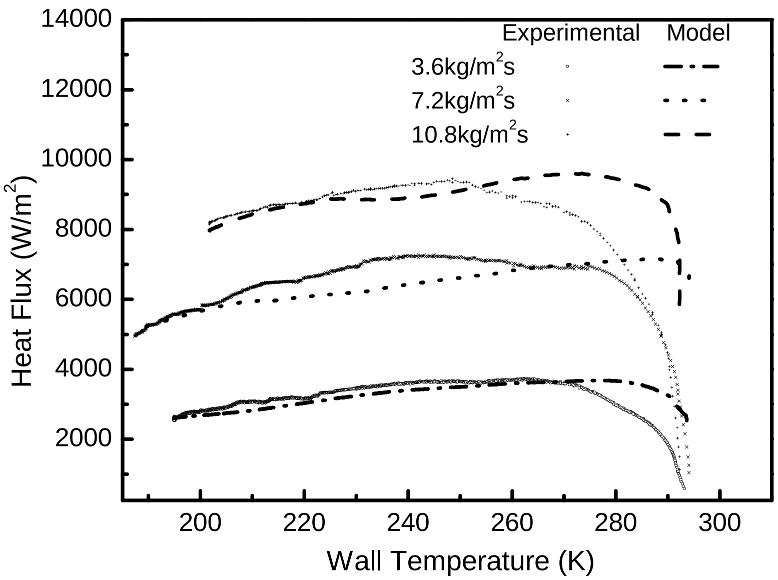

Figure 4-22. Comparison between experimental and model results of the bottom wall heat fluxes at outlet section.

4.3 Rewetting Experiment

Rewetting is the establishment of liquid-wall contact and characterizes the transition from film boiling to transition boiling. Early researchers tend to believe that the liquid will contact the hot surface at a fixed temperature usually called Leidenfrost temperature, however, more and more results show that there is no unique temperature at which a hot surface will rewet, instead, the rewetting temperature is a function of many thermal, hydrodynamic and geometric parameters pertinent to the system (Chan and Banerjee 1981a, Abdul-Razzak et al. 1992, Barnea et al. 1994). In this section, the rewetting phenomenon is experimentally investigated by pre-cooling and then quenching the test section with different mass fluxes.

4.3.1 Types of Rewetting

Rewetting phenomenon is rather complex and involves the interaction among the liquid phase, vapor phase, and the solid wall. Iloeje et al. (1975) was the first one who successfully isolated three different controlling mechanisms for forced convective rewet. These are: impulse cooling collapse, axial conduction controlled rewet and dispersed flow rewet.

The impulse cooling collapse was proposed as the controlling mechanism for the IAFB region, in which the liquid-vapor interface is wavy and fluctuates about a mean position. If the wall temperature or heat flux is lowered, the vapor thickness decreases and eventually the liquid may contact the wall. Depending on the temperature and the wall heat flux, permanent liquid-wall contact is either maintained or the liquid will be pushed away from the surface with the formation of vapor. In the second case, each liquid-wall contact is equivalent to an impulsive cooling of the surface. For a chilldown process, repeated contacts will lower the surface temperature enough to permit rewet. Recent experiments (Cokmez-Tuzla et al. 2000) employed a special rapid-response probe validate this impulsive liquid-wall contact in film boiling region. Some researchers (Chan and Banerjee 1981b, Adham-Khodaparast et al. 1995) used the Kelvin-Helmhlotz instability to explain the growth of the interfacial wave. Based on this controlling mechanism, Kalinin et al. (1969) proposed that the wall temperature corresponding to the minimum heat flux can be obtained from their empirical correlation:

$$\frac{T_{\min}-T_s}{T_{crit}-T_l}=1.65\left(0.16+2.4\left[\frac{(k\rho c)_l}{(k\rho c)_w}\right]^{0.25}\right) \tag{4.21}$$

in which, T_{crit} is the thermodynamic critical temperature, subscript *l* is for liquid and *w* is for wall. The hydrodynamic parameter of the flow rate is, however, completely absent in this model.

In a system with an already wetted upstream surface, Simon and Simoneau (1969) suggested that the transition from the film boiling to nucleate boiling is governed by axial conduction. They assumed that the rewet temperature is a thermodynamic property of the fluid, and is determined by using the Van der Waals equation of state (Spiegler et al. 1963):

$$\frac{T_{rw}}{T_{crit}} = 0.13\frac{p}{p_{crit}} + 0.84 \tag{4.22}$$

here, T_{rw} denotes the rewet temperature, p_{crit} is the critical pressure.

In dispersed flow regime, Iloeje et al. (1975) postulated that rewetting was controlled by the limiting effects of two processes, namely, heat transfer to the vapor assuming no effect of the existence of droplets, and heat transfer due to the presence of the droplets, which may or may not be touching the surface. The sum of the two heat transfer components gives the total heat flux and indicates the location of the minimum heat flux and $T_{\min}$.

4.3.2 Rewetting Temperature and Rewetting Velocity

The local wall temperature at the onset of rewetting is very important for theoretical modeling and engineering applications. Many definitions have been used in the literature, such as rewetting temperature, apparent quenching or rewetting temperature, minimum film boiling temperature, Leidenfrost temperature, etc. In different investigations, usually one of the above definitions was selected according to the experimental configuration. This partly reflects the limited understanding on rewetting phenomenon.

Figure 4-23 shows a typical chilldown boiling curve and the corresponding transient wall temperature. Since the liquid-wall contact indicates the end of the film boiling, the rewetting temperature should be defined as the minimum film boiling temperature $T_{\min}$, which corresponds with the minimum film boiling heat flux, as shown in Figure 4-23.

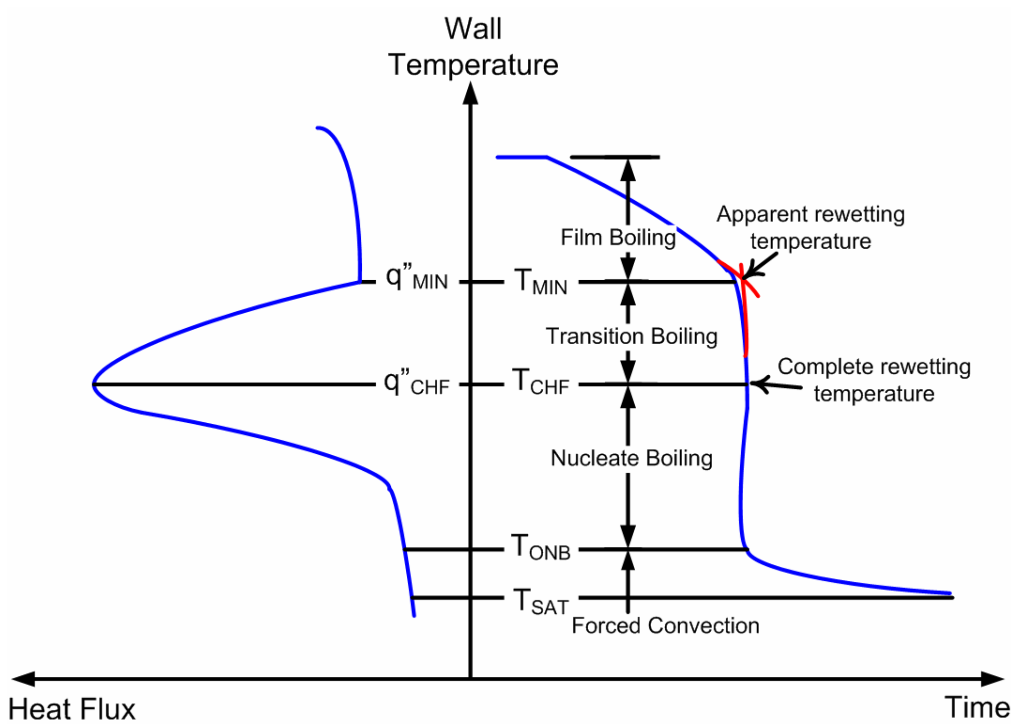

Figure 4-23. A typical chilldown boiling curve and the corresponding transient wall temperature.

However, the apparent rewetting temperature, which is the intersection of tangent lines to the “knee” of the measured temperature-time trajectories, was also used by many researchers (Chen et al. 1979, Abdul-Razzak et al. 1992, Barnea et al. 1994, Westbye et al. 1995). Other definitions of rewetting temperature include the temperature at the “knee” of the temperature-time trajectory (Iloeje et al. 1982) and complete rewetting temperature defined at the CHF point (Adham-Khodaparast et al. 1995). The rewetting temperatures from those above definitions are generally not equal. In current test, it is shown that the wall temperature has an abrupt decrease at the rewetting point; therefore the temperature at the "knee" of the temperature-time trajectory is used to define the rewetting temperature.

Typical temperature profiles of a rewetting test are shown in Figure 4-24. The test section is pre-cooled to certain temperature and then quenched by injecting liquid nitrogen from the bellows with constant mass flux. The wall temperatures decrease very slowly at the beginning and then drop abruptly at the rewetting point.

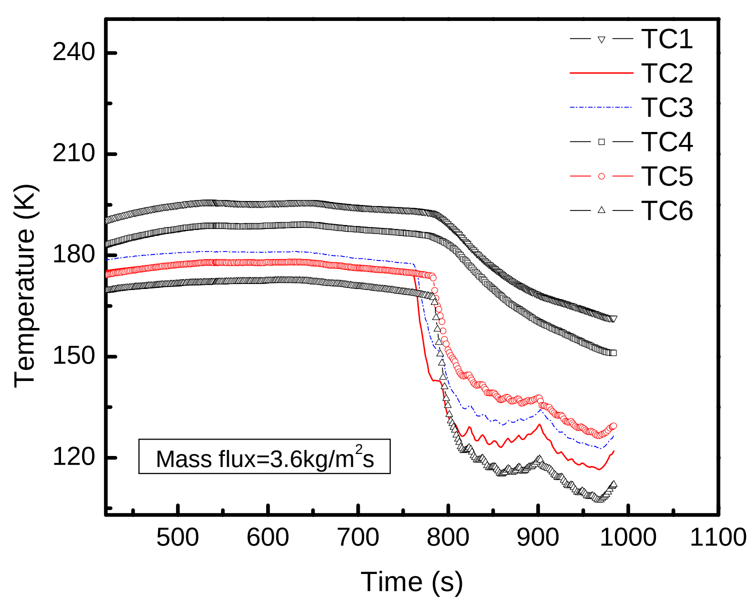

Figure 4-24. Typical temperature profiles during a rewetting test.

The axial variation of the averaged rewetting temperature at the bottom of the tube under different mass fluxes is illustrated in Figure 4-25. The rewetting temperature increases with increasing mass flux; this has also been reported in high mass flux experiments (Chan and Banerjee 1981a, Abdul-Razzak et al. 1992, Westbye et al. 1995, Xu 1998). It was proposed by Xu (1998) that the vapor film thickness would decrease at higher mass flux, and therefore lead to rewetting at a higher wall temperature. No clear trend of axial variation is shown in Figure 4-25.

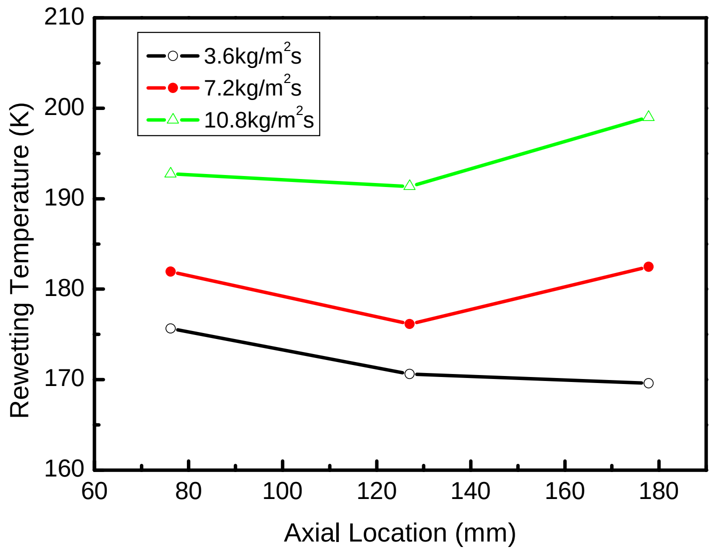

Figure 4-25. Axial variation of the averaged rewetting temperature at different mass fluxes.

Although it is quite complicated and difficult to fully analyze the rewetting phenomenon, many researchers have tried to predict rewetting temperature by theoretical models and experimental correlations. Berenson (1961) extended Zuber's vapor escape mode1 to analyze the minimum heat flux condition in steady film boiling over a flat horizontal surface. The heat transfer through the vapor film was described as a pure heat conduction problem, and the following correlation was obtained to predict the minimum film boiling temperature for pool boiling:

$$\Delta T_{\min} = 0.127 \frac{\rho_v h_{lv}}{k_v} \left(\frac{g(\rho_l - \rho_v)}{(\rho_l + \rho_v)} \right)^{\frac{2}{3}} \left(\frac{\sigma}{(\rho_l - \rho_v)} \right)^{\frac{1}{2}} \left(\frac{\mu_v}{g(\rho_l - \rho_v)} \right)^{\frac{1}{3}} \qquad (4.23)$$

The minimum film boiling temperature calculated from Equation 4.23 is 142.3K. The impulse cooling collapse model (Kalinin et al. 1969), which is given in Equation 4.21, considers the properties of the solid wall and gives a minimum film boiling temperature of 189.97K, which is close to the experimental values. Predicted rewetting temperature from the axial conduction model is only 106.4K, which is much less than the present data. Under current experimental condition, long liquid filaments are observed to flow at the tube bottom, the impulse cooling collapse model was proposed for IAFB and therefore gives a better result over the axial conduction model.

The flow rate effect has not been shown in the above correlations; however, as mentioned before all the previous experiments indicated the rewetting temperature also depends on hydrodynamic parameters. Iloeje et al. (1975) conducted vertical flow boiling experiments with water in an inconel tube and observed minimum film boiling superheats asymptotically approaching certain values. They suggested that this asymptote would be close or equal to a pool boiling value and correlated their data in the following empirical form:

$$\Delta T_{\min} = \Delta T_{m,Ber}\left(1 - Ax^{n}\right)\left(1 + BG^{m}\right) \tag{4.24}$$

where $\Delta T_{m,Ber}$ is Berenson's minimum film boiling temperature for pool boiling (Equation 4.23), x is quality, G is mass flux, A, B, m and n are constants. Xu (1998) used R113 to quench a hot surface and suggested a similar form as Equation 4.24 to correlate his experimental data as:

$$\Delta T_{\min} = \Delta T_{m,Ber}\left(1 + BG^{m}\right) \tag{4.25}$$

A correlation similar in the form of Equation 4.25 is used in current study, with the same exponent as Iloeje et al. (1975), the best fit is obtained as:

$$\Delta T_{\min} = \Delta T_{m,Ber}\left(1 + 0.242G^{0.49}\right) \tag{4.26}$$

The prediction results from all the above correlations and the experimental data are compared in Figure 4-26.

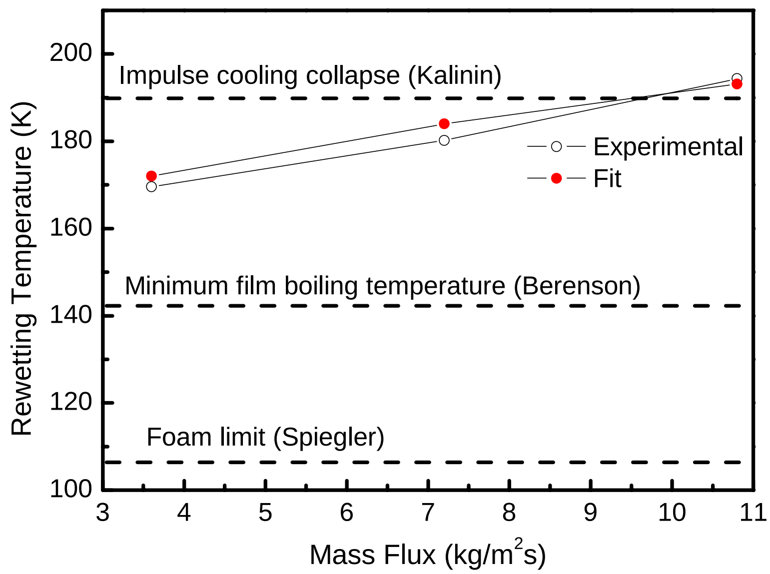

Figure 4-26. Comparison of rewetting temperatures between experiments and different correlations.

The propagation speed of the QF or the rewetting velocity can be determined as the axial distance between the thermocouple locations divided by time difference of the rewetting time (Chan and Banerjee 1981a). Figure 4-27 shows the average rewetting velocity under different mass fluxes.

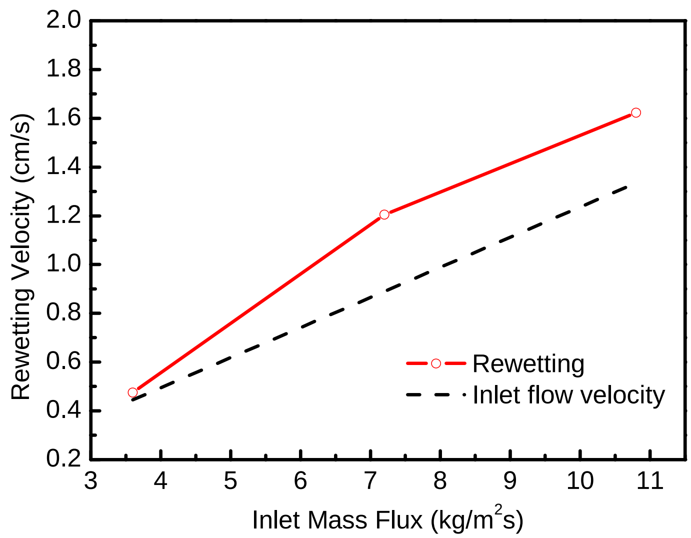

Figure 4-27. Average rewetting velocity under different mass fluxes.

The rewetting velocity is larger than the inlet velocity and increases with increasing mass flux. The difference between the rewetting velocity and the inlet velocity is larger under higher mass flux.

4.3.3 Visualization Study

According to impulse cooling collapse model, the liquid-wall contact is not the sufficient condition that leads to the surface rewet. For rewet phenomenon to occur, the surface temperature must be lower enough to allow the liquid-wall contact to spread.

Chan and Banerjee (1981c) also suggested that the rewetting was due to not only the breakup of the liquid-vapor interface but also the growth and spread of the rewet spots. The visualized images for the rewet process, which are shown in Figure 4-28 in time sequence, tend to support this hypothesis. The flow direction is from left to right with a mass flux of $3.6\,\text{kg/m}^2\text{s}$.

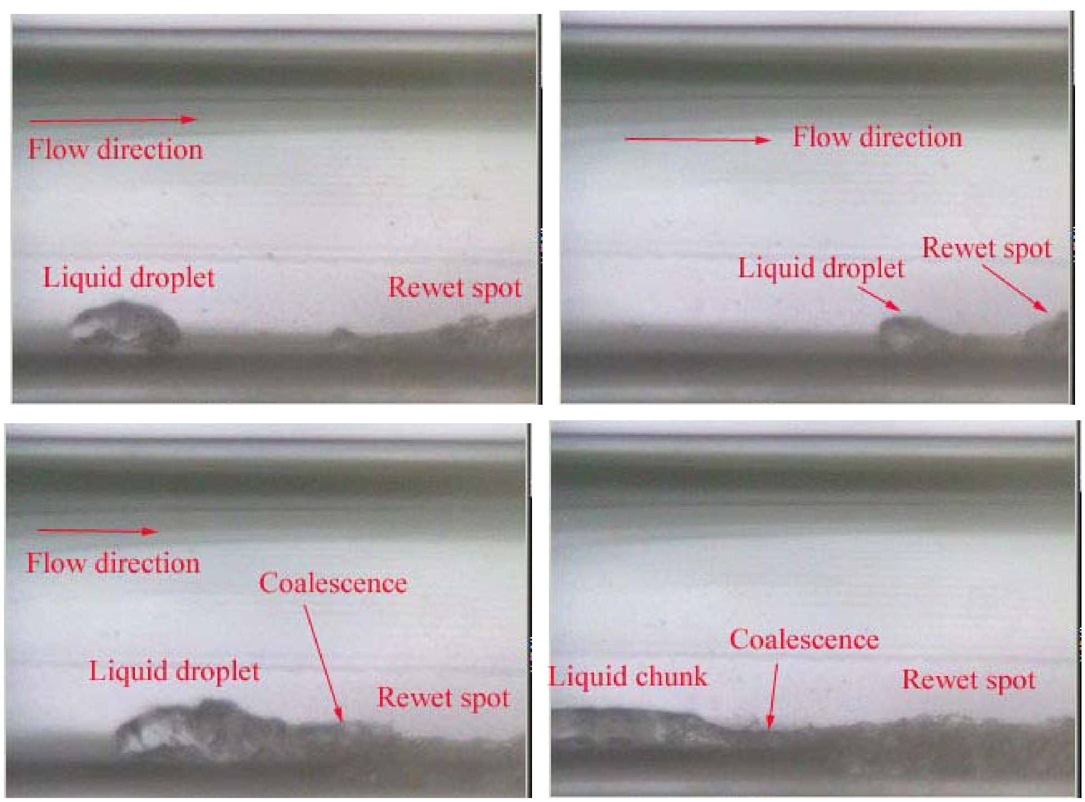

Figure 4-28. Visualization result of the rewet process.

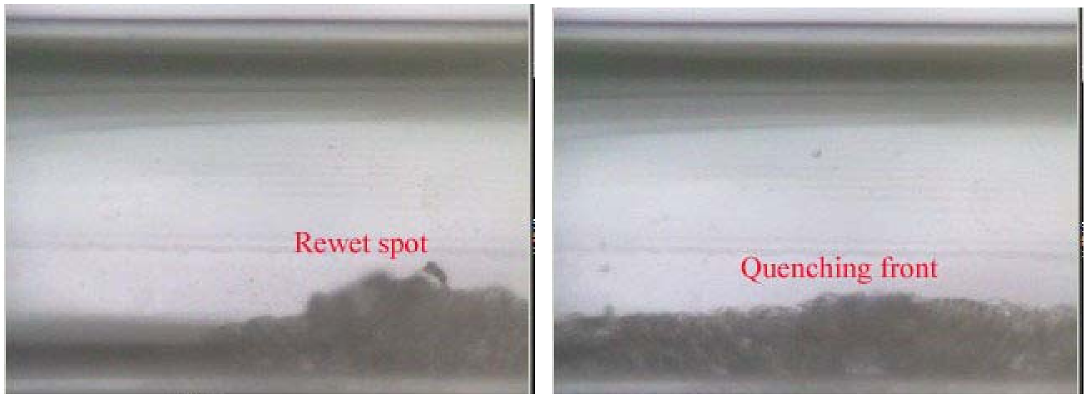

Figure 4-28. Continued.

The rewet spots, which are foam-like chunks consists by many small bubbles, first appear at some local points. After generation, they grow and spread in both direction while being drifted downstream at the same time. Liquid droplets or liquid filaments are observed to coalesce with the rewet spots. The tube wall is then covered by a foamy mixture of bubbles with wavy interface, which is known as quenching front. The nucleate boiling beneath the quenching front is highly transient, as the wall temperature decreasing rapidly the liquid nitrogen begins to contact the wall and many nucleation sites are suppresses.

CHAPTER 5
CRYOGENIC TWO-PHASE CHILLDOWN UNDER MICROGRAVITY CONDITION

Efficient and safe utilization of cryogenic fluids in a spacecraft during space missions demands thorough study of cryogenic two-phase flow and heat transfer under microgravity condition. However, researches on this field are very limited due to the experimental difficulties. In present study, experimental study of cryogenic chilldown under microgravity condition is conducted. The investigation focuses on the film boiling region.

5.1 Introduction

5.1.1 Film Boiling under Microgravity

Among the various film boiling correlations for pool boiling, it is very interesting to note that the surface heat flux or heat transfer coefficient is usually correlated with $g^{1/4}$, in which g is the gravitational acceleration. For example, the highly cited Bromley's correlation (Bromley 1950) for horizontal tubes is:

$$h_{fb} = 0.62\left[\frac{k_v^3 h'_{lv}\rho_v g\left(\rho_l - \rho_v\right)}{\mu_v D \Delta T_w}\right]^{1/4} \tag{5.1}$$

For horizontal surface, the mostly used correlation gives (Berenson 1961):

$$h_{fb} = 0.425\left[\left(\frac{k_v^3 h'_{lv}\rho_v g\left(\rho_l - \rho_v\right)}{\mu_v \Delta T_w}\right)\left(\frac{g\left(\rho_l - \rho_v\right)}{\sigma}\right)^{1/2}\right]^{1/4} \tag{5.2}$$

in which the $\left(g\left(\rho_l - \rho_v\right)/\sigma\right)^{1/2}$ term is actually a geometrical factor as pointed out by Berenson (1961), and has the dimension of [m^{-1}], thus in Equation 5.2 the film boiling heat transfer coefficient is still proportional to $g^{1/4}$. Liao (2005) and Chan (1995) also got the same relation, as shown in Chapter 4. The list also includes the correlations given by Noyes (1963), Chang and Snyder (1960), etc. The only exception, to the author's knowledge, is the correlation proposed by Chang (1959), in which the film boiling heat transfer coefficient is suggested to be proportional to $g^{1/3}$.

It is also noted that some of the above correlations were derived based on quite different approaches, such as analytical solution of flow in vapor film channel (Chan 1995; Liao 2005) and vapor escape model based on Taylor-Helmholtz instability (Berenson 1961). Therefore, it is natural for one to think that the heat transfer characteristic in film boiling is related to $g^{1/4}$ and extend the above correlations to different g-level. For example, the Bromley's correlation can be modified as:

$$h_{fb} = 0.62\left[\frac{k_v^3 h_{lv}' \rho_v g\left(\rho_l - \rho_v\right)}{\mu_v D \Delta T_w}\left(\frac{a}{g}\right)\right]^{1/4} \tag{5.3}$$

in which, a is the local acceleration.

However, experiments by Merte and Clark (1964) showed that the heat flux and the Nusselt number were proportional to $\left(a/g\right)^{1/3}$ in the examined gravity range of $0.01 < a/g < 1$; on the other hand, the maximum and minimum heat flux were found to depend on gravity according to $\left(a/g\right)^{1/4}$. Unlike most the other microgravity pool boiling researches, which were performed under steady or quasi-steady conditions with constant wall heat flux or constant wall temperature, the experiments by Merte and Clark (1964) were highly transient. In their experiments, a small ball was quenched inside the saturated liquid nitrogen under different g-level, the temperature of the ball keeps decreasing, to this extent, their experimental condition is close to cryogenic chilldown process. The drop tower used in their experiments can provide a free fall time of about 1.4 second.

For flow boiling experiments, the flow will play a role in both bulk convection and vapor removal mechanism; therefore the heat transfer coefficient will not have a simple relation with local acceleration as that in pool boiling.

Chilldown investigations in reduced gravity is very limited, all of the previous experiments in open literature have been reviewed in Chapter 2. The basic findings for flow film boiling are summarized in Table 5-1.

Table 5-1. Basic findings of flow film boiling in previous chilldown experiments.

	Adham-Khodaparast et al. (1995)	Westbye et al. (1995)	Antar and Collins (1997)
Experimental apparatus	horizontal surface	horizontal tube	vertical tube
Working fluid	R113	R113	LN_2
Flow pattern	NA	inverted annular flow	liquid filament annular flow
Heat transfer rate under microgravity	lower	lower	lower
Rewetting temperature under microgravity	lower	lower	lower
Rewetting speed under microgravity	NA	higher	lower

All previous researches reported lower heat transfer rate in reduced gravity, Adham-Khodaparast et al. (1995) attributed this reduction to the thickening of the vapor film.

5.1.2 Current Experimental Condition

Since the microgravity duration is relatively short, the experiment is designed to drop the apparatus at different wall temperatures with different mass fluxes. The wall temperature is classified as three groups that are high wall temperature (about 270K), medium wall temperature (about 240K) and low wall temperature (about 210K). Different motors are used to generate different mass fluxes.

The gravity level and the deceleration impact have been measured by an accelerometer (Omega ACC104A) mounted on an aluminum piece that attached to the drag shield. The accelerometer has a calibration coefficient of 10mV/g and needs an excitation current range of 2-20mA. A current source (Omega ACC-PS1) powered by 9V batteries is used to provide the constant excitation current of 2mA. The signal is send out from the current source through BNC coaxial connector to a screw terminal (Measurement Computing SCB-50). A data acquisition board (Measurement Computing PCI-DAS 6036) plugged into the PCI slot is used for data acquisition and is connected to the screw terminal.

The method of measuring gravity level and the deceleration level follows Snyder's experiments (Snyder 1993). By taking certain time of data at each drop before the release, an average voltage level at 1-g is obtained. Using this information, combined with the calibration constant of the accelerometer, the following equation gives the g-level:

$$a = 1 + \frac{\left(V_{read} - V_{1g}\right)}{C} \tag{5.4}$$

where V_{read} is the voltage read from the accelerometer, V_{1g} is the averaged voltage at 1-g, and C is the calibration constant of the accelerometer. The 1 is added to account for the fact that the reference acceleration level is 1g.

The drag shield is dropped without loading the experimental apparatus. The deceleration level is averaged about 7g with a maximum of about 18g. The current accelerometer is designed for high g-level measurement and the output uncertainty is larger than the microgravity level. As an accelerometer capable of measuring 10^{-5}g and can still survive high deceleration is not available, the performance of the low-gravity level is not measured directly.

5.2 Flow Regime Visualization under Microgravity Condition

The flow regimes before and during drop are compared in Figure 5-1. The images on the left are taken before drop, while the microgravity images are on the right. In the experimental wall temperature range, the two-phase flow is in the DFFB state and the liquid phase is either in the form of small droplets or connected as long filaments before drop. The characteristics of the 1-g flow regime are summarized in Chapter 4.

Different flow behaviors have been recorded during the microgravity period. If the liquid phase before drop is dispersed droplets, these droplets will enter the central region still as droplets during the drop period (Figure 5-1B). For long liquid filaments, sometimes the filaments are lifted up and still maintain original shape during the drop (Figure 5-1D); in some other cases, the liquid filaments are broken and dispersed into the central region (Figure 5-1F) or has a liquid-vapor core in the center and smaller chunks at both top and bottom (Figure 5-1H).

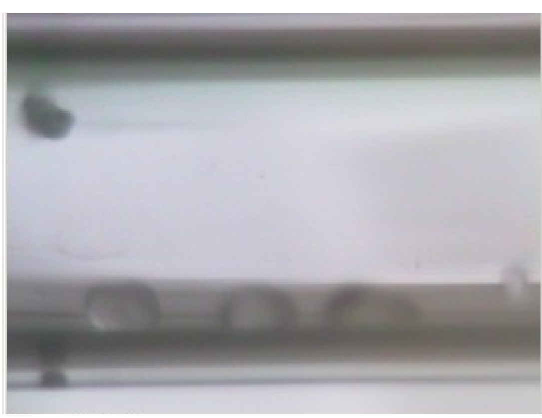
A

B

Figure 5-1. Two-phase flow images under both 1-g and microgravity conditions. A) 1-g case 1. B) Microgravity case 1. C) 1-g case 2. D) Microgravity case 2. E) 1-g case 3. F) Microgravity case 3. G) 1-g case 4. H) Microgravity case 4.

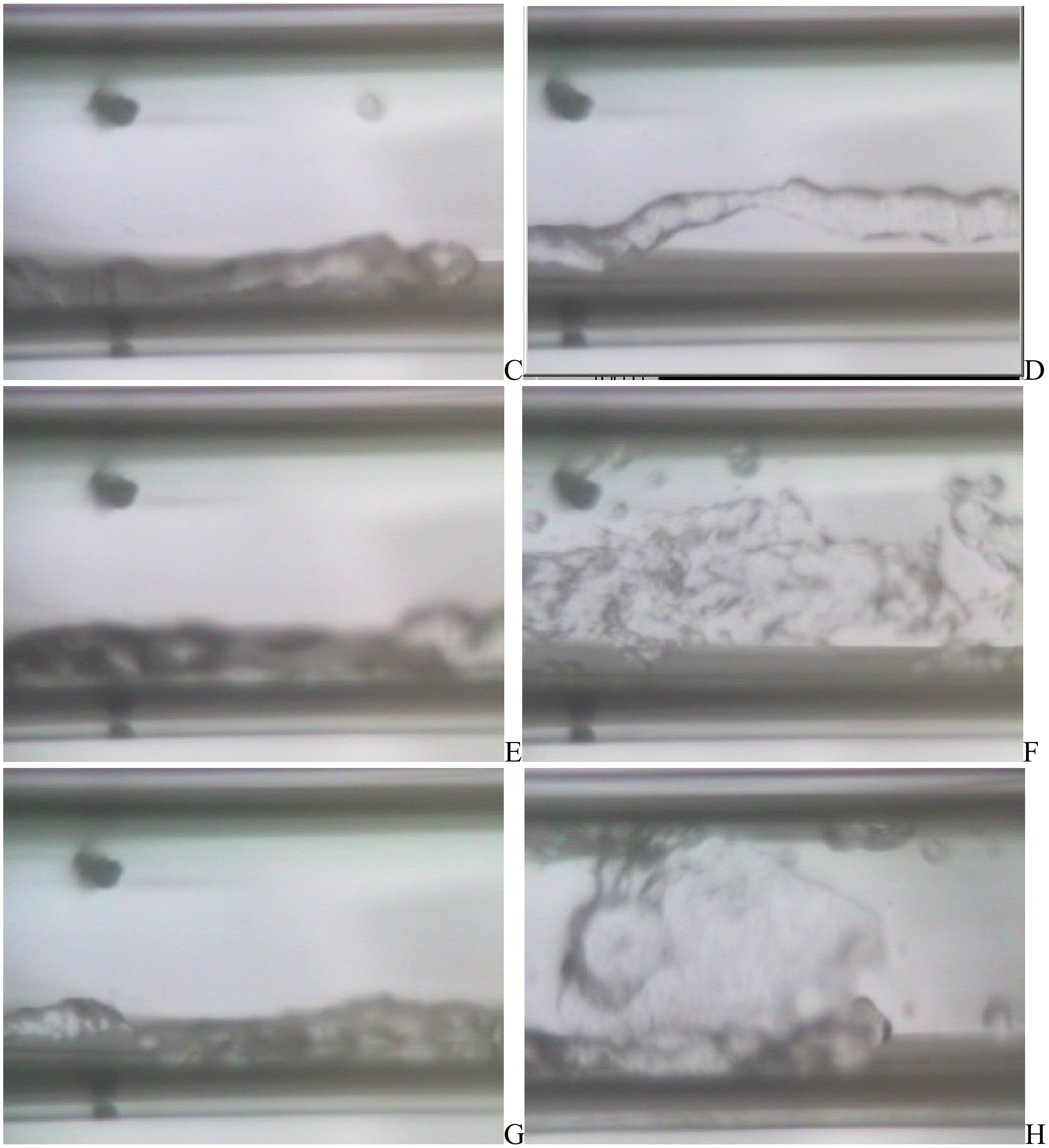

Figure 5-1. Continued.

5.3 Heat Transfer Study

Due to the thickening of the vapor film, the heat transfer in film boiling is generally lower under microgravity condition. However, this effect is expected to be relatively less important with increasing inertial term. In this section, the heat transfer in film boiling region under microgravity is to be discussed.

5.3.1 Wall Temperature Profiles

To get more data points during the microgravity period, the wall temperatures are measured only at one cross-section. Figure 5-2 gives the typical temperature profiles with different mass fluxes.

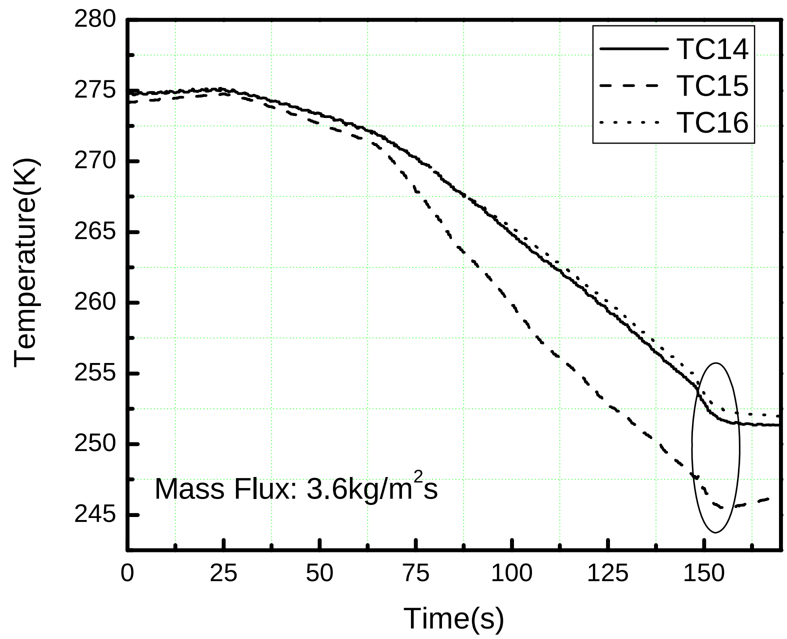

A

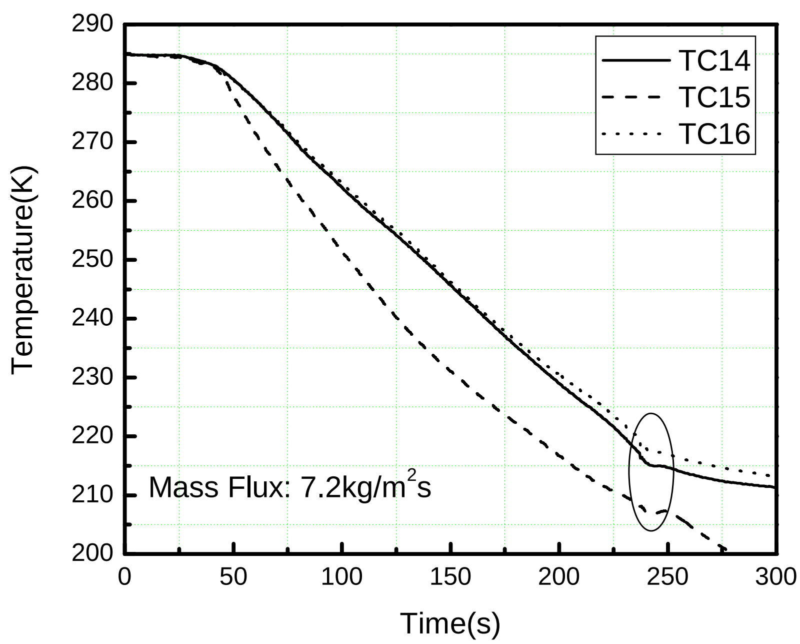

B

Figure 5-2. Temperature profiles with different mass fluxes in microgravity test. A) Mass flux of 3.6 kg/m^2s. B) Mass flux of 7.2 kg/m^2s. C) Mass flux of 10.8 kg/m^2s.

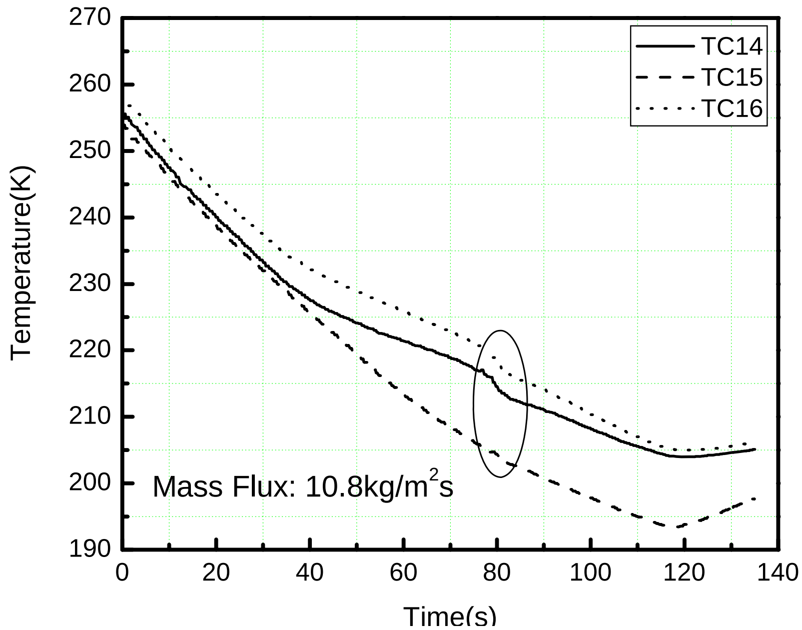

C

Figure 5-2. Continued.

The circled temperatures in Figure 5-2 approximately indicate the time period of one drop, which includes release of the drag shield, microgravity time, impact on the air bag, and deceleration period.

To exam the detail of the wall temperature response to sudden removal of the gravity force, the temperature profiles are zoomed in. Figure 5-3 illustrates the typical results. It is observed that the temperature decreasing rate at the bottom wall is generally slower during the microgravity period, because the removal of the gravitational force will thicken the vapor film and reduce the film boiling heat flux. Since the top wall transfers heat mainly by convection, the gravity field is expected to have less effect on the heat transfer at the top wall. However, as shown in Figure 5-1, it is possible for the liquid phase to contact the top wall during the microgravity period and results in higher heat removal rate. For current transient experimental condition, the best way to represent the data is to calculate the averaged heat flux which is to be given in the following section.

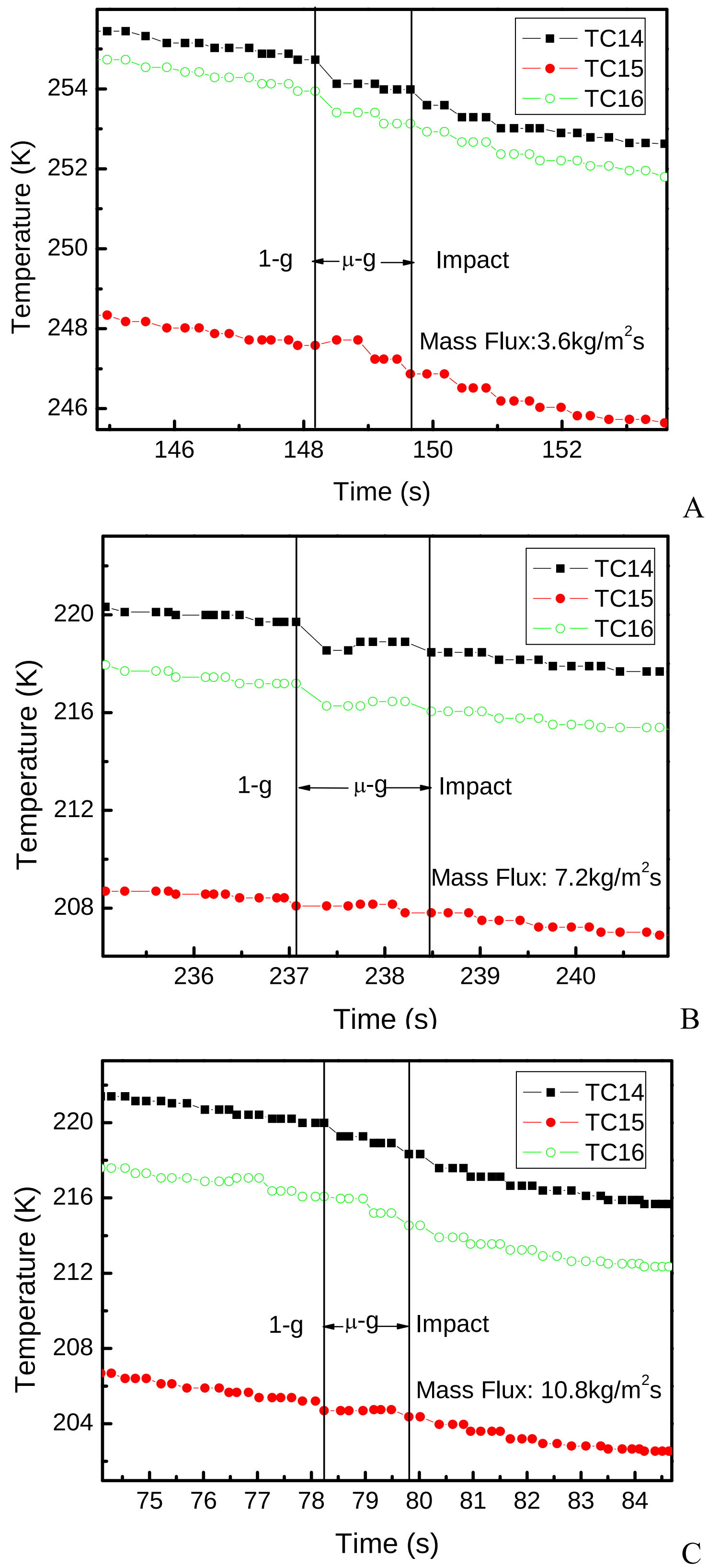

Figure 5-3. Wall temperature response to microgravity. A) Mass flux of 3.6 kg/m^{2}s. B) Mass flux of 7.2 kg/m^{2}s. C) Mass flux of 10.8 kg/m^{2}s.

5.3.2 Wall Heat Flux

The gravity effect is shown in Figure 5-4, in which the ratio of bottom heat flux before drop and during drop is plotted for different flow rates. The heat flux at the bottom of the tube decreases under microgravity condition and the ratio varies from a minimum of about 0.66 to about 0.90. The result does not show a strong dependence on wall temperature and inlet flow rate. Two runs of the quenching test performed by Xu (1998) reported similar ratio of 0.7 and 0.8, however, in Westbye et al.'s (1995) work, this ratio was found to be much less and ranged from 0.15 to 0.6.

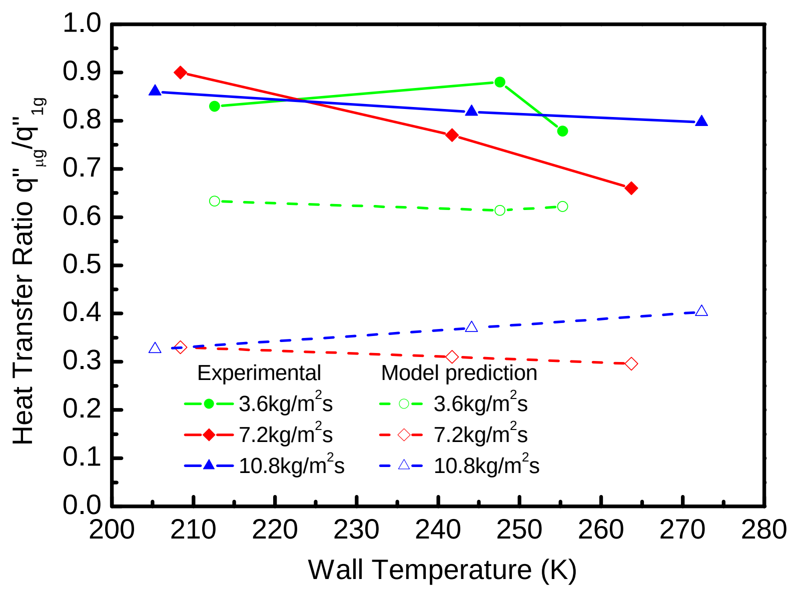

Figure 5-4. Ratio of heat flux under microgravity to 1-g condition with different flow rates and comparison with model prediction.

The bottom wall is subjected to film boiling of the liquid filaments and the convection to the super heated vapor phase. For the film boiling part, the heat flux and the heat transfer coefficient are proportional to $(a/g)^{1/3}$ as suggested by Merte and Clark (1964). Assuming that the convection is not affected by the microgravity condition, the resulted heat flux ratio is shown in the dash line in Figure 5-4; the gravity level in this calculation is 10^{-4}g. The calculation results are much scattered and significantly less than the experimental values. This suggests that under microgravity condition, the effect of convection part may raise the heat flux, and therefore the total effect of the microgravity is less prominent than that in the pool boiling experiments.

CHAPTER 6
MODELING CRYOGENIC CHILLDOWN

Numerical modeling is a powerful tool to help reveal the physics behind the experimental phenomenon, and to make prediction when systematic experiments are not attainable. For many complicated phenomena such as the chilldown process, on which the experimental investigations are relatively limited, modeling has become an indispensable part to advance our understanding.

In this chapter, a so-called “two-fluid model” is developed and applied to the cryogenic chilldown process. The model focuses on predicting chilldown heat and mass transfer under the microgravity condition, for which the experiments are difficult and costly; this model is also applicable to the vertical tube chilldown process.

6.1 Introduction

6.1.1 Flow Regimes and Transition Criteria

From experimental investigations, we know that several flow regimes exist in quenching or chilldown process. Since different flow regimes are associated with different heat transfer mechanisms, therefore the first step in modeling the chilldown process should be a correct description of the flow regimes and the corresponding transition criteria. Particularly, the flow behavior after the onset of the CHF or the so-called Post-CHF flow shows many varieties and is more challenging to model. As a comparison, the flow before the CHF point is in the nucleate boiling state and can generally be well predicted by nucleate boiling correlations or a homogeneous model.

For a steady state boiling system or a constant wall heat flux experiment in a vertical tube, it is generally accepted that the sequence of the Post-CHF flow regimes mainly depends on the thermodynamic quality at the CHF location, and can be classified into two types (Chen et al. 1979; Nelson and Unal 1992; Yadigaroglu 1978; Andreani and Yadigaroglu 1996). Figure 6-1 illustrates the Post-CHF flow regimes. If the CHF occurs at low or negative (subcooled) flow qualities, the flow regime is expected to be an inverted annular flow (IAF), followed by a dispersed flow. At high qualities, the CHF occurs due to the liquid film dryout and the flow pattern is generally a dispersed flow. A boiling regime map (Collier 1981) is often used to predict the flow regimes under a constant heat flux condition.

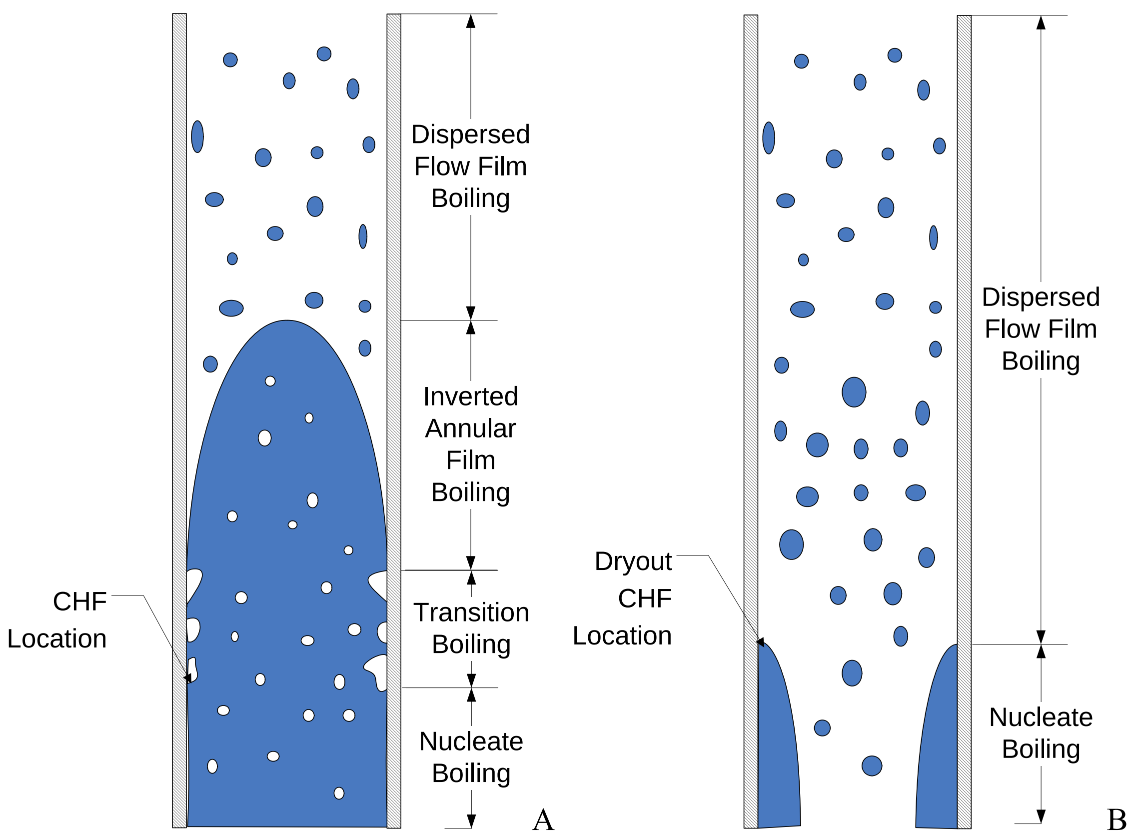

Figure 6-1. Post-CHF flow regimes. A) Low-quality CHF. B) High quality CHF.

The boiling regime map is, however, not applicable to chilldown experiments. The reason is that neither the wall heat flux nor the CHF location is fixed during chilldown. As shown in previous chapters, the CHF location moves downstream as the tube is chilled down and the wall heat transfer experiences the film boiling, transition boiling and nucleate boiling sequential stages. Moreover, the detailed structures of the flow regimes are highly dependent on the flow regime from which it originates. In a chilldown process, initially the wall temperature is often several hundred degrees above the Leidenfrost temperature. When the liquid enters the hot tube, a vapor film is formed immediately and it separates the liquid from touching the wall. In a vertical tube or under microgravity environment, the liquid phase generally flows in the middle of the tube. Therefore, for vertical tube chilldown or microgravity chilldown, the general sequence of the flow regime after the rewetting point is expected to be IAF, dispersed flow, and single phase vapor flow.

The above discussion on flow regimes describes a general classification, more detailed flow regimes have been reported from experiments. For example, the IAF was further divided into different flow regimes such as smooth IAF, rough-wavy IAF, and agitated IAF as summarized by Ishii and Dejarlais (1986, 1987).

The flow regime transition criterion is another important factor required for a successful modeling of the two-phase flow system. For Post-CHF flows, the void fraction α or quality x is usually used as the transition criterion. Obot and Ishii (1988) developed a set of flow regime transition criteria in terms of the capillary number and the downstream distance from the CHF location (Table 6-1), and their criteria were implemented into a nuclear reactor safety code. Here, Z is the downstream distance from the CHF location, D is the tube diameter, and Ca is the capillary number.

Table 6-1. Post-CHF flow regime transition criteria.

Regime	Ishii's Correlation	Void Frraction
Smooth IAF	$Z/D = 60\mathrm{Ca}^{1/2}$	$0.05 < \alpha < 0.3$
Rough-Wavy IAF	$Z/D = 295\mathrm{Ca}^{1/2}$	$0.3 < \alpha < 0.4$
Agitated IAF	$Z/D = 595\mathrm{Ca}^{1/2}$	$0.4 < \alpha < 0.75$
Dispersed IAF (post-agitated IAF)		$0.75 < \alpha < 0.98$
Highly dispersed IAF		$\alpha > 0.98$

If only IAF and dispersed flow are modeled in the Post-CHF region as shown in Figure 6-1A, then the only transition encountered is form IAF to dispersed flow. A widely accepted criterion given by Groeneveld (1975) suggests that the dispersed flow develops at the void fraction high than 0.8. However, lower values were also used. Hammouda et al. (1997) used 0.5 in their IAFB model.

The physics behind this transition is believed to be related to the instabilities that develop at the liquid-vapor interface, which consequently lead to necking and detachment of the liquid column (Kawaji and Banerjee 1987). The detached liquid column breaks up further into droplets through different mechanisms (Andreani and Yadigaroglu 1994). The transition criterion used by Kawaji and Banerjee (1988) is given as: $\alpha_{lj} < 0.5$ or

$\dfrac{\alpha_{lj-1} - \alpha_{lj}}{\Delta Z} > 0.15$ and $\alpha_{lj+1} > 0.6$. Here, α_l is the volume fraction of the liquid, and j denotes the node point. Analytis and Yadigaroglu (1987) proposed to use the Weber number as the criterion, the Weber number in their study is defined as:

$$\mathrm{We} = \rho_v \left(u_v - u_l\right)^2 2\left(R - \delta\right) / \sigma \tag{6.1}$$

where ρ_v is vapor density; u_v and u_l are vapor and liquid phase velocity, respectively; R is tube radius; δ is vapor film thickness; σ is the surface tension.

Upstream of the CHF point, the two-phase flow is in the transition or nucleate boiling state. The rewetting temperature is often used as the transition criterion to discern Pre-CHF and Post-CHF region. The rewetting temperature is affected by flow rate, wall surface condition, axial temperature gradient and many other factors, and therefore is usually extracted from the experimental results.

6.1.2 Different Modeling Methods and Current Approach

Different methods have been used in two-phase flow modeling, ranging from the homogenous model (Cross et al. 2002) to the two-fluid model (Ishii 1975; Ardron 1980; Ishii and Mishima 1984), then to the three fluid model (Alipchenkov et al. 2004), in which the entrained phase is described by an additional set of conservation equations, and further to more detailed models that incorporate both micro- and macro-scale models (Ben David et al. 2001 a, b). A review of different levels in chilldown models is given in Chapter 2.

During a chilldown process, the velocity difference between the two phases are considerably large, moreover, downstream of the rewetting point, the flow is essentially in thermodynamic non-equilibrium. In the two-fluid model, each phase is described with a set of conservation equations; therefore this model is more applicable to discern the differences between phases, and is adopted in the current investigation. The general conservation equations are given in Equations 2.1-2.4.

In this study, four distinct flow regions, namely, fully vapor region, DFFB region, IAFB region, and nucleate boiling region, are modeled. The two-fluid model is used to describe the DFFB and IAFB region, while fully vapor region and nucleate boiling region are treated as single phases.

6.2 Inverted Annular Film Boiling Model

In chilldown experiments, IAFB is expected to immediately follow the QF and then change to DFFB downstream at a high void fraction. A two-fluid IAFB model is to be discussed in this section; the model will be implanted into cryogenic chilldown model later.

6.2.1 Introduction

IAFB is characterized by high surface temperatures and consists of a continuous liquid core at the center of the channel, surrounded by a vapor blanket covering the heated surface. The study of the IAFB is of considerable practical interest in many applications, such as cryogenic system, nuclear reactor safety, steam generators, evaporators, and metallurgical processing (Hammouda et al. 1997).

The two-phase flow and heat transfer phenomena in IAFB are rather complicated. For example, in IAFB, for highly subcooled liquid and high flooding rates, momentary local transition to nucleate boiling near the QF is also thought to be possible (Edelman et al. 1983). Incorporation of such detailed effects in a mechanistic IAFB model would be an almost impossible task (Analytis and Yadigaroglu 1987). Therefore, the two-fluid model has been used as a balance between simplicity and inclusion of important phenomena.

The conservation equations of all the two-fluid IAFB models come from the fundamental work of Ishii and other researchers (Ishii 1975; Ardron 1980; Ishii and Mishima 1984). The steady state form of two-fluid IAFB model was suggested by Analytis and Yadigaroglu (1987) and by Hammouda et al. (1997), while the transient form was developed by Kawaji and Banerjee (1987, 1988). Having almost the same conservation equations, these models differ from one another in how the constitutive relations are formed.

6.2.2 Model Description

6.2.2.1 Assumptions and conservation equations

Conservation equations for the IAFB model are derived based on the assumptions listed below:

1. Liquid flows in the center of the flow channel and is separated from the heated wall by a vapor layer.
2. The vapor layer thickness is uniform around the tube periphery.
3. The vapor layer contains no entrained liquid.
4. The liquid core contains no vapor bubbles.
5. The pressure is uniform in the radial direction.
6. The two phases are in thermodynamic non-equilibrium, and the vapor phase is treated as an ideal gas.
7. The interface is smooth and the interfacial velocity u_i is equal to the liquid phase velocity u_l.
8. The interface is saturated.
9. The vapor flow changes from laminar to turbulent at a vapor Reynolds number, Re_v, large than 100.

The above turbulent transition criterion was suggested by Hsu and Westwater (1959). Later, Kao et al. (1972) argued that there was transition to turbulence in the vapor film almost immediately downstream from the origin of the film boiling region. However, current study shows that the vapor Reynolds number increases very fast in the film boiling region, therefore, use either of the above transition criteria will have an insignificant difference. In this study the first transition criterion is used.

For a vertical tube, the transient one-dimensional two-fluid equations for the IAFB region are given as below:

Continuity equations:

$$\frac{\partial}{\partial t}(\alpha\rho)_l + \frac{\partial}{\partial z}(\alpha\rho u)_l = -m_l''\frac{P_i}{A} \tag{6.2}$$

$$\frac{\partial}{\partial t}(\alpha\rho)_v + \frac{\partial}{\partial z}(\alpha\rho u)_v = m_l''\frac{P_i}{A} \tag{6.3}$$

Momentum equations:

$$\frac{\partial}{\partial t}(\alpha\rho u)_l + \frac{\partial}{\partial z}(\alpha\rho uu)_l + \alpha_l\frac{dP}{dz} = \pm\alpha_l\rho_l g + \frac{\tau_i P_i}{A} + m_l''\frac{(u_l - u_i)P_i}{A} \tag{6.4}$$

$$\frac{\partial}{\partial t}(\alpha\rho u)_v + \frac{\partial}{\partial z}(\alpha\rho uu)_v + \alpha\frac{dP}{dz} = \pm\alpha\rho_v g - \frac{\tau_i P_i}{A} - m_l''\frac{(u_v - u_i)P_i}{A} - \frac{\tau_{wv}P_w}{A} \tag{6.5}$$

Enthalpy energy equations:

$$\frac{\partial}{\partial t}(\alpha\rho h)_l + \frac{\partial}{\partial z}(\alpha\rho uh)_l = \frac{q_{lh}''P_i}{A} - m_l''\frac{(h_{ls} - h_l)P_i}{A} \tag{6.6}$$

$$\frac{\partial}{\partial t}(\alpha\rho h)_v + \frac{\partial}{\partial z}(\alpha\rho uh)_v = \frac{q_v''P_i}{A} + m_l''\frac{(h_{vs} - h_v)P_i}{A} \tag{6.7}$$

State equation of the vapor phase:

$$\rho_v = \frac{P}{R_g T_v} \tag{6.8}$$

In the above equations, subscript *l* is for liquid phase, *v* is for vapor phase, *w* is for wall, *s* is for saturation, and *i* denotes the liquid-vapor interface; α is void fraction, while $\alpha_l = 1-\alpha$ is the liquid volume fraction; m_l'' denotes the vaporization mass flux at the interface; q_{lh}'' and q_v'' are the heat fluxes used to heat up the liquid and vapor, respectively;

P_i and P_w are interfacial and wall perimeter, respectively; A is the cross section area of the flow channel; τ is the shear stress; g is the gravitational acceleration constant and R_g is the gas constant. For the body force in the momentum equations, plus sign is for downward flow, and minus sign is for upward flow.

The above equations are derived for subcooled flow film boiling case, which is more general. The liquid heating term, q''_{lh}, is used to account for the heat distributed to heat up the subcooled liquid. For saturated flow boiling, $q''_{lh} = 0$, and the entire liquid core is at saturation temperature, therefore the enthalpy of the liquid phase is only depends on the local pressure, which is not unknown after solving the momentum equation, thus Equation 6.6 need not to be solved.

As stated in assumption 6, the interfacial velocity is equal to the liquid phase velocity; therefore the third term in the RHS of Equation 6.4 will disappear. The momentum equations for saturated IAFB are written as:

$$\frac{\partial}{\partial t}(\alpha\rho u)_l + \frac{\partial}{\partial z}(\alpha\rho uu)_l + \alpha_l\frac{dP}{dz} = \pm\alpha_l\rho_l g + \frac{\tau_i P_i}{A} \tag{6.9}$$

$$\frac{\partial}{\partial t}(\alpha\rho u)_v + \frac{\partial}{\partial z}(\alpha\rho uu)_v + \alpha\frac{dP}{dz} = \pm\alpha\rho_v g - \frac{\tau_i P_i}{A} - m''_l\frac{(u_v - u_l)P_i}{A} - \frac{\tau_{wv}P_w}{A} \tag{6.10}$$

6.2.2.2 Heat transfer in inverted annular film boiling

Proper selection of the constitutive relations to close the above equations requires clear understanding of the physical mechanisms in IAFB region. Therefore, before given the constitutive relations, the heat transfer mechanism is to be discussed here.

A typical flow section in IAFB is sketched in Figure 6-2. The liquid core is separated from the hot wall with a vapor film of thickness δ in a hot tube with radius of *R*. From previous assumption, it is readily to get:

$$\delta = R\left(1-\sqrt{\alpha_l}\right) \tag{6.11}$$

The interfacial perimeter and inside wall perimeter are then given as:

$$P_i = 2\pi\left(R-\delta\right) \tag{6.12}$$

$$P_w = 2\pi R \tag{6.13}$$

The heat transfer in IAFB is proposed as a three-step process: heat transfer from wall to vapor, q''_{wv}; from vapor to liquid, q''_{vl}; and from the interface to liquid core, q''_{lh}, which is used to heat the subcooled liquid and vanishes for saturated boiling. Radiation heat transfer from wall to the liquid, q''_r, is also considered.

From energy balance, the total heat flux received by the liquid column is:

$$q''_l = q''_{vl} + q''_r \tag{6.14}$$

while the energy balance for the vapor phase gives:

$$P_i q''_v = q''_{wv} P_w - q''_{vl} P_i \tag{6.15}$$

The interfacial and wall perimeter appear in the above equation due to the difference in heat transfer area. The total heat flux to the liquid phase is used to evaporate the liquid at interface as well as heat up the liquid core (for subcooled flow boiling only). Therefore:

$$q''_{ev} = q''_l - q''_{lh} = q''_{vl} + q''_r - q''_{lh} \tag{6.16}$$

For saturated flow boiling, the independent variables in the above analysis are q''_{wv}, q''_{vl}, and q''_r. The vapor phase flows between the annulus of the wall and the liquid core.

Kays (1993) tabulated the Nusselt number for annulus flow. However, the Nusselt number depends on the ratio of the inner and outer radius, which is changing in IAFB region, as shown in Figure 6-2. Therefore, the vapor flow is treated as flow between two parallel plates for $\delta << R$, while Colburn equation (Incropera and Dewitt 2002) is used for $\delta \sim R$.

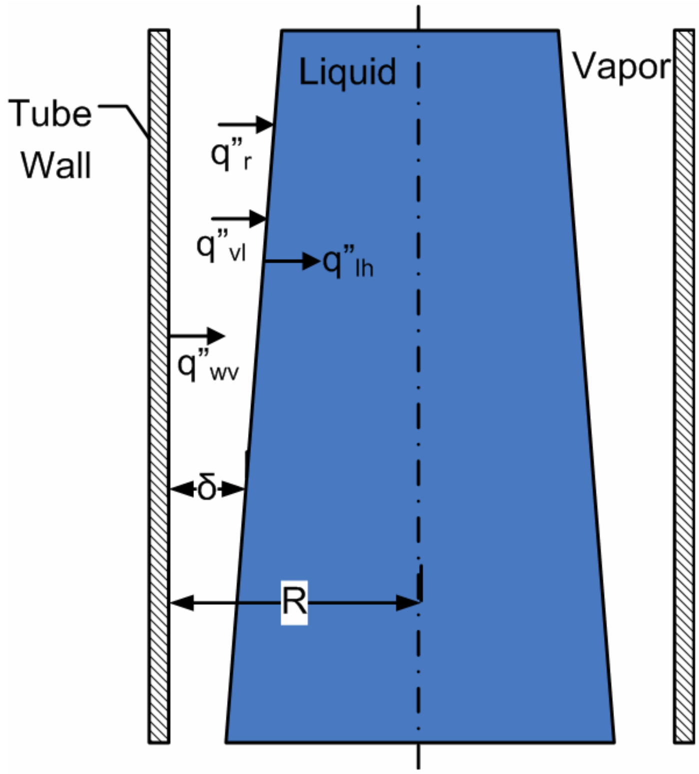

Figure 6-2. Heat transfer mechanisms in IAFB.

Considering the vapor flow as flow between two parallel plates and liquid at saturation temperature, the wall to vapor and vapor to liquid heat fluxes can be given as (Kays 1993):

$$q''_{wv} = \frac{k_v \mathrm{Nu}_\mathrm{w}}{2\delta\left(1\text{-}\theta^{*2}\right)}\left[\left(T_w - T_v\right) - \theta^*\left(T_v - T_s\right)\right] \tag{6.17}$$

$$q''_{vl} = \frac{k_v \mathrm{Nu}_\mathrm{i}}{2\delta\left(1\text{-}\theta^{*2}\right)}\left[\left(T_v - T_s\right) - \theta^*\left(T_w - T_v\right)\right] \tag{6.18}$$

where θ^* is the influence coefficient. Kays (1993) gave that for laminar flow Nu=5.385 and $\theta^* = 0.346$; for turbulent flow with $\mathrm{Re} = 10000$, Nu=27.8 and $\theta^* = 0.220$ (for $\mathrm{Pr} = 0.7$). The Nuseelt number Nu and θ^* can be interpolate between the laminar values and turbulent values for $\delta << R$.

For $\delta \sim R$, the Colburn equation (Incropera and Dewitt 2002) gives:

$$q''_{wv} = 0.023\frac{k_v}{2\delta}\mathrm{Re}_w^{\ 0.8}\,\mathrm{Pr}_v^{\ 0.33}\left(T_w - T_v\right) \tag{6.19}$$

$$q''_{vl} = 0.023\frac{k_v}{2\delta}\mathrm{Re}_i^{\ 0.8}\,\mathrm{Pr}_v^{\ 0.33}\left(T_v - T_l\right) \tag{6.20}$$

while the Reynolds number is defined as:

$$\mathrm{Re}_w = \rho_v u_v 2\delta/\mu_v \tag{6.21}$$

$$\mathrm{Re}_i = \rho_v \left|u_v - u_l\right| 2\delta/\mu_v \tag{6.22}$$

in which, μ_v is the vapor viscosity.

Assume that the vapor film is transparent and the wall is gray, the radiation heat flux to the liquid core is written as (Hammouda et al. 1997):

$$q''_r = \frac{\sigma_B\left(T_w^4 - T_s^4\right)}{\dfrac{1}{\varepsilon_w} - \dfrac{1}{\varepsilon_l\sqrt{\alpha_l}} - 1} \tag{6.23}$$

where $\sigma_B = 5.67\times10^{-8}\ \mathrm{W/m^2\,K^4}$ is the Stefan-Boltzman constant; ε_w and ε_l are emissivity of the wall and the liquid, respectively.

6.2.2.3 Constitutive relations

For saturated flow boiling, constitutive relations for m''_l , q''_v , τ_i , τ_{wv} should be specified to close the model equations. Different constitutive relations, which are generally come from single-phase or adiabatic annular two-phase flow experiments, have been proposed in the literature. In present approach, attention has been paid to provide the constitutive relations in the same form at similar boundary conditions. For example, the wall shear stress and interfacial shear stress are given in the same form. The constitutive relations will be summarized below.

Vapor generation term. In the model equations, the vapor generation term, m_l'', has the unit of $[\mathrm{kg/m^2s}]$. It denotes the vapor generation rate per unit area at the interface. Given the latent heat for phase change, h_{lv}, the vapor generation term is expressed as:

$$m_l'' = q_{ev}''/h_{lv} \tag{6.24}$$

where the evaporation heat flux q_{ev}'' is given in Equation 6.16.

Vapor heating term. As described previously, vapor heating term can be calculated from Equation 6.15.

Shear stress terms. For turbulent flow in the vapor film, correlations for wall shear stress and interfacial shear stress are given by (Kawaji and Banerjee 1988):

$$\tau_{wv} = 0.5\, f_w \rho_v u_v^2 \tag{6.25}$$

$$\tau_i = 0.5\, f_i \rho_v \left(u_v - u_l\right)^2 \tag{6.26}$$

where f_w and f_i are friction factor, and given by:

$$f_w = 0.085\,\mathrm{Re}_w^{-0.25} \tag{6.27}$$

$$f_i = 0.085\,\mathrm{Re}_i^{-0.25} \tag{6.28}$$

in which Re_w and Re_i are defined in Equation 6.21 and Equation 6.22, respectively.

6.2.3 Boundary Condition and Solution Procedure

For the transient form of the IAFB model, a semi-implicit, finite-difference scheme is adopted, and a Second Order Upwind (SOU) scheme is used for convection term.

IAFB model can also be applied to steady state problem as in a vertical channel heated with constant heat flux, and the inside two-phase flow is in steady film boiling state with low to moderate void fraction. This is a common process in many industrial systems. On the other hand, the solving procedure and results of the steady IAFB model are beneficial to adopt its transient form in chilldown model as well as assess the validity of the model. In this section, the boundary condition and solution procedure for the steady IAFB model will be given.

6.2.3.1 Boundary condition

The steady IAFB model is applied to a stainless steel vertical tube heated with constant heat flux q''_w. The tube has 0.635cm OD, 0.432cm ID, and 70 cm length. Small initial void fraction and slip velocity are assigned at the inlet (Xu et al. 2006). An initial void fraction ε_1 of 0.01 and a slip velocity ε_2 at the order of 10^{-3} are used in the computation. The two-phase nitrogen flow is injected from top or bottom of the tube with a volume flow rate of $\dot{V}$. The pressure at the inlet is given and both phases are in saturated temperature T_s at the inlet. The boundary conditions of the two-phase flow at the tube inlet are summarized as:

$$\left.\begin{aligned} &\alpha_0 = \varepsilon_1 \\ &P_0 = P_{in} \ \left(P_{in} \text{ specified}\right) \\ &u_{l,0} = \dot{V}\big/A \ \left(\dot{V} \text{ specified}\right) \\ &u_{v,0} = u_{l,0} + \varepsilon_2 \\ &h_{v,0} = h_{vs} \end{aligned}\right\} \tag{6.29}$$

For the tube wall temperature calculation, adiabatic boundary condition is set at the inlet and outlet of the tube wall; the outer surface of the tube is subjected to constant heat flux, while the inner surface loses heat to the two-phase flow.

6.2.3.2 Numerical method and solution procedure

Different numerical methods have been used to solve the two-fluid governing equations in the literature. SIMPLE method was used by Issa and Kempf (2003) and by Liao (2005), while Runge-Kutta (Hammouda et al. 1997) and Euler method (Yang and Zhang 2005; Xu et al. 2006), which are much easier, were also often used. In current study the Euler method is used.

For saturated flow boiling, the dependent variables are α, P, u_l, u_v, h_v. The continuity and momentum equations can be expressed as:

$$\begin{bmatrix} \alpha & 2\alpha\rho_v u_v & 0 & \rho_v u_v^2 \\ (1-\alpha) & 0 & 2(1-\alpha)\rho_l u_l & -\rho_l u_l^2 \\ 0 & \alpha\rho_v & 0 & \rho_v u_v \\ 0 & 0 & (1-\alpha)\rho_l & -\rho_l u_l \end{bmatrix} \begin{bmatrix} \partial P/\partial z \\ \partial u_v/\partial z \\ \partial u_l/\partial z \\ \partial \alpha/\partial z \end{bmatrix} = \begin{bmatrix} B_1 \\ B_2 \\ B_3 \\ B_4 \end{bmatrix} \tag{6.30}$$

Here,

$$\left.\begin{aligned} B_1 &= -\frac{\tau_i P_i}{A} - \frac{m_l''(u_v - u_l)P_i}{A} - \frac{\tau_{wv} P_w}{A} - \alpha u_v^2 \frac{\partial \rho_v}{\partial z} \pm \alpha\rho_v g \\ B_2 &= \frac{\tau_i P_i}{A} \pm (1-\alpha)\rho_l g \\ B_3 &= \frac{m_l'' P_i}{A} - \alpha u_v \frac{\partial \rho_v}{\partial z} \\ B_4 &= -\frac{m_l'' P_i}{A} \end{aligned}\right\} \tag{6.31}$$

Introduce the vapor momentum equation into vapor enthalpy equation, one can get:

$$\frac{\partial h_v}{\partial z} = \frac{q_v'' P_i / A + m_l''(h_{vs} - h_v) P_i / A - m_l'' h_v}{\alpha \rho_v u_v} \tag{6.32}$$

To obtain the wall temperature, the 1-D heat conduction equation is used, and gives:

$$\frac{\partial^2 T_w}{\partial z^2} + \frac{q_w'' - q_{wv}'' - q_r''}{k_w \delta_w} = 0 \tag{6.33}$$

where, k_w is the thermal conductivity of the wall and δ_w is the wall thickness. The discretized equation is solved by Tri-diagonal Matrix Algorithm (TDMA) method. The solution procedure is illustrated in Figure 6-3.

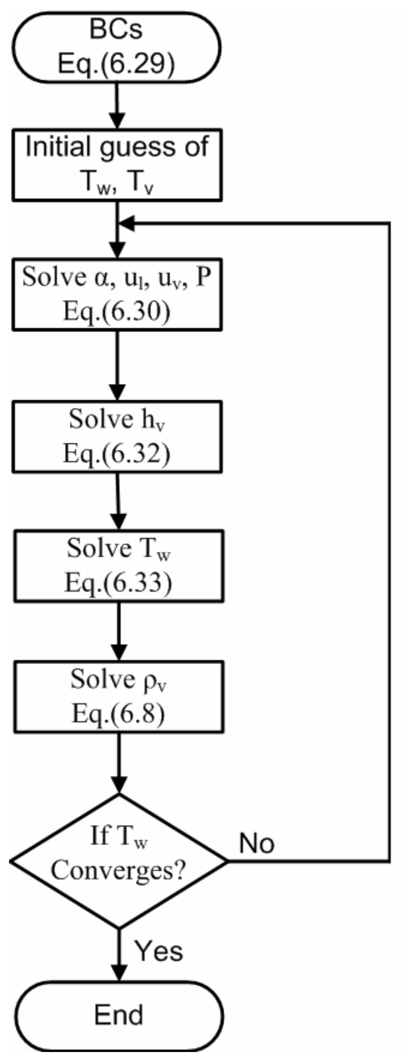

Figure 6-3. Solution procedure of steady IAFB two-fluid model.

After setting the boundary conditions at the inlet, initial guesses of the vapor temperature and wall temperature are given. The computation first solves the continuity and momentum equations and then the vapor enthalpy equation. After that the wall temperature is updated based on the heat conduction equation. Next, the vapor temperature is updated from state equation. This process is iterated until the wall temperature converges.

6.2.4 Results and Discussion

To validate the IAFB model, it would be desirable to compare the modeling results with experimental measurements. However, to our knowledge, the available experimental data are either for transient process (Kawaji et al. 1985; Lee and Kim 1987) or for subcooled flow boiling (Takenaka et al. 1989). As a compromise, part of the model results is compared with a correlation.

For IAFB, the only correlation we can find in the literature is given by Carey (1992), in which the heat transfer coefficient is given as:

$$h = \left[\frac{\rho_v \left(\rho_l - \rho_v \right) g h'_{lv} k_v^3}{4\left(z - z_{CHF} \right) \mu_v \left(T_w - T_s \right)} \right]^{1/4} \tag{6.34}$$

where, z_{CHF} is the CHF location, and $z - z_{CHF}$ denotes the distance from the CHF location. h'_{lv} is defined by:

$$h'_{lv} = h_{lv} + \frac{3}{8} C_{pv} \left(T_w - T_s \right) \tag{6.35}$$

The wall heat flux is calculated by:

$$q''_w = h\left(T_w - T_s \right) \tag{6.36}$$

Apparently, Equation 6.34 comes from the Bromley type correlation (Bromley 1950) for stable pool boiling, and therefore only applicable for two-phase system with very small interfacial shear stress (Carey 1992). The effects of flow direction and flow rate are not correlated in Equation 6.34.

Figure 6-4 compares the wall temperatures computed by the IAFB model and by Equation 6.34 under three different wall heat fluxes of $3.5\,\mathrm{kW/m^2}$, $5.0\,\mathrm{kW/m^2}$, and $10.0\,\mathrm{kW/m^2}$. The CHF location in Equation 6.34 is evaluated from the inlet void fraction α_0 through:

$$z_{CHF} = -\frac{\rho_v h_{lv} \alpha_0 \cdot \rho_l \dot{V} \big/ \left[\rho_l \left(1-\alpha_0\right) + \rho_v \alpha_0 \right]}{q''_w \pi D} \tag{6.37}$$

where D is the ID of the tube. The IAFB model is carried out for down-flow case.

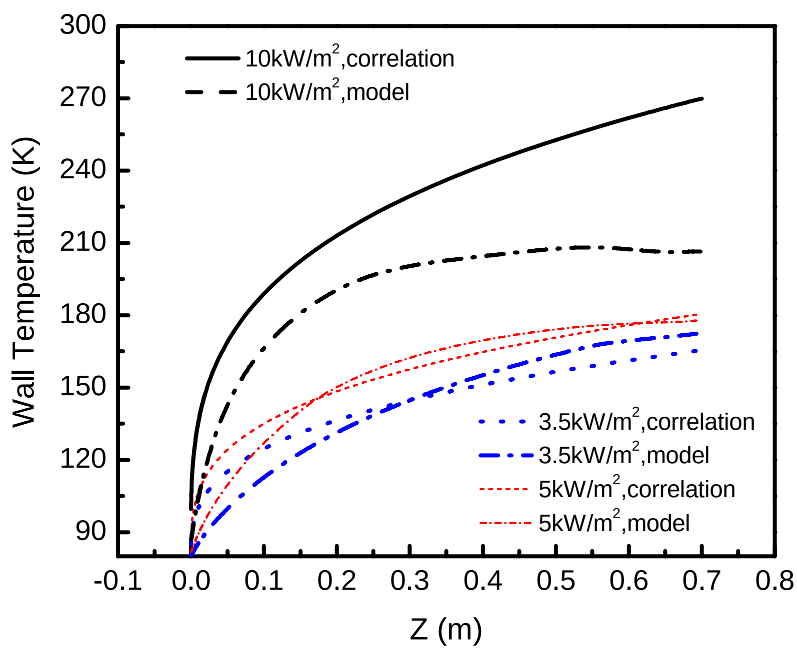

Figure 6-4. Comparison of wall temperatures between the IAFB model and the correlation prediction under different heat fluxes.

With increasing wall heat flux, more liquid nitrogen is evaporated, and the slip velocity increases according to mass conservation. Therefore the interfacial shear stress is larger at higher wall heat flux. For the small and moderate wall heat flux cases, in which the interfacial shear stress is not very large, the correlation is valid as motioned before and agrees well with the IAFB model.

As more liquid phase is evaporated, the vapor velocity and slip velocity increase along the axial direction, associated with increasing heat transfer coefficient and vapor film thickness, which are two competing parameters that influence the wall-to-vapor heat transfer. Experimental results (Hammouda et al. 1996) show that the wall temperature approaches a constant value or even decreases after certain downstream location. The model result for large wall heat flux, the $10.0\,\mathrm{kW/m^2}$ case, shows this trend correctly, on the other hand, the correlation of Equation 6.34 comes from pool boiling experiments and only considers the effect of the thickening of the vapor film at downstream location, it breaks down and gives unreasonably high wall temperature, as shown in Figure 6-4. For up-flow, the slip velocity is generally higher than that of the down-flow case, and the correlation is expected to give less accurate prediction.

The IAFB model can also be used to study the gravity effect on the two-fluid system. Figure 6-5 shows the liquid velocity u_l and vapor velocity u_v along the tube for down-flow, up-flow and 0-g case with the wall heat flux of $5.0\,\mathrm{kW/m^2}$. The body force term in Equation 6.31 is zero for 0-g case, while plus and minus sign are for down-flow and up-flow case, respectively. It is obvious that the up-flow case has the largest slip velocity, while the down-flow case has the smallest slip velocity and 0-g case lies in the middle. The highest liquid phase velocity is achieved in the down-flow case, and the highest vapor velocity corresponds to the up-flow case.

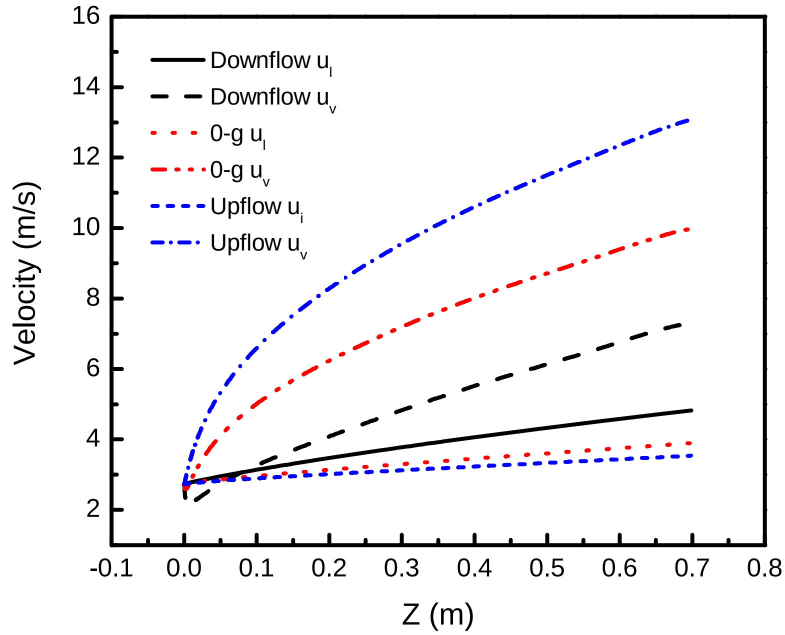

Figure 6-5. IAFB model prediction of the liquid velocity and the vapor velocity along the tube for down-flow, up-flow, and 0-g.

Generally, all the velocities increase along the axial direction, however, it is noted that the vapor velocity for the down flow case decreases from 2.8m/s to about 2.1m/s at the tube inlet and then increases. For down flow, the liquid velocity has the maximum increase rate and the void fraction is near zero at the tube inlet, to satisfy the mass conservation equation, the vapor velocity must decrease at the tube inlet. Until at further downstream location, the void fraction is larger and the vapor phase begins to be accelerated.

The corresponding wall temperature T_w, vapor temperature T_v, and void fraction α are shown in Figure 6-6 for down-flow, up-flow and 0-g case. The down-flow has the highest wall temperature, vapor temperature, and void fraction. This is because for down-flow case the vapor velocity is the lowest (Figure 6-5). In IAFB, the heat from the wall is mainly carried away by the vapor phase, the vapor phase then distributes part of this heat to evaporate the liquid phase, and the radiation heat transfer is often negligible small. The convective heat transfer between the wall and the vapor is characterized by the vapor Reynolds number in Equation 6.19; therefore, lower vapor velocity is associated with higher wall temperature, higher vapor temperature and higher void fraction.

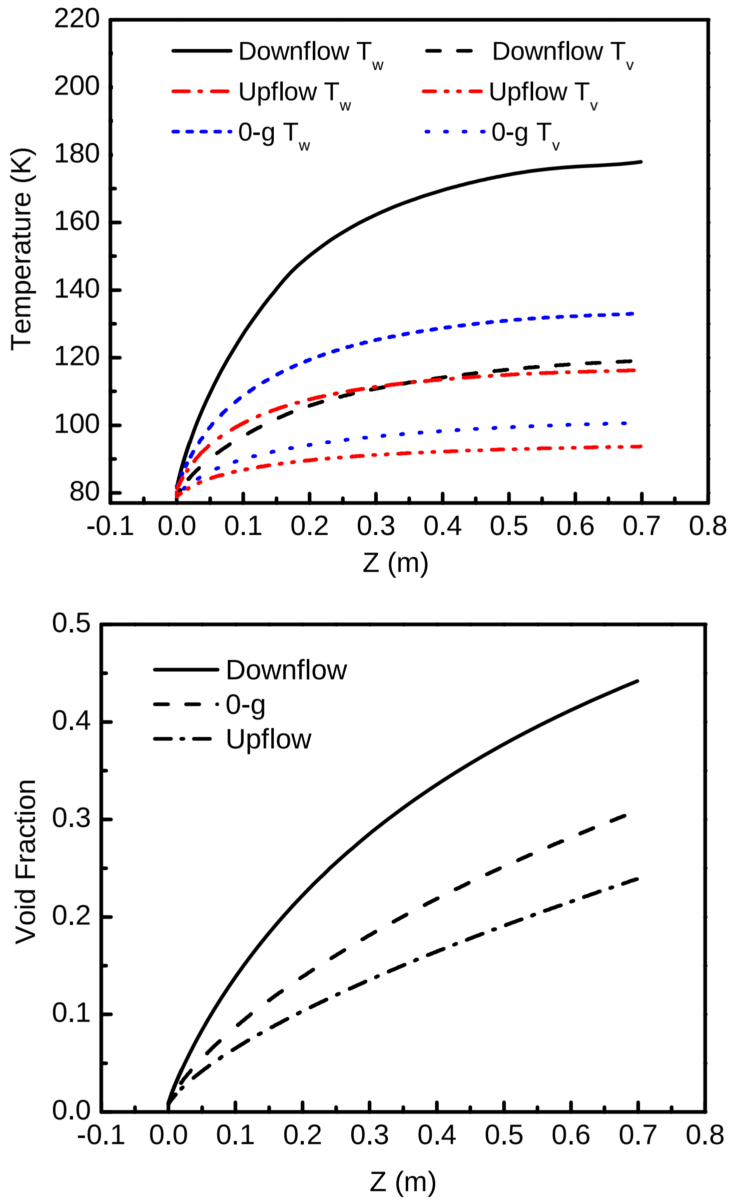

A

B

Figure 6-6. IAFB model prediction of different variables along the tube for down-flow, up-flow, and 0-g. A) Wall temperature and vapor temperature. B) Void fraction.

One can also find that the thermal equilibrium only holds for locations close to the CHF point, and the degree of thermal non-equilibrium increases along the flow direction. Therefore, it is generally inapplicable to describe the IAFB with simple empirical correlations which are usually based on saturation properties.

6.3 Dispersed Flow Film Boiling Model

In chilldown experiments and in flow channels heated with constant heat flux, with increasing void fraction and velocity deference between the two phases, dispersed flow is expected to appear downstream of the IAFB region. A two-fluid model for the dispersed flow is developed in this study and used in the cryogenic chilldown model later.

6.3.1 Introduction

Dispersed flow is also called mist or liquid deficient flow in the literature. It is characterized by liquid droplets dispersed in a continuous vapor phase. Dispersed flow is generally in a non-equilibrium state(Carey 1992).

The existence of the droplets in the flow channel will inevitably alter both the flow field and the total heat transfer coefficient. As summarized by Andreani and Yadigaroglu (1996), the dispersed phase can modify the temperature field and modify the velocity and thermal boundary layers. For example, for flow channel with uniformly distributed droplets, a large interfacial heat transfer and vaporization rate occurs in the vicinity of the wall where the vapor temperature is highest. This will result in a strong reduction of the vapor temperature in the viscous sublayer. Moreover, the structure of the turbulence is strongly affected by the dispersed phase: the presence of particles near the wall promotes turbulence in the boundary layer, increasing heat transfer, while particles in the core may dampen or increase the turbulence.

The droplets size, distribution and revolution are important in dispersed flow prediction. Wide spectrum of droplet size and different distribution functions have been reported in the literature (Ganić and Rohsenow 1977). However, detailed description of the droplets during a test is a difficult task, and not enough data have been accumulated to provide satisfactory correlation untill now. Lacking of the proper droplet size distribution, together with currently poor understanding of the interfacial exchange mechanisms, makes the DFFB models often end up with too many adjustable parameters.

Generally, the prediction methods for DFFB can be classified into the following four groups: empirical correlations, phenomenological models, look-up table and mechanistic models. These methods will be briefly reviewed below, for more details the review by Andreani and Yadigaroglu (1994) is a good reference.

An often used correlation for DFFB is developed by Dougall and Rohsenow (1963), it is a Dittus-Boelter type correlation:

$$q''_w = 0.023 \frac{k_v}{D} \mathrm{Re}_{2\phi}^{0.8} \mathrm{Pr}_v^{0.4} \left(T_w - T_s\right) \tag{6.38}$$

with:

$$\mathrm{Re}_{2\phi} = \mathrm{Re}_v \left[x_e + \frac{\rho_v}{\rho_l}\left(1 - x_e\right) \right] \tag{6.39}$$

where x_e is the equilibrium quality, and all the properties are evaluated at saturation temperature. The Dougall-Rohsenow correlation requires only information on local conditions and therefore easy to use, it produces rather good prediction of the wall heat flux. However, this correlation does not predict the state of non-equilibrium, and has only limited accuracy in some situations.

The phenomenological models are based on a simplified phenomenological description of the physical process, and consider the vapor superheat. One of the highly cited phenomenological models was proposed by Chen et al. (1979), known as the CSO model. For $x_e \geq 0.5$, the thermal non-equilibrium is correlated in this model as:

$$\frac{x}{x_e} = 1 - \frac{0.26}{1.15 - \left(p/p_{cr}\right)^{0.65}} \cdot \frac{T_v - T_s}{T_w - T_v} \tag{6.40}$$

here, x is the actual quality, p_{cr} is the critical pressure. Then, based on Reynolds analogy, the convective heat transfer coefficient is inferred as:

$$h = Gxc_{p,wf} \, \mathrm{Pr}_{G,wf}^{-2/3} \frac{f}{2} \tag{6.41}$$

in which, G is the mass flux, and vapor heat capacity $c_{p,wf}$ and the Prandtl number $\mathrm{Pr}_{G,wf}$ are calculated at film temperature, $f = 0.037\,\mathrm{Re}^{-0.17}$ is the friction factor. This model has limited success at moderate to high pressure; however, it is inadequate under low mass flux and low pressure conditions.

Most of the DFFB correlations are applicable only over limited ranges of flow conditions, and most of them do not provide reasonable predictions when extrapolated outside this range. Therefore, a totally empirical approach, the look-up table based on Post-CHF data and interpolating techniques has been proposed (Groeneveld et al. 2003). However, this approach contains no understanding of the physical mechanisms in film boiling and is still under development.

The mechanistic models simulate the basic mass, momentum and energy mechanisms and calculate the evolution of all the flow variables. In these models, the empiricism is generally shifted towards the determination of the parameters entering in the closure laws (Andreani and Yadigaroglu 1994). Examples include the two-fluid model (Kawaji and Banerjee 1988) and models accounting for the distributed heat sink effect (Chung and Olafasson 1984). The mechanistic models provide more details of the flow and heat transfer field in the DFFB, however, the success of these models highly dependent on the accuracy of the closure relations and other adjustable parameters.

6.3.2 Model Description

A two-fluid model for DFFB, which includes all the heat transfer mechanisms, will be discussed in this section and then implanted into cryogenic chilldown model later.

6.3.2.1 Assumptions and conservation equations

Assumptions to derive the conservation equations for DFFB are listed as follows:

1. The liquid phase is dispersed spherical droplets, while the vapor phase is continuous.
2. The two phases are in thermodynamic non-equilibrium, the liquid phase is at saturation temperature, and the vapor phase is treated as ideal gas.
3. The vapor and liquid pressures are uniform and equal to the tube exit pressure.
4. At any given cross-section of the flow channel, all droplets have a same diameter d. The droplet diameter is a function of axial position or vapor quality x.
5. At any given cross-section of the flow channel, all droplets move with a same velocity u_d.
6. The interfacial velocity is the same as the droplet velocity.

The assumption 3 is based on the fact that the pressure drop in the dispersed region is very small compared with the total pressure drop. Under this assumption, the pressure is not an unknown, and the vapor momentum equation does not need to be solved, therefore the problem is significantly simplified.

As stated in assumption 4, single-droplet formulation is used in current study. The reason for this assumption lies in two aspects. First, the work of Kawaji and Banerjee (1988) included both the single-droplet formulation and multi-field approach, in which the droplet size distribution was modeled by eleven groups of droplets, and the two methods resulted in fairly good agreement. The multi-field approach did not show discernable advantage over the single-droplet formulation in their work. On the other hand, the droplet size distribution function used in the model work is often "adjustable", this function has not been well correlated to many influencing parameters from the experiments as discussed in previous section.

For vertical tube, the transient one-dimensional two-fluid equations for DFFB region are given as below:

Continuity equation:

$$\frac{\partial}{\partial t}\left(\alpha_l \rho_l\right)+\frac{\partial}{\partial z}\left(\alpha_l \rho_l u_d\right)=-m_l''' \tag{6.42}$$

$$\frac{\partial}{\partial t}\left(\alpha \rho_v\right)+\frac{\partial}{\partial z}\left(\alpha \rho_v u_v\right)=m_l''' \tag{6.43}$$

Momentum equation:

$$\frac{\partial}{\partial t}\left(\alpha_l \rho_l u_d\right)+\frac{\partial}{\partial z}\left(\alpha_l \rho_l u_d u_d\right)=\pm \alpha_l \rho_l g+\tau_d''' \tag{6.44}$$

Vapor enthalpy equation:

$$\frac{\partial}{\partial t}\left(\alpha \rho_v h_v\right)+\frac{\partial}{\partial z}\left(\alpha \rho_v u_v h_v\right)=q_v'''+m_l'''\left(h_{vs}-h_v\right) \tag{6.45}$$

The density of vapor phase is calculated form Equation 6.8. In the above equations, subscript *d* is for liquid phase, *v* is for vapor phase and *s* denotes saturation; m_l''' is the interfacial mass transfer rate per unit volume with unit of [$\mathrm{kg/m^3s}$]; q_v'' is the heat flux used to heat up the vapor; for the body force in the momentum equations, plus sign is for down-flow, and minus sign is for up-flow.

6.3.2.2 Heat transfer in dispersed flow film boiling and constitutive relations

Heat transfer in the DFFB region is rather complex. In Figure 6-7 the heat and mass transfer mechanisms in DFFB are illustrated as (Andreani and Yadigaroglu 1994; Guo and Mishima 2002):

1. Convective heat transfer from the wall to the vapor q''_{wv};
2. Interfacial heat transfer between the vapor and droplets q''_{vd};
3. Direct contact wall-to-droplet heat transfer q''_{wd};
4. Radiative heat transfer from the wall to the droplets $q''_{r,wd}$;
5. Radiative heat transfer from the wall to the vapor $q''_{r,wv}$;
6. Radiative heat transfer from the vapor to the droplets $q''_{r,vd}$;
7. Evaporation of the droplets m''_{l}.

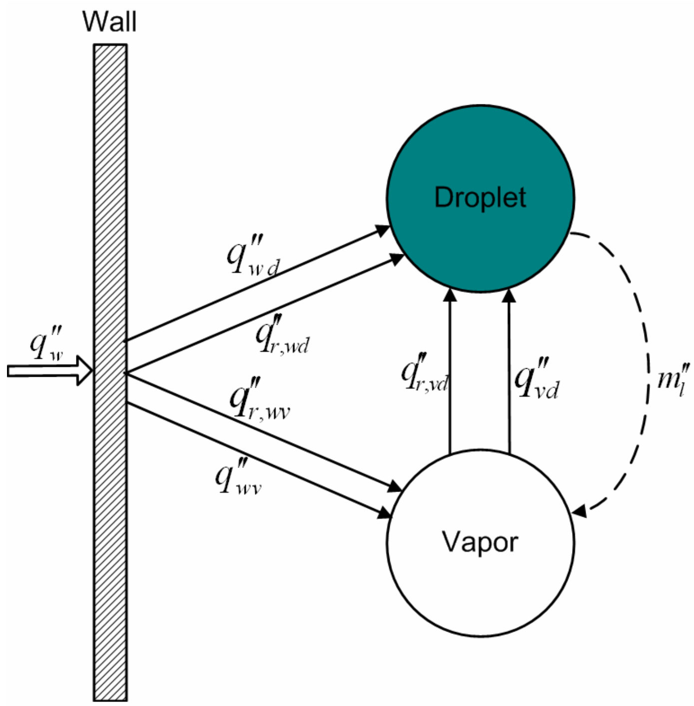

Figure 6-7. Heat and mass transfer mechanisms in DFFB.

There might be some confusion by using the term direct contact wall-to-droplet heat transfer. In DFFB, the wall temperature is generally higher than the Leidenfrost temperature, therefore when the droplets are in the vicinity of the wall; a thin vapor film will separate it from in touch with the wall. In this context, the term actually means the heat transfer through this thin vapor film. Only in very few occasions, the droplets can have enough momentum to penetrate the vapor film and wet the wall. Some literature (Carey 1992) name the former and the later as dry contact and wet contact, respectively. However, the wet contact is generally considered negligible, and the direct contact heat transfer has been used in most of the literature, although misleading literally. This tradition is followed in current study.

Convective heat transfer from the wall to the vapor. This part contributes most to the total heat removal from the wall, and is modeled as:

$$q''_{wv} = 0.023\frac{k_v}{D}\mathrm{Re}_v^{0.8}\,\mathrm{Pr}_v^{0.33}\left(T_w - T_v\right) \tag{6.46}$$

in which, *D* is the tube ID and Re_v is the vapor Reynolds number.

Interfacial heat transfer between vapor and droplets. This part is calculated by the Lee-Ryley model (Lee and Ryley 1968):

$$q''_{vd} = \frac{k_v}{d}\left(2 + 0.74\,\mathrm{Re}_d^{0.5}\,\mathrm{Pr}_v^{0.33}\right)\left(T_v - T_s\right) \tag{6.47}$$

here, *d* is the droplet diameter, Re_d is the droplet Reynolds number that defined as:

$$\mathrm{Re}_d = \frac{\rho_v\left(u_v - u_d\right)d}{\mu_v} \tag{6.48}$$

Direct contact wall-to-droplet heat transfer. This part is usually much smaller than the convective heat transfer from the wall to the vapor, and is modeled by (Guo and Mishima 2002):

$$q''_{wd} = \left[\frac{18k_v^3 t_R^3 \rho_v h'_{lv} \dot{m}_d^5}{d^5 \rho_l^4 \mu_v \left(1-\alpha\right)\left(T_w - T_s\right)}\right]^{1/4}\left(T_w - T_s\right) \tag{6.49}$$

in which $h'_{lv} = h_{lv} + C_p\left(T_v - T_s\right)$, is the modified latent heat; t_R is the droplet resident time, which characterizes the average time that the droplet in contact with the wall, and is given by Bolle and Moureau (1986) as:

$$t_R = \pi\sqrt{\rho_l d^3/16\sigma} \tag{6.50}$$

$\dot{m}_d$ is the deposition rate, which represents the droplet mass impinging rate to the wall per unit area, and given by Kataoka and Ishii (1983) as:

$$\dot{m}_d = K\left(1-\alpha\right)\rho_l \tag{6.51}$$

where K is the deposition mass transfer coefficient, given as:

$$K = \frac{\mu_l}{D} 0.22\,\mathrm{Re}_l^{0.74}\left(\frac{\mu_v}{\mu_l}\right)^{0.26} E^{0.74} \tag{6.52}$$

here, E denotes the fraction of liquid droplet entrainment in the vapor core and equals to unity for dispersed flow.

Radiative heat transfer. The radiation heat transfer among the wall, the vapor and the droplet is usually small. When the radiation is considered, the method proposed by Sun et al. (1976) is highly cited. The wall, the vapor, and the droplets are characterized by an electrical network as shown in Figure 6-8.

The radiation heat fluxes can then be expressed as:

$$q''_{r,wv} = \left(R_w + R_v + R_w R_v / R_d\right)^{-1} \sigma_B \left(T_w^4 - T_v^4\right) \tag{6.53}$$

$$q''_{r,wd} = \left(R_w + R_d + R_w R_d / R_d\right)^{-1} \sigma_B \left(T_w^4 - T_s^4\right) \tag{6.54}$$

$$q''_{r,vd} = \left(R_v + R_d + R_v R_d / R_w\right)^{-1} \sigma_B \left(T_v^4 - T_s^4\right) \tag{6.55}$$

where

$$R_v = (1-\varepsilon_v)\big/\left[\varepsilon_v(1-\varepsilon_v\varepsilon_d)\right] \tag{6.56}$$

$$R_d = (1-\varepsilon_d)\big/\left[\varepsilon_d(1-\varepsilon_v\varepsilon_d)\right] \tag{6.57}$$

$$R_w = 1\big/(1-\varepsilon_v\varepsilon_d) + (1-\varepsilon_w)\big/\varepsilon_w \tag{6.58}$$

In the above equations, ε_w, ε_v and ε_d are emissivity of the wall, the vapor and the droplets, respectively.

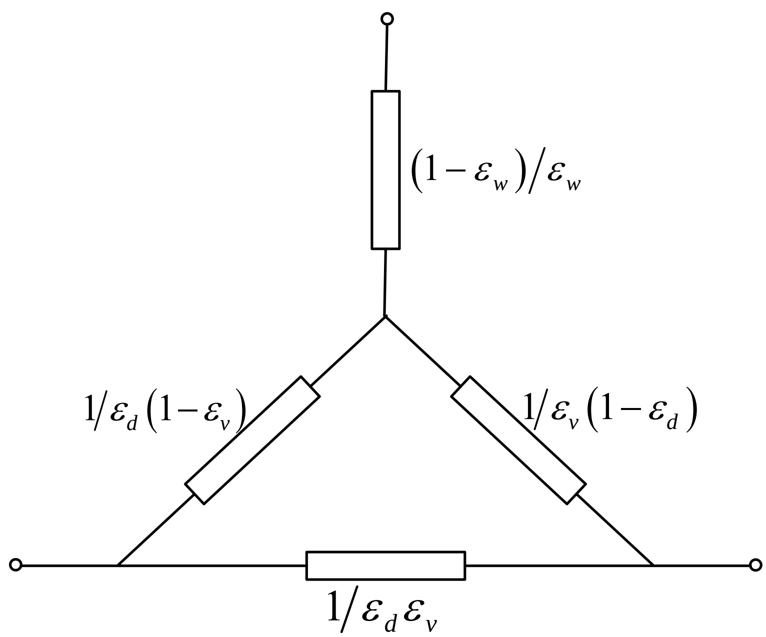

Figure 6-8. Electrical analog of radiation heat transfer in DFFB.

Interfacial mass transfer rate. All the heat absorbed by the liquid phase is assumed to be used to evaporate the liquid droplets. From energy balance, the heat used to evaporate the droplets per unit volume is given by:

$$q'''_{evap} = A_i''' q''_{vd} + \frac{4}{D}\left(q''_{r,vd} + q''_{wd} + q''_{r,wd}\right) \tag{6.59}$$

The interfacial mass transfer rate per unit volume in the model equations is, therefore:

$$m_l''' = q'''_{evap}\big/h_{lv} \tag{6.60}$$

here, because of the difference in the heat transfer area for different heat transfer mechanisms, A_i''' and $\frac{4}{D}$ appear in Equation 6.59.

For a flow channel with length *l* and contains *n* droplets with diameter of *d*, the interfacial area is:

$$A_i = n\pi d^2 \tag{6.61}$$

while, the sum of the total volume of the droplets over the flow channel volume is the liquid fraction, this gives:

$$A_i = \frac{3(1-\alpha)\pi D^2 l}{2d} \tag{6.62}$$

and the interfacial area per unit volume of the flow channel is:

$$A_i''' = \frac{6(1-\alpha)}{d} \tag{6.63}$$

The vapor to droplet convective heat transfer area equals the interfacial area, while the other heat transfer mechanisms are considered to take place at the wall.

Vapor heating term. The vapor phase is heated by the wall and passes part of this heat to evaporate the liquid droplets. The vapor heating term in Equation 6.45 is given as:

$$q_v''' = \frac{4}{D}\left(q_{wv}'' + q_{r,wv}'' - q_{r,vd}''\right) - A_i''' q_{vd}'' \tag{6.64}$$

Interfacial drag term. The interfacial drag on the droplets per unit volume is calculated by:

$$\tau_d''' = \frac{6(1-\alpha)F_D}{\pi d^3} \tag{6.65}$$

where F_D is the drag force on one droplets, which was suggested by Rowe (1961) as:

$$F_D = \frac{C_D}{2} \rho_v \left| u_v - u_d \right| \left(u_v - u_d \right) \frac{\pi}{4} d^2 \tag{6.66}$$

in which, the drag coefficient is given as:

$$C_D = \frac{24}{\mathrm{Re}_d} \left(1 + 0.15 \mathrm{Re}_d^{0.687} \right) \tag{6.67}$$

Droplet diameter. The droplet diameter is an important parameter, and is evaluated by the model of Kataoka et al. (1983):

$$d = 7.96 \times 10^{-3} \frac{\sigma}{\rho_v \left(\alpha u_v \right)^2} \mathrm{Re}_v^{2/3} \left(\frac{\rho_v}{\rho_l} \right)^{-1/3} \left(\frac{\mu_v}{\mu_l} \right)^{2/3} \tag{6.68}$$

6.4 Application of a Two-Fluid Model to Cryogenic Chilldown

In this section, a cryogenic chilldown model is developed with four regions. Previously discussed IAFB and DFFB model are introduced into this cryogenic chilldown model. The code validation of the cryogenic chilldown model is given in the Appendix.

6.4.1 Model Description

Chilldown process inside of a vertical stainless steel tube is modeled. The tube, which is inside of a vacuum jacket, has 0.635cm OD, 0.432cm ID, and 70 cm length. Saturated liquid nitrogen is injected from the bottom of the tube at certain fixed inlet flow rate. The computation has been carried out for both normal gravity case and microgravity case.

6.4.1.1 Fluid flow

When saturated liquid nitrogen with a small initial void fraction as in Equation 6.29 enters from the bottom of the tube, the two-phase flow is in IAFB state. The two-fluid

IAFB model discussed in previously is used to describe the two-phase flow behavior in this region.

The void fraction keeps increasing as the two-phase flow propagating downstream. In current study, the transition criterion from IAFB to DFFB is set as $\alpha = 0.90$. The governing equations for DFFB are given in Equation 6.42-6.45, and the pressure drop is neglected in DFFB region. The boundary conditions at the transition interface are given from the upstream IAFB region.

If the flow channel is enough long, all the liquid droplets in the DFFB front will be evaporated eventually and the flow becomes fully vapor. In this study, when the void fraction reaches 0.99, the effect of the liquid phase is neglected and the flow is modeled as fully vapor, in which the only heat transfer mechanism is due to the forced convection to the vapor:

$$q''_{wv} = 0.023 \frac{k_v}{D} \mathrm{Re}_v^{0.8} \mathrm{Pr}_v^{0.33} \left(T_w - T_v \right) \tag{6.69}$$

When the tube wall has been chilled down to rewetting temperature, intermittent liquid-wall contact is established and transition boiling begins. The transition boiling, characterized by rapid bubble generation, is highly unstable and immediately replaced by the nucleate boiling. Model the transition boiling region in chilldown is generally a difficult task, because the understanding and experimental data of the transition boiling are still very limited at current stage. On the other hand, the transition boiling period in chilldown process is so short and the heat flux of transition boiling is in the same order as that of the nucleate boiling, therefore nucleate boiling correlations are used to model both the transition boiling region and the nuclear boiling region in this work, this approach is also adopted by other researches (Kawaji and Banerjee 1988; Hedayatpour et al. 1993).

The Chen's correlation (Chen 1966) for nucleate boiling is used, in which the total heat transfer coefficient equals to the sum of a microscopic (nucleate boiling) contribution h_{mic} and a macroscopic (bulk convection) contribution h_{mac}, in addition, h_{mic} is evaluated by pool boiling correlation times a suppression factor $S\left(\mathrm{Re}_{2\phi}\right)$; while h_{mac} is proposed to be enhanced from single liquid convection with a enhancement factor $F\left(X_{tt}\right)$. The Chen's correlation gives:

$$h = h_{pool} S\left(\mathrm{Re}_{2\phi}\right) + h_l F\left(X_{tt}\right) \tag{6.70}$$

where

$$h_{pool} = 0.00122\left[\frac{k_l^{0.79} c_{pl}^{0.45} \rho_l^{0.49}}{\sigma^{0.5} \mu_l^{0.29} h_{lv}^{0.24} \rho_v^{0.24}}\right]\left(T_w - T_s\left(P_l\right)\right)^{0.24}\left(P_s\left(T_w\right) - P_l\right)^{0.75} \tag{6.71}$$

$$h_l = 0.023\frac{k_l}{D}\mathrm{Re}_l^{0.8}\,\mathrm{Pr}_l^{0.4} \tag{6.72}$$

In Equation 6.70, $\mathrm{Re}_{2\phi}$ is the two-phase Reynolds number, X_{tt} is the Martinelli parameter. For details can refer to Chen (1966).

In some other chilldown models (Kawaji and Banerjee 1988; Hedayatpour et al. 1993), the location and the propagation of the quenching front are a prior; these models begin with the IAFB and move back to the upstream of the quenching front after solving the Post-CHF region. In this study, instead, the rewetting temperature is used as the transition criterion from the film boiling to nucleate boiling. Whenever the wall temperature is quenched below the rewetting temperature, the nucleate boiling model will be started. The rewetting temperature is not a fixed value but affected by flow rate, fluid and wall properties, etc. Fortunately, for the same experimental setup and limited range of working conditions, the rewetting temperature is generally a constant. Therefore, use the rewetting temperature acquired from the experiments as transition criterion is expected to be applicable to similar experimental conditions. A reliable correlation for rewetting temperature is desirable and will generalize current chilldown model.

6.4.1.2 Heat conduction in tube wall

The wall temperature is obtained by solving the 1-D transient heat conduction equation:

$$\rho_w c_{p,w} \frac{\partial T_w}{\partial t} = k_w \frac{\partial^2 T_w}{\partial z^2} \tag{6.73}$$

6.4.1.3 Initial and boundary conditions

Initially the whole tube is at a constant temperature of T_0, the tube is filled with pure vapor which is in thermal equilibrium with the tube.

Saturated liquid nitrogen is injected from the bottom of the tube under constant flow rate; a small inlet void fraction and a small inlet slip velocity are assigned at flow inlet, as summarized in Equation 6.29.

Adiabatic boundary condition is set at the inlet wall, outlet wall and outer surface. For the inner surface, different correlations are used for the four regions, and are summarized in Table 6-2.

Table 6-2. Inner wall boundary conditions at different regions.

Region	Boundary condition	Equation used
Fully vapor	$q''_w = q''_{wv}$	6.69
DFFB	$q''_w = q''_{wv} + q''_{wd} + q''_{r,wv} + q''_{r,wd}$	6.46, 6.49, 6.53, 6.54
IAFB	$q''_w = q''_{wv} + q''_r$	6.17, 6.23
Transition and nucleate boiling	$q''_w = h\left(T_w - T_s\right)$	6.70

6.4.2 Numerical method and solution procedure

A semi-implicit, finite difference scheme is used in the chilldown model. Very small time step is used to avoid the instability that is inherent in the two-fluid model. The 1-D heat conduction equation is solved by TDMA method with totally 200 nodes. The solution procedure is illustrated in Figure 6-9. First, the initial conditions for both the tube wall and the flow field are given, and the CHF location Z_{CHF} is set at the tube inlet. Then the calculation begins with a initial guess of α, P, u_l, u_v, h_v.

In this model, Post-CHF models are used for downstream of the CHF point, while nucleate boiling model is applied to upstream of CHF point. In Post-CHF calculation the void fraction increases along axial direction, whenever the calculated void fraction reaches the two critical values, it is considered as a flow regime transition, and therefore a different model is selected. After solving the flow field, the wall temperature is updated according to Equation 6.73. A pre-defined rewetting temperature is used as transition criterion between the Post-CHF and nucleate boiling region. The location where the wall temperature becomes lower than the rewetting temperature is set as the new CHF location, and the program iterates until the wall temperature converges. This will finish the computation in one time step. For the whole chilldown process, the program ends until the calculation time is larger than the experiment time.

6.4.3 Results and Discussion

The cryogenic chilldown model can be used for top-flooding, bottom-flooding and microgravity cases, and is capable of predicting both the flow field and temperature field. In this part, the feasibility of this model is addressed by comparing the model results with experimental data.

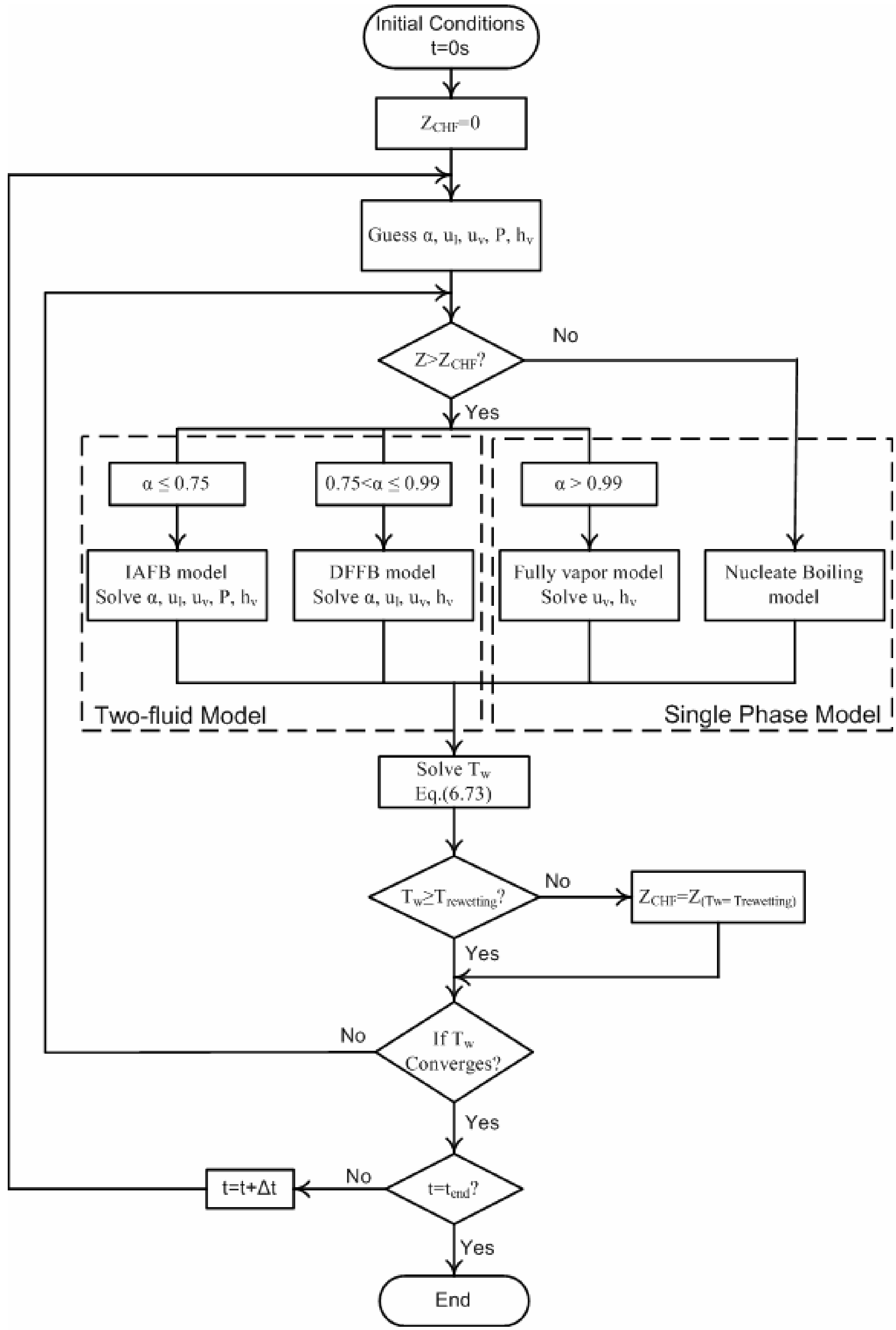

Figure 6-9. Solution procedure of the cryogenic chilldown model.

6.4.3.1 Experimental results

One of the important aims to develop the cryogenic chilldown model is for the prediction of chilldown process under microgravity, for which systematic experiments are often difficult and costly. In the literature, to the author's knowledge, the only experimental investigation covers the whole cryogenic chilldown process under low gravity environment was conducted by Antar and Collins (1997). Their work is reviewed as follows.

The cryogenic chilldown experiments were carried by Antar and Collins (1997) under both terrestrial and low gravity environments with same experimental apparatus. The low gravity environment, which has an average gravitational acceleration of $\pm 0.01g$, was provided by a NASA KC-135 aircraft. During the test, the low gravity time lasted about 25 seconds, while the test section is usually chilled down within 20 seconds; therefore the low gravity duration is sufficient long.

Two different test sections were used in the experiments. A quartz tube, having 1.275 cm OD and 1.05 cm ID and approximately 60 cm long, was used for the purpose of recording the flow regimes; another stainless steel test section was used for wall temperature measurement. The stainless steel test section, which has the dimension of 0.635 cm OD, 0.432 cm ID, and 70 cm length, will be modeled in current study. Both test sections were mounted vertically inside a vacuum jacket. Saturated liquid nitrogen was injected from the bottom of the test section, while the top of the test section was opened to atmosphere. A stainless steel bellows, inside of a liquid nitrogen accumulator, was used to store the liquid nitrogen before each test. The bellows was compressed from the outside with gaseous helium at approximately constant pressure to supply liquid nitrogen.

The two main variables in the experiment were the nitrogen flow rate and the initial tube temperature. The results shown in the paper has a flow rate range of about 35-55 cc/s. The tube was initially at room temperature, after each test the wall temperature was always brought above 0^0C. Three type T thermocouples were soldered to the outside wall of the stainless steel test section; however, one thermocouple was reported to give erratic signals during the test, and only the other two thermocouple measurements were given. These two thermocouples located at 20 cm and 30 cm from the inlet, respectively.

In low gravity tests, the flow sequence before rewetting was reported as: fully vapor flow, dispersed flow, and then followed by filamentary flow, in which "the liquid took the form of long liquid filaments meandering in the center of the pipe which were surrounded by a vapor blanket separating them from the test section wall". Single filaments were always observed to grater than 10 tube diameter and in general had a diameter of about one third that of the test section. However, the reported images are rather unclear.

Although the author claimed that the observed filamentary flow structure in low gravity is a new and unique flow pattern, and has two characteristics that different from IAF regime in ground tests, it is believed that the filamentary flow structure actually belongs to IAF regime by a further study and comparison with other experiments. The reasons will be given below.

As described by Antar and Collins (1997), the two characteristics of the filamentary flow were: first, in low gravity the diameters of the liquid filaments were smaller than that of the IAF; and second, the liquid filaments extended to longer distances than that in the IAF, which has a length about three tube diameters.

However, liquid filament with smaller diameter is actually classified as inverted annular flow pattern and had been reported in microgravity experiments previously. For example, a series microgravity quenching experiments using R-113 conducted by Kawaji et al. (1991) reported that “the inverted annular-like flow regime in microgravity showed a much thicker vapor film in comparison with that seen in 1-g tests. In microgravity, the liquid core was often much thinner, more closely resembling a thick cylindrical liquid filament which was mostly smooth and continuous but sometimes bulged at some places nearly filling the tube volume without rewetting the tube surface”.

On the other hand, the thicker vapor film in microgravity alleviates the heat transfer from the wall to the liquid core, and the liquid core is expected to extend longer before breaking into dispersed flow. Even in the ground test, the IAFB region is not always short. If the heat flux from the wall is pretty low as in chilldown experiments, the liquid core in IAFB region could be much longer than three tube diameter (Lee and Kim 1987).

From the above reasons, the sequence of the flow regime in microgravity cryogenic chilldown process is modeled as fully vapor, dispersed flow, IAF, and nucleate boiling.

The temperature measurements (Antar and Collins 1997) show that the rewetting temperature is rather a constant, which is about 115K, in the experimental flow rate range. The wall temperature drops very quickly at this point. Therefore the transition criterion to nucleate boiling is set as 115K. The transition boiling period is found to be very short and usually less than one second.

6.4.3.2 Model results and comparisons

Figure 6-10 shows the measured and predicted wall temperatures under 1-g condition. The two thermocouples are located at 20cm and 30cm from the inlet, and the flow rate is approximately 40cc/s according to the inlet pressure and flow rate relation given by Antar and Collins (1997).

The model slightly over-predicts the temperature decreasing speed before the rewetting point and thus leads to an earlier transition to the nucleate boiling region, the overall agreement is good. It is noted that the initial condition of the experiment was not well controlled so that there is a temperature difference of about 25K between the initial thermocouple responses as shown in Figure 6-10; while in current model, the tube is assumed at same initial temperature. The scatter between the model prediction and the experimental data for thermocouple location at 30cm from the inlet comes mainly from this initial difference.

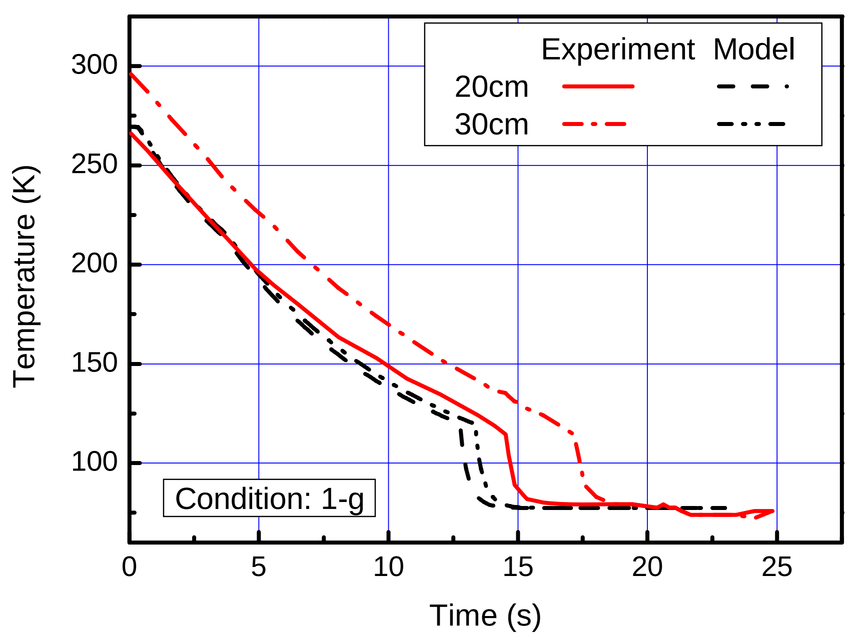

Figure 6-10. Comparison between measured and predicted wall temperatures under 1-g condition with flow rate of 40cc/s.

Comparison between microgravity tests and model predictions is illustrated in Figure 6-11. Again, good agreement is achieved. Contrary to the 1-g case, the model under-predicts the temperature decreasing speed very slightly. This discrepancy is believed to come from the residual gravity effect in the experiment. The KC-135 aircraft generally produces reduced to micro-g gravity level (about 0.05~0.01g), the detailed g-level fluctuates in one test and differs from test to test. Antar and Collins (1997) did not give the approximated g-level in their tests. As shown by many researchers the gravity force can improve the film boiling heat transfer. In present study the model results are for 0-g, therefore the model slightly under-predicts the temperature decreasing speed.

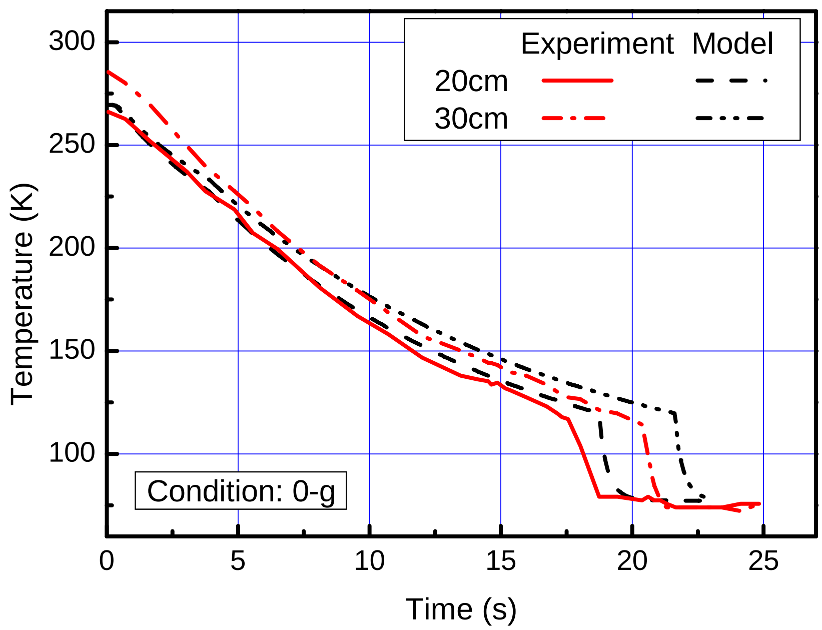

Figure 6-11. Comparison between measured and predicted wall temperatures under 0-g condition with flow rate of 40cc/s.

Figure 6-12 shows the prediction of the transient wall temperatures at different axial locations along the tube under both 1-g and 0-g conditions with a flow rate of 40cc/s. The three locations in the figure are 1mm, 20cm and 30cm from the inlet, respectively.

Obviously, the tube wall closer to the inlet is quenched more quickly. Moreover, the gravity effect is found to be less important near the tube inlet (1mm line), because the void fraction is very small there and the flow is almost single liquid. The gravity effect is found to increase along the axial direction.

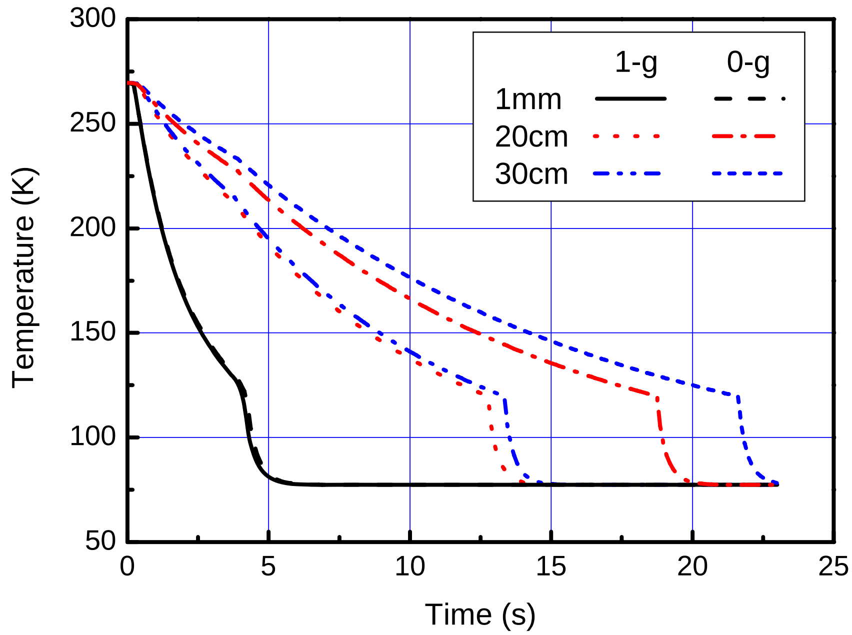

Figure 6-12. Model prediction of wall temperatures at different axial locations under both 1-g and 0-g conditions.

Effects of the inlet flow rate and gravity level are illustrated in Figure 6-13. As seen from Figure 6-13A, higher flow rate is associated with quicker temperature decrease, and this effect is more important further downstream. Figure 6-13B illustrates that in film boiling region the heat transfer rate decreases with decreasing gravitational acceleration.

After rewetting point, the correlation used in this model does not include the gravity effect, therefore the temperatures decreasing at about the same speed at transition and nucleate boiling region under different g-levels. The experiment of Merte and Clark (1964) showed that in the transition and nucleate boiling region, the boiling curve is almost unchanged under different g-levels. On the other hand, it is the rewetting point that usually of particular interest in engineering application, the current model clearly demonstrates the gravity effect on the film boiling region, and is, therefore, very important in Post-CHF flow and heat transfer prediction.

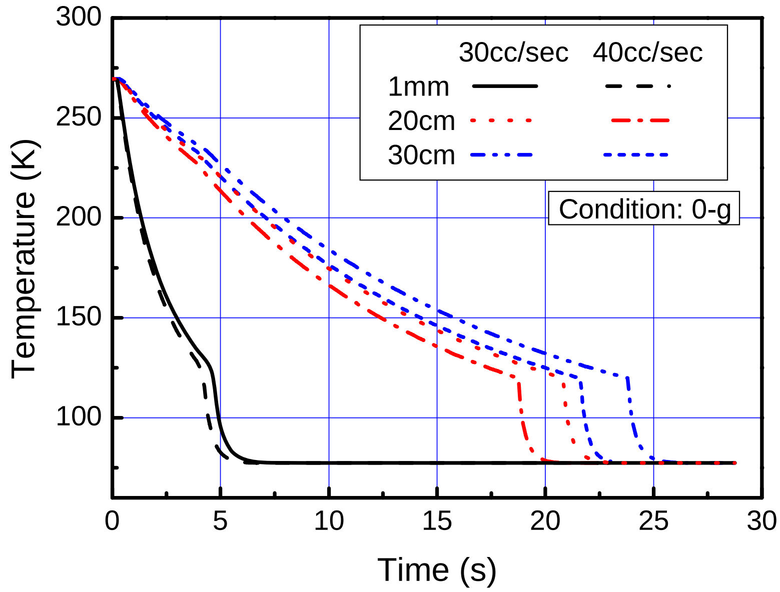

A

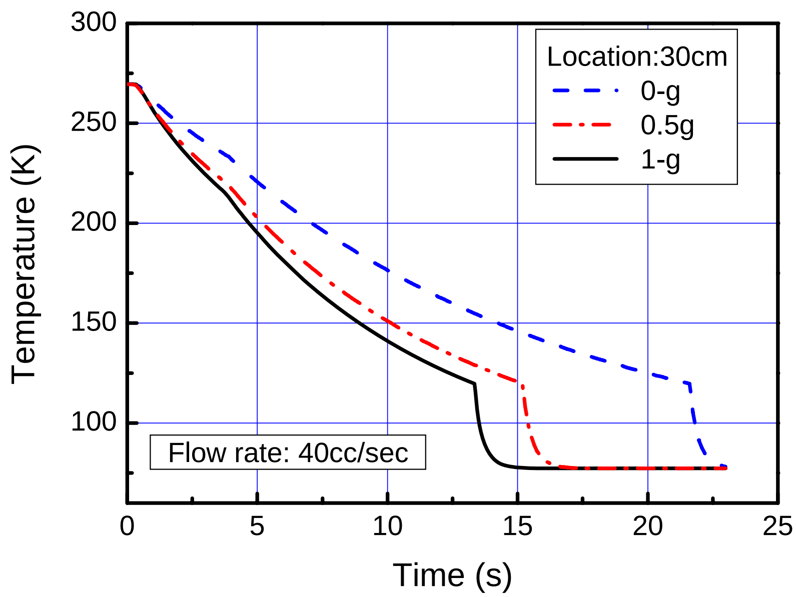

B

Figure 6-13. Effects of inlet flow rate and gravity level on chilldown process. A) Effect of inlet flow rate. B) Effect of gravity level.

Figure 6-14 gives the wall temperature profiles at different time. Wall temperature decreases with time and increases along the axial direction. In the beginning, the maximum temperature gradient is at the tube inlet, when QF appears, the maximum temperature gradient moves with the QF.

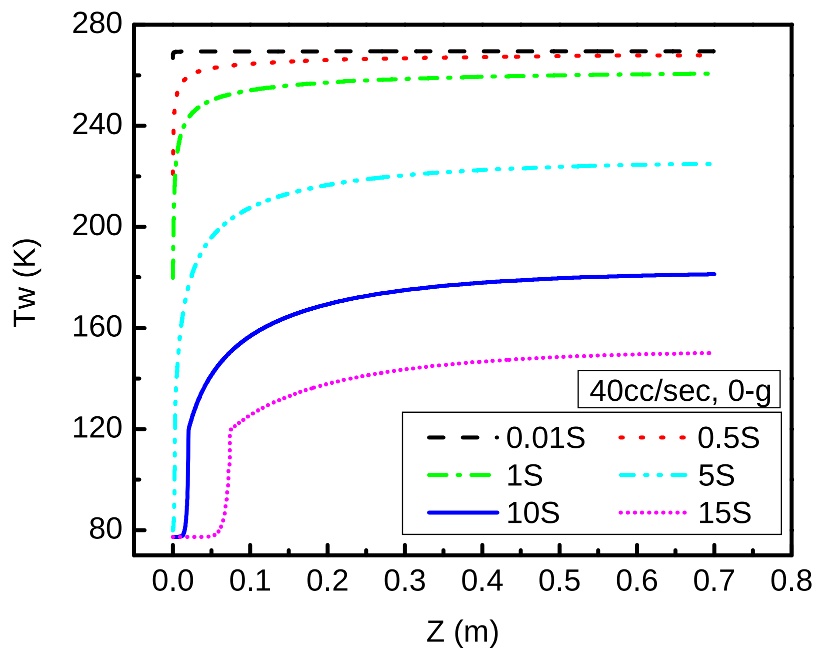

Figure 6-14. Wall temperature profiles at different time.

The void fraction at different time under 0-g condition is shown in Figure 6-15. The void fraction increases along the axial direction since more and more liquid is evaporated as the flow propagates.

The driving potential of the evaporation, the temperature difference between the wall and the liquid saturation temperature, keeps decreasing as the tube is being chilled down; therefore pace of the void fraction increasing rate slows down as shown in Figure 6-15. Particularly, in the beginning stage the wall is very hot, the void fraction shows an abrupt increases along the axial direction, and the flow regime changes from IAF to dispersed flow and then to fully vapor flow. Later on, the fully vapor region and dispersed region are totally pushed out of the tube and the exit state of the two-phase flow is in IAFB, and finally, QF appears and sweeps downstream.

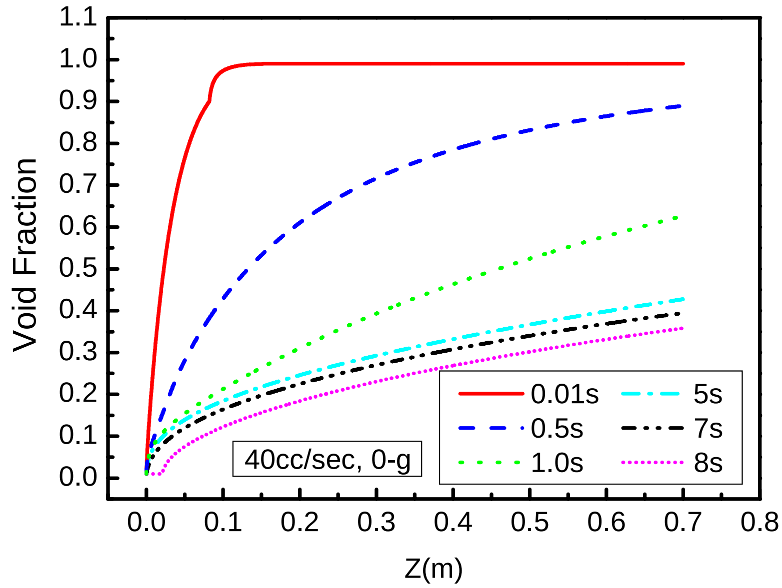

Figure 6-15. Void fraction along the tube during chilldown.

6.5 Conclusions

In this chapter, cryogenic chilldown process is divided into four regions which are fully vapor region, DFFB region, IAFB region, and nucleate boiling region. Then a cryogenic two-fluid chilldown model is developed with each of these four regions modeled in different strategy. The model can be applied to both vertical tube chilldown case and microgravity chilldown case. The model predictions and the experimental results have a good agreement.

CHAPTER 7
CONCLUSIONS AND RECOMMENDATIONS

In current study, chilldown experiments have been conducted under both 1-g and microgravity conditions. A two-fluid model is developed for both vertical tube chilldown and chilldown under microgravity. Major conclusions of current study and recommendations for future research are to be given in this chapter.

7.1 Conclusions

1. The experiments show that the chilldown process can be generally divided into three regions: film boiling region, transition boiling region and nucleate boiling region, and each region is associated with different flow regime and heat transfer mechanism. After data reduction, chilldown boiling curve, which is similar to the pool boiling curve, is generated based on the wall temperature measurement. The limits between different regions of the chilldown process are clearly shown as the point of the critical heat flux (CHF) and the minimum heat flux on the chilldown boiling curve.

2. Experiments have been conducted under three different low flow conditions. It has been observed that the two-phase flow is dispersed in the film boiling region with liquid phase in the form of long filaments as the tube is chilled down, while the vapor phase is generally superheated. The heat transfer mechanism at the bottom wall is film boiling to the liquid filaments and convection to the superheated vapor phase, the upper wall transfers heat mainly by convection. The statistic feature of the liquid filaments is studied and it has been shown that the thickness of the filaments shows very limited increase with increasing mass flux and does not present a strong correlation with the wall temperature; while the length of the filaments is more scattered at higher mass fluxes and lower wall temperatures.

3. Based on the experimental result, a phenomenological model, in which the heat transfer at the bottom is considered as a sum of vapor and liquid components, has been developed. Good agreement is achieved between the model prediction and the experimental result.

4. Rewetting experiments show that rewetting temperature and rewetting velocity increases with increasing mass flux. The rewetting process is observed as the appearance of the rewet spots followed by the growth and spread of the rewet spots in both direction, and finally the establishment of the quenching front.

5. Cryogenic chilldown under microgravity condition is experimentally studied. In the film boiling region, the bottom wall heat flux is found to decrease under microgravity condition. Under current experimental condition, the gravity effect does not show a strong dependence on wall temperature and inlet flow rate.

6. A two-fluid cryogenic chilldown model has been developed to predict both vertical tube and microgravity chilldown process. The model contains four distinct regions, which are fully vapor region, dispersed flow film boiling (DFFB) region, inverted annular film boiling (IAFB) region, and nucleate boiling region. Two-fluid equations are applied to the DFFB region and the IAFB region, the fully vapor region and nucleate boiling region are depicted with single-phase correlations. Constitutive relations and transition criteria between different regions are studied and provided to close the chilldown model. Comparison between the model results with previous experimental data (Antar and Collins1997) shows a good agreement.

7.2 Recommendations for Future Research

In current research, both experimental and modeling work have been conducted to advance the understanding of the cryogenic chilldown process and significant progress has been achieved, however, due to the complicity of the problem there are several key issues remain unsolved and the following are recommended for future investigations:

1. The effects of the test section dimension and the thermal and surface properties of the wall have not been investigated in current experiments. It is suggested to include these effects in the future experiments.

2. The gravity effect on the film boiling region has been studied in this research. The transition region and nucleate boiling region are not included and needs further exploration.

3. In chilldown model, the droplet diameter is the most important parameter in DFFB region. More experimental observations are desirable to provide reliable database of the droplet size and distribution function for modeling work.

4. Transition from the IAFB region to the DFFB region has been observed by some researchers as large liquid chunks travel in vapor phase and break into liquid droplets shortly after their generation. Current model work does not include this short transition region and use void fraction as the transition criterion instead. Future research is suggested to advance this model by adding this transition region with necessary closing relations.

APPENDIX
CODE VALIDATION

In this section, the code for chilldown model is validated in two ways. First, the code is used to simulate the dam-break problem and the computation results are compared with analytical solution. Next, the grid independence of the code is tested.

A.1 Dam-Break Problem

Dam-break problem is one of the effective tests of numerical prediction because it has an analytical solution that contains discontinuities, and this allows a sensitive check on the effects of numerical diffusion in code predictions.

Assume a reservoir contains still water with flat surface of height h_1, on the other side of the reservoir, the water height is h_0 (Figure A-1), suddenly the dam of the reservoir is removed and results a transient 1-D flow due to the gravity.

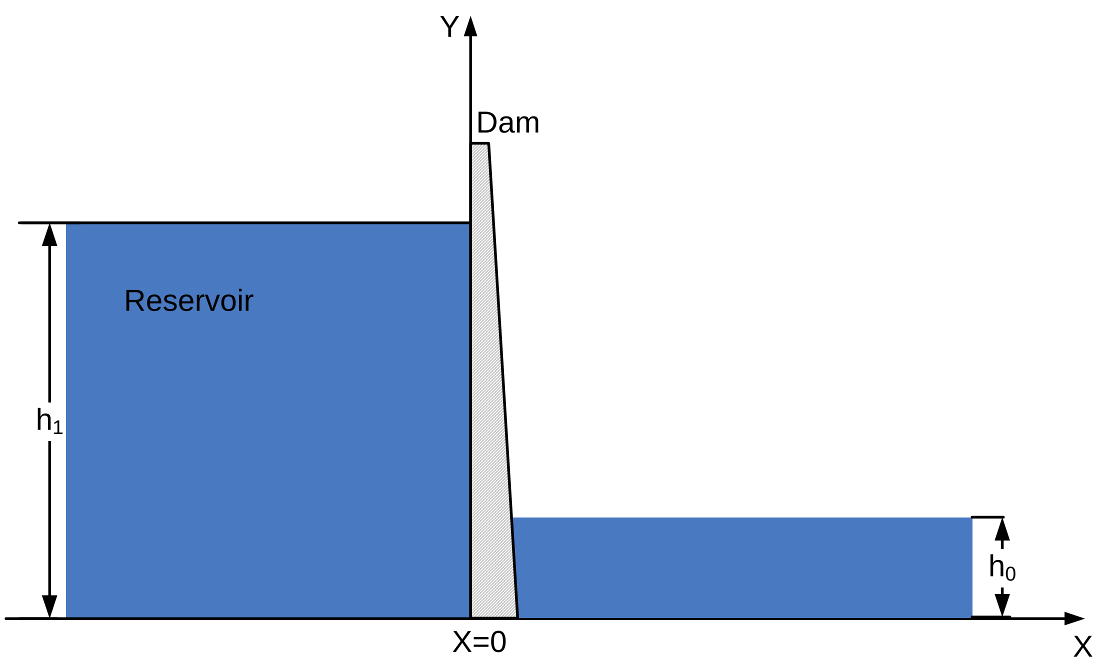

Figure A-1. Dam-break flow model.

If there is no friction on the wall and no viscous stress in the fluid, and air pressure is constant, an analytical solution for the liquid level and liquid velocity is given by Zoppou and Roberts (2003). The result is shown in Table A-1.

Table A-1. Analytical solution of dam-break problem for horizontal frictionless channel.

Range	Dependent variable
$x \le -t\sqrt{gh_1}$	$u = 0 \quad h = h_1$
$-t\sqrt{gh_1} < x \le t\left(u_2 - \sqrt{gh_2}\right)$	$u = u_3 = \frac{2}{3}\left(\sqrt{gh_1} + \frac{x}{t}\right) \quad h = h_3 = \frac{4}{9g}\left(\sqrt{gh_1} - \frac{x}{2t}\right)^2$
$t\left(u_2 - \sqrt{gh_2}\right) < x < tS_2$	$u = u_2 = S_2 - \frac{gh_0}{4S_2}\left(1 + \sqrt{1 + \frac{8S_2^2}{gh_0}}\right)$ $h = h_2 = \frac{h_0}{2}\sqrt{1 + 8\left(\frac{2h_2}{h_2 - h_0}\frac{\sqrt{h_1} - \sqrt{h_2}}{\sqrt{h_0}}\right)^2} - \frac{1}{2}$
$tS_2 \le x$	$u = 0 \quad h = h_0$

In Table A-1, S_2 is the shock speed and given by:

$$S_2 = 2\sqrt{gh_1} + \frac{gh_0}{4S_2}\left(1 + \sqrt{1 + \frac{8S_2^2}{gh_0}}\right) - \left(2gh_0\sqrt{1 + \frac{8S_2^2}{gh_0}} - 2gh_0\right)^{1/2} \tag{A.1}$$

The governing equations for this 1-D dam-break problem can be expressed as:

$$\frac{\partial u_l}{\partial t} + u_l\frac{\partial u_l}{\partial x} = -g\frac{\partial h_l}{\partial x} \tag{A.2}$$

$$\frac{\partial h_l}{\partial t} + \frac{\partial u_l h_l}{\partial x} = 0 \tag{A.3}$$

here, u_l is liquid velocity, h_l is liquid height, and $g = 10$ m/s^2 is the gravitational acceleration. Length of the computation region is 2000m, and the initial and boundary conditions are listed as:

$$u(x,0) = 0, \quad h(x,0) = \begin{cases} h_0 = 5\text{m} & \text{if } x > 1000\text{m} \\ h_1 = 10\text{m} & \text{if } x \le 1000\text{m} \end{cases} \tag{A.4}$$

The dam break problem is solved based on the two-fluid code, in which only liquid phase equations are needed, and the pressure term is set as zero. Figure A-2 and Figure A-3 compare the numerical solution with the analytical solution at $t = 25\text{s}$ and $t = 50\text{s}$ after the dam break, respectively.

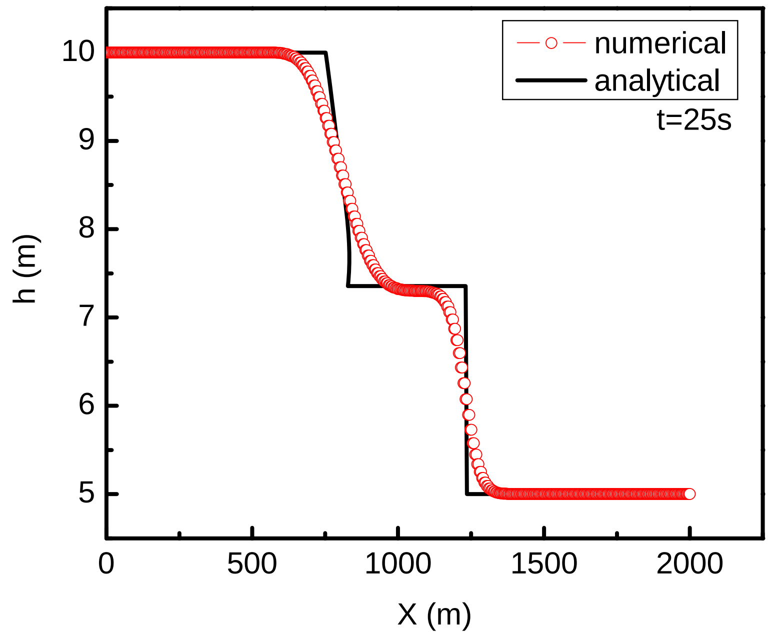

A

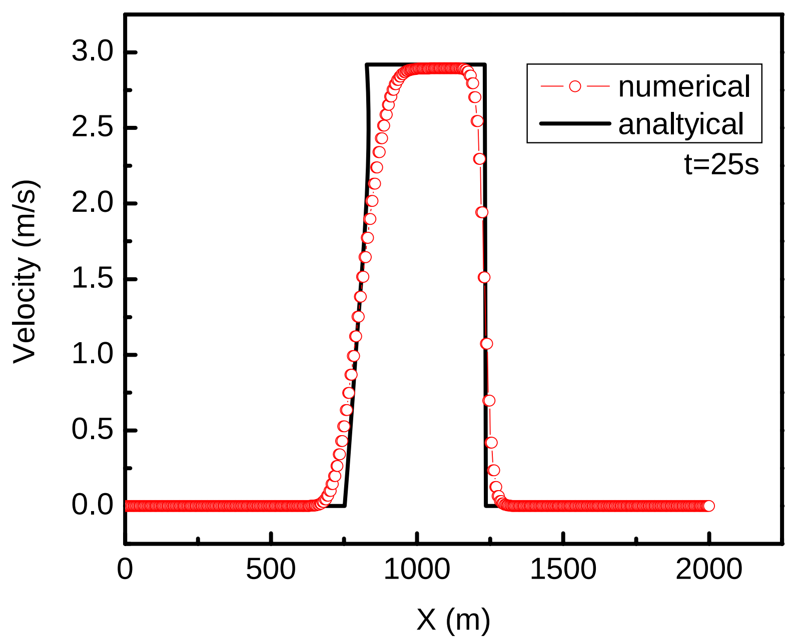

B

Figure A-2. Comparison between numerical results and analytical solutions at 25s after dam break. A) Water depth. B) Water velocity.

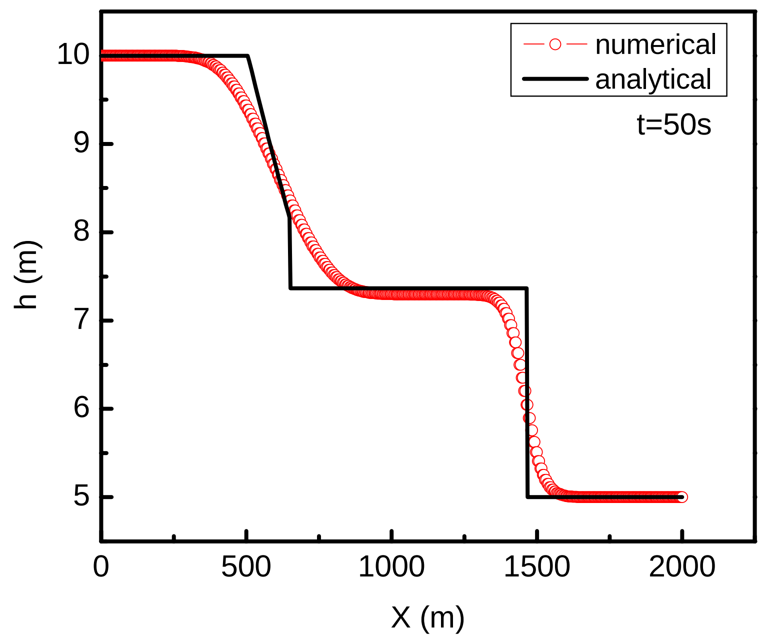

A

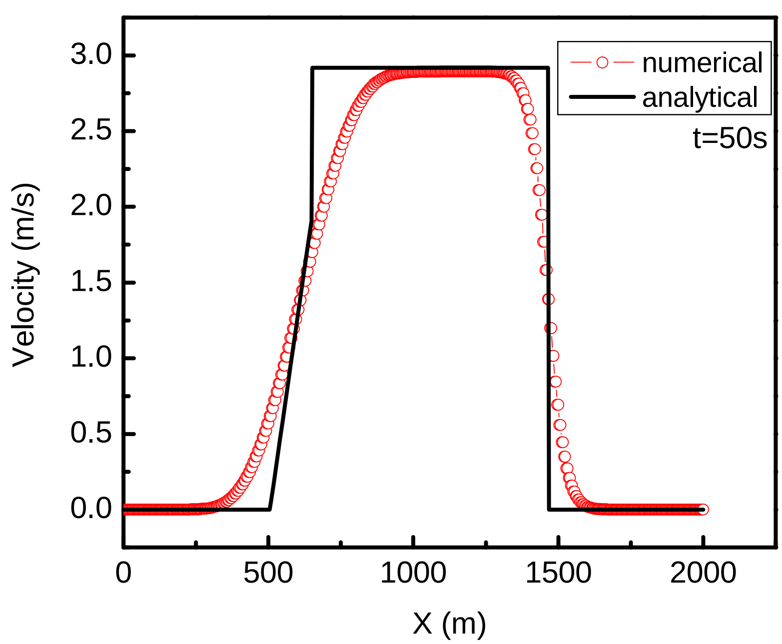

B

Figure A-3. Comparison between numerical results and analytical solutions at 50s after dam break. A) Water depth. B) Water velocity.

After the dam break, the water wave and velocity spread on both directions from the breaking point. The maximum velocity depends on the initial water levels and remains unchanged with time. Due to the numerical dissipation, the sharp changes of the water depth and water velocity are smeared.

Courant number ($CFL = u\dfrac{\Delta t}{\Delta x}$) is an important factor for the transient flow computation. With increasing CFL number the numerical results approaches the analytical solution gradually (Figure A-4). However, the numerical results are unstable for roughly $CFL > 0.7$.

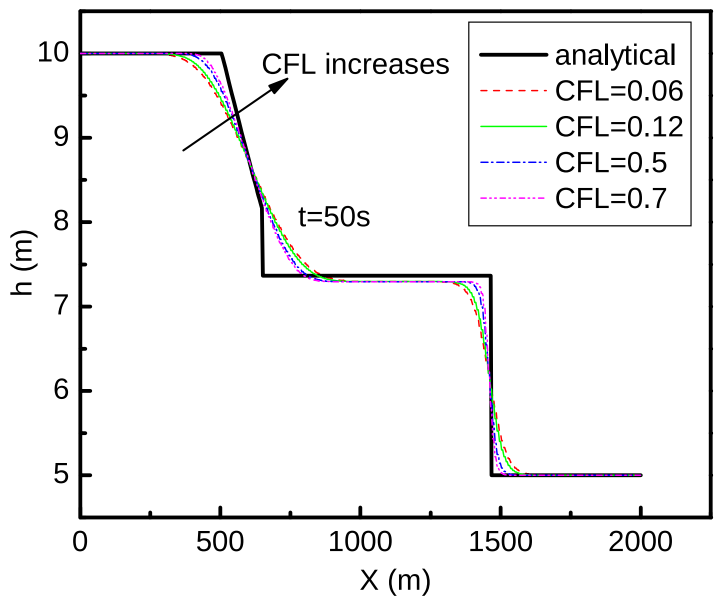

Figure A-4. Effect of CFL number.

A.2 Grid Independence Check

Grid independence of the code is tested for the inverted annular film boiling region with a constant wall temperature under zero-gravity condition. The test section has a dimension of 0.432 cm ID and 70 cm length. At t=0, liquid nitrogen enters the test section with volumetric flow rate of 40cc/s. The liquid nitrogen evaporates while traveling downstream due to the high wall temperature, therefore the void fraction increases along the test section. Three different mesh sizes are used in the computation with total of 200, 400 and 600 grids, respectively.

For a constant time step of $\Delta t = 0.0001$, the computation results of void fraction at t=1 second with different grids show very small difference (Figure A-5). In Figure A-6, the total grid number is fixed at 200 and different CFL number is used in the computation. Again, the resulted void fractions are very close. Therefore, it is believed that current scheme reaches grid independence.

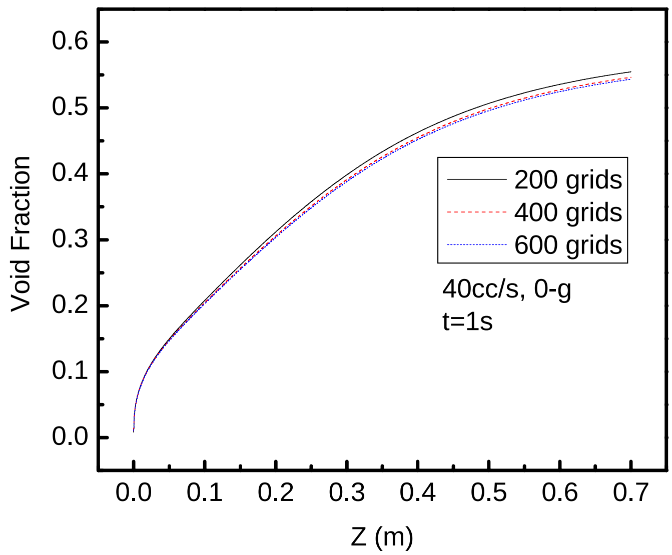

Figure A-5. Computation results of void fraction with different grids at a fixed time step of $\Delta t = 0.0001$.

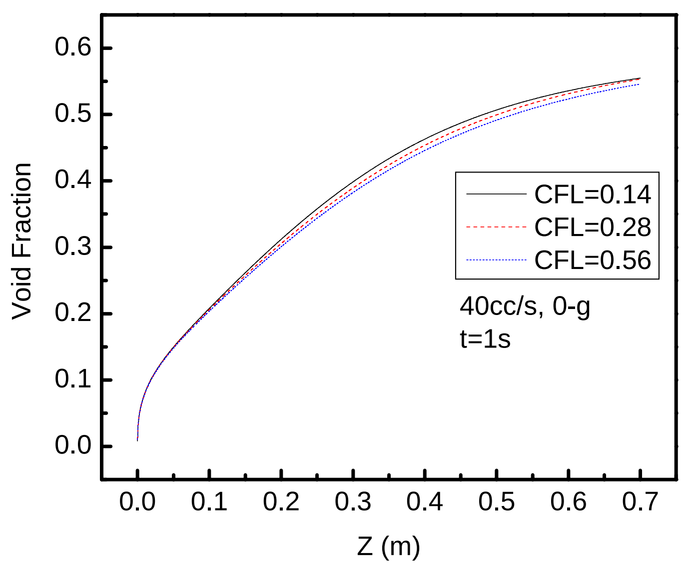

Figure A-6. Computation results of void fraction with different CFL number at a fixed grid number of 200.

LIST OF REFERENCES

Abdul-Razzak, A., Shoukri, M. and Chan, A. M. C., 1992, Rewetting of horizontal tubes. Nuclear Engineering and Design 138, 375-388.

Abdul-Razzak, A., Shoukri, M. and Chan, A. M. C., 1993, Two-fluid modeling of the rewetting and refilling of hot horizontal tubes. The Canadian Journal of Chemical Engineering 71, 358-365.

Adham-Khodaparast, K., Xu, J. J. and Kawaji, M., 1995, Flow film boiling collapse and surface rewetting in normal and reduced gravity conditions. International Journal of Heat and Mass Transfer 38, 2749-2760.

Alipchenkov, V. M., Nigmatulin, R. I., Soloviev, S. L., Stonik, O. G., Zaichik, L. I., and Zeigarnik, Y. A., 2004, A three-fluid model of two-phase dispersed-annular flow. International Journal of Heat and Mass Transfer 47, 5323-5338.

Analytis, G. Th., and Yadigaroglu, G., 1987, Anylytical modeling of inverted annular film boiling. Nuclear Engineering and Design 99, 201-212.

Andreani, M. and Yadigaroglu, G., 1994, Prediction methods for dispersed flow film boiling. International Journal of Multiphase Flow 20 Suppl., 1-51.

Andreani, M. and Yadigaroglu, G., 1996, A 3-d Eulerian-Lagrangian model of dispersed flow film boiling including a mechanistic description of the droplet spectrum evolution I. The thermal-hydraulic model. International Journal of Heat and Mass Transfer 40, 1753-1772.

Antar, B. N. and Collins, F. G., 1997, Flow boiling during quenching in low gravity environment. International Journal of Microgravity Science and Technology 3, 118-128.

Ardron, K. H., 1980, One-dimensional two-fluid equations for horizontal stratified two-phase flow. International Journal of Multiphase Flow 6, 295-304.

Banerjee, S. and Chan, A. M. C., 1980, Separated flow model I: analysis of the averaged and local instantaneous formulations. International Journal of Multiphase Flow 6, 1-24.

Barnea, Y., Elias, E., and Shai, I., 1994, Flow and heat transfer regimes during quenching of hot surfaces. International Journal of Heat and Mass Transfer 37, 1441-1453.

Ben David, M., Zimmels, Y., and Zvirin, Y., 2001a, Determination of the quench velocity and rewetting temperature of hot surfaces. Part I: analytical solution of the micro-scale hydrodynamic model. International Journal of Heat and Mass Transfer 44, 1323-1342.

Ben David, M., Zimmels, Y., and Zvirin, Y., 2001b, Determination of the quench velocity and rewetting temperature of hot surfaces. Part II: an integrated approach of hydrodynamic-thermodynamic micro- and macro-scale models. International Journal of Heat and Mass Transfer 44, 1343-1371.

Berenson, P. J., 1961, Film-boiling heat transfer from a horizontal surface. ASME Journal of Heat Transfer 83, 351-358.

Bergles, A. E. and Jr. Thompson, W. G., 1970, The relationship of quench data to steady-state pool boiling data. International Journal of Heat and Mass Transfer 13, 55-68.

Bolle, L., and Moureau, J. C., 1986, Spray cooling of hot surface. In: Hewitt, G. F., Delhaye, J. M., Zuber, N. (Eds.), Multiphase Science and Technology, Vol.1, Hemisphere Publishing, Washington, DC, 447-456.

Breen, B. P. and Westwater, J. W., 1962, Effect of diameter of horizontal tubes on film boiling heat transfer. Chemical Engineering Progress 58, 67-72.

Brentari, E. G., Giarratano, P. J., and Smith, R.V., 1965, Boiling heat transfer for oxygen, nitrogen, hydrogen, and helium. NBS Technical Note No. 317, National Bureau of Standards.

Brentari, E. G. and Smith, R. V., 1965, Nucleate and film pool boiling design correlatios for O2, N2, H2 and He. Advances in Cryogenic Engineering 10, 325-341.

Bromley, L. A., 1950, Heat transfer in stable film boiling. Chemical Engineering Progress *46*, 221-227.

Bronson, J. C., Edeskuty, F.J., Fretwell, J.H., Hammel, E.F., Keller, W.E., Meier, K.L., Schuch, and A.F, Willis, W.L., 1962, Problems in cool-down of cryogenic systems. Advances in Cryogenic Engineering 7, 198-205.

Burggraf, O. R., 1964, An exact solution of inverse problem in heat conduction theory and application. ASME Journal of Heat Transfer 86, 373-382.

Burke, J. C., Byrnes, W. R., Post, A. H., and Ruccia, F. E., 1960, Pressure cooldown of cryogenic transfer lines. Advances in Cryogenic Engineering 4, 378-394.

Carey, V. P., 1992, Liquid-vapor phase-change phenomena. Taylor & Francis Press, NewYork.

Chan, A. M. C., 1995, Stratified flow film boiling inside horizontal tubes. ASME Journal of Heat Transfer 117, 179-184.

Chan, A. M. C., and Banerjee, S., 1981a, Refilling and rewetting of a hot horizontal tube part I: experiment. ASME Journal of Heat Transfer 103, 281-286.

Chan, A. M. C., and Banerjee, S., 1981b, Refilling and rewetting of a hot horizontal tube part II: structure of a two-fluid model. ASME Journal of Heat Transfer 103, 287-292.

Chan, A. M. C., and Banerjee, S., 1981c. Refilling and rewetting of a hot horizontal tube part III: application of a two-fluid model to analyze rewetting. ASME Journal of Heat Transfer 103, 653-659.

Chang, Y. P., 1959, Wave theory of heat transfer in film boiling. ASME Journal of Heat Transfer 8, 1-12.

Chang, Y. P., and Snyder, N. W., 1960, Heat transfer in saturated boiling. Chemical Engineering Progress, Symp. 56, 25-38.

Chen, J. C., 1966, Correlation for boiling heat transfer to saturated fluids in convective flow. Industry Engineering Chemistry Process Design and Development 5, 322-329.

Chen, J. C., Ozkaynak, F. T. and Sundaram, R. K., 1979, Vapor heat transfer in post-CHF region including the effect of thermodynamic non-equilibrium. Nuclear Engineering and Design 51, 143-155.

Chen, W. J., Lee, Y., and Groeneveld, D. C., 1979, Measurement of boiling curves during rewetting of a hot circular duct. International Journal of Heat and Mass Transfer 22, 973-976.

Cheng, S. C., 1978, Transition boiling curves generated from quenching experiments using a two dimensional model. Letters in Heat and Mass Transfer 5, 391-403.

Cheng, S. C., Ng, W. W. L. and Heng, K. T., 1978, Measurements of boiling curves of subcooled water under forced convective conditions. International Journal of Heat and Mass Transfer 21, 1385-1392.

Cheng, S. C., and Ragheb, H., 1979, Transition boiling data of water on inconel surface under forced convective conditions. International Journal of Multiphase Flow 5, 281-291.

Chi, J. W. H., 1965, Cooldown temperatures and cooldown time during mist flow. Advances in Cryogenic Engineering 10, 330-340.

Chi, J. W. H., and Vetere, A.M., 1964, Two-phase flow during transient boiling of hydrogen and determination of nonequilibrium vapor fractions. Advances in Cryogenic Engineering 9, 243-253.

Chung, J. N., and Olafsson, S. I., 1984, Two-phase droplet flow convective and radiative heat transfer. International Journal of Heat and Mass Transfer 27, 901-910.

Cokmez-Tuzla, A. F., Tuzla, K., and Chen J. C., 2000, Characteristics of liquid-wall contact in post-CHF flow boiling. International Journal of Heat and Mass Transfer 43, 1925-1934.

Collier, J. G., 1981, Convective Boiling and Condensation. 2nd ed., McGraw-Hill, New York.

Cross, M. F., Majumdar, A. K., Bennett Jr., J. C., and Malla, R. B., 2002, Model of chilldown in cryogenic transfer linear. Journal of Spacecraft and Rockets 39, 284-289.

Dhir, V. K., Duffey R. B. and Catton I., 1981, Quenching studies on a zircaloy rod bundle. ASME Journal of Heat Transfer 103, 293-299.

Dougall, R. S., and Rohsenow, W. M., 1963, Film boiling on the inside of vertical tubes with upward flow of the fluid at low qualities. MIT Report 9079-26.

Duffey, R. B. and Porthouse, D. T. C., 1973, The physics of rewetting in water reactor emergency core cooling. Nuclear Engineering and Design 25, 379-394.

Edelman, Z., Naot, D., and Elias, E., 1983, Optical illustration of liquid penetration to the vapor film in inverted annular boiling. International Journal of Heat and Mass Transfer 26, 1715-1717.

Flynn, T. M., 1996, Cryogenic Engineering. Marcel Dekker, Florence, KY.

Frederking, T. H. K., Chapman, R. C., and Wang, S., 1964, Heat transport and fluid motion during cooldown of single bodies to low temperature. Advances in Cryogenic Engineering 10, 353-359.

Ganić, E. N., Rohsenow, W. M., Dispersed flow heat transfer, Intentional Journal of Heat and Mass Transfer 20 (1977) 855-866.

Gebhart, B., Jaluria, Y., Mahajan, R.L., Sammakia, B., 1988, Buoyancy-induced flow and heat transport. Hemisphere Publishing Company.

Groeneveld, D. C.,1975, Post-dryout heat transfer: physical mechanisms and a survey of prediction methods. Nuclear Engineering and Design 32, 283-294.

Groeneveld, D. C., Leung, L. K. H., Vasic, A. Z., Guo, Y. J., and Cheng, S. C., 2003, A look-up table foe fully developed film-boiling heat transfer. Nuclear Engineering and Design 225, 83-97.

Gungor, K.E. and Winterton, R.H.S., 1987, Simplified general correlation for saturated flow boiling and comparisons of correlatios with data. Chemical Engineering Research and Design 65, 148-156.

Guo, Y. J. and Mishima, K., 2002, A non-equilibrium mechanistic heat transfer model for post-dryout dispersed flow regime. Experimental Thermal and Fluid Science 26, 861-869.

Hammouda, N., Groeneveld, D. C., and Cheng, S. C., 1996, An experimental study of subcooled film boiling of refrigerants in vertical up-flow. International Journal of Heat and Mass Transfer 39, 3799-3812.

Hammouda, N., Groeneveld, D. C., and Cheng, S. C., 1997, Two-fluid modeling of inverted annular film boiling. International Journal of Heat and Mass Transfer 40, 2655-2670.

Hedayatpour, A., Antar, B. N., and Kawaji, M., 1993, Cool-down of a vertical line with liquid nitrogen. AIAA Journal of Thermophysics and Heat Transfer 7, 426-434.

Hsu, Y. Y. and Graham, R. W., 1963, A visual study of two-phase flow in a vertical tube with heat addition. NASA-TN-1564.

Hsu, Y. Y., and Westwater, W., 1959, Approximate theory for film boiling on vertical surfaces. AIChE Symposium Series 56, 15-24.

Iloeje, O. C., Plummer, D. N., Rohsenow, W. M. and Griffith, P., 1975, An investigation of the collapse and surface rewet in film boiling in forced vertical flow. ASME Journal of Heat Transfer 42, 3387-3407.

Iloeje, O. C., Plummer, D. N., Rohsenow, W. M., Griffith, P., 1982, Effects of mass flux, flow quality, thermal and surface properties of materials on rewet of dispersed flow film boiling. ASME Journal of Heat Transfer 104, 304-308.

Incropera, F. P., and Dewitt, D. P., 2002, Fundamentals of heat and mass transfer, 5th edition. John Wiley & Sons, New York.

Ishii, M., 1975, Thermo-fluid dynamic theory of two-phase flow. Eyrolles, Paris.

Ishii, M., and Dejarlais, G., 1986, Flow regime transition and interfacial characteristics of inverted annular flow. Nuclear Engineering and Design 95, 171-184.

Ishii, M., and Dejarlais, G., 1987, Flow visualization study of inverted annular flow of post dryout heat transfer region. Nuclear Engineering and Design 99, 187-199.

Ishii, M. and Mishima, K., 1984, Two-fluid model and hydrodunamic constitutive relations. Nuclear Engineering and Design 82, 107-126.

Issa, R. I., and Kempf, M. H. W., 2003, Simulation of slug flow in horizontal and nearly horizontal pipes with the two-fluid model. International Journal of Multiphase Flow 29, 69-95.

Kalinin, E. K., Yarko, S. A., Yskochelaev, V., and Berlin, I. I., 1969, Investigation of the crisis in film boiling in channels. Proceedings of Two Phase Flow and Heat Transfer in Rod Bundles, ASME Winter Annual Meeting, Los Angeles, CA, 89-94.

Kandlikar, S.G., 1990, A general correlation for saturated two-phase flow boiling heat transfer inside horizontal and vertical tubes. ASME Journal of Heat Transfer 112, 219-228.

Kao, H. S., Morgan, C. D., Crawford, M., and Jones, J. B., 1972, Stability analysis of film boiling. AIChE Symposium Series 68, 147-155.

Kataoka, I., and Ishii, M., 1983, Entrainment and deposition rates of droplets in annular two-phase flow. Proceedings of ASME/JSME Thermal Engineering Joint Conference, Vol. 1.

Kataoka, I., Ishii, M., and Mishima, K., 1983, Generation and size distribution of droplet in annular two-phase flow. ASME Journal of Fluid Engineering 105, 230-238.

Kawaji, M. and Banerjee, S., 1987, Application of a multifield model to reflooding of a hot vertical tube part I: model structure and interfacial phenomena. ASME Journal of Heat Transfer 109, 204-211.

Kawaji, M. and Banerjee, S., 1988, Application of a multifield model to reflooding of a hot vertical tube part II: analysis of experimental results. ASME Journal of Heat Transfer 110, 710-720.

Kawaji, M., Ng, Y.S., Banerjee, S., and Yadigaroglu, G., 1985, Reflooding with steady and oscillatory injection: Part I-flow regimes, void fraction, and heat transfer. ASME Journal of Heat Transfer 107, 670-678.

Kawaji, M., Westbye, C. J. and Antar, B. N., 1991, Microgravity experiments on two-phase flow and heat transfer during quenching of a tube and filling of a vessel. AIChE Symposium Series 87, 236-243.

Kays, W. M., 1993, Convective Heat and Mass Transfer. 3rd ed., McGraw-Hill, New York.

Kim, J. and Moin, P., 1985, Application of a fractional step method to incompressible Navier-Stokes equation. Journal of Computational Physics 59, 308-323.

Klimenko, V.V., Fyodorov, M.V. and Fomichyov, Yu. A., 1989, Channel orientation and geometry influence on heat transfer with two-phase forced flow of nitrogen. Cryogenics 29, 31-36.

Kline, S. J. and McClintock, F. A., 1953, Describing uncertainties in single sample experiments. Mechanical Engineering 75, 3-8.

Koizumi, Y., Ueda, T., and Tanaka, H., 1978, Post dryout heat transfer to R-113 upward flow in a vertical tube, International Journal of Heat and Mass Transfer 22, 669-678.

Kutateladze, S.S., 1948, On the transition to film boiling under natural convection, Kotloturbostroenie 3, 10.

Kutateladze, S.S., 1952, Heat transfer in condensation and boiling. State Sci. and Tech. Pub. Of Lit. on Machinery, Moscow (Atomic Energy Commission Translation 3770, Tech. Info Service, Oak Ridge, Tennessee.)

Laverty, W. F., and Rohsenow, W. M., 1967, Film boiling of saturated nitrogen flowing in a vertical tube. ASME Journal of Heat Transfer 91, 90-98.

Lee, K., and Ryley, D. J., 1968, The evaporation of water droplets in superheated steam. ASME Journal of Heat Transfer 90, 445-451.

Lee, Y., and Kim, K. H., 1987, Inverted annular-flow boiling. International Journal of Multiphase Flow 13, 345-355.

Liao, J., 2005, Modeling two-phase transport during cryogenic chilldown in a pipeline. Ph.D. dissertation, University of Florida.

Lin C-S, Van Dresar, N. T., and Hasan, M. M., 1991, A pressure control analysis of cryogenic storage systems. NASA TM 104409.

Merte, Jr., H., and Clark, J. A., 1964, Boiling heat transfer with cryogenic fluids at standard, fractional, and near-zero gravity. ASME Journal of Heat Transfer 86C, 315-319.

Nelson, R., and Unal, C., 1992, A phenomenological model of the thermal hydraulics of convective boiling during the quenching of hot rod bundles, Part I: thermal hydraulic model. Nuclear Engineering and Design 136, 277-298.

Noyes, R. C.,1963, An experimental study of sodium pool boiling heat transfer. ASME Journal of Heat Transfer 85, 125-132.

Obot, N. T., and Ishii, M., 1988, Two-phase flow regime transition criteria in post-dryout region based on flow visulazation experiments. International Journal of Heat and Mass Transfer 31, 2559-2570.

Ozisik, M. N, 1993, Heat Conduction, 2nd Edition. John Wiley & Sons, New York.

Ozisik, M. N and Orlande, H. R. B., 2000, Inverse Heat Transfer. Taylor and Francis, New York.

Piggott, B. D. G. and Porthouse, D. T. C., 1975, A correlation of rewetting data. Nuclear Engineering and Design 32, 171-181.

Raithby, G. D., and Hollands, K. G. T., 1975, A general method of obtaining approximate solutions to laminar and turbulent free convection problems. Advances in Heat Transfer, 11, 265-315, Academic Press, New York.

Rowe, P. N., 1961, Drag forces in a hydraulic model of a fluidised bed, part II. Transactions of the Institute of Chemicals Engineers 39, 175-180.

Seader, J. D., Miller, W. S., and Kalvinskas, L.A., 1965, Boiling heat transfer for cryogenics. NASA Contractor Report CR-243.

Shah, M. M., 1984, Prediction of heat transfer during boiling of cryogenic fluids flowing in tubes. Cryogenics 24, 231-236.

Shah, M. M. and Siddiqui, M. A., 2000, A general correlation for heat transfer during dispersed-flow film boiling in tubes. Heat Transfer Engineering 21, 18-32.

Simon, F. F., and Simoneau, R. J., 1969, Transition from film to nucleate boiling in vertical forced flow. ASME Paper, No. 69-HT-26.

Snyder, T. J., 1993, WSU 2.1 second microgravity drop tower design, construction, and performance. Master thesis, Washington State University.

Spiegler, P., Hopenfeld, J., Silberberg, M., Jr. Bumpus, C. F., and Norman, A., 1963, Onset of stable film boiling and the foam limit. International Journal of Heat and Mass Transfer 6, 987-989.

Steward, W. G., Smith and R. V., Brennan, J.A., 1970, Cooldown transients in cryogenic transfer lines. Advances in Cryogenic Engineering 15, 354-363.

Sun, K. H., Dix, G. E., Tien, C. L., 1974, Cooling of a very hot vertical surface by a falling liquid film. ASME Journal of Heat Transfer, Transaction of ASME 96, 126-131.

Sun, K. H., Gonzalez-Santalo, J. M., and Tien, C. L., 1976, Calculations of combined radiation and convection heat transfer in rod bundles under emergency cooling conditions. ASME Journal of Heat Transfer 98, 414-420.

Swanson, C. J., Donnelly, R. J., and Ihas, G. G., 2000, Turbulent pipe flow of He I and He II. Physica B 284-288, 77-78.

Taitel, Y and Dukler, A. E., 1976, A model for predicting flow regime transitions in horizontal and near horizontal gas-liquid flow. AIChE Journal 22, 47-55.

Takenaka, N., Fujii, T., Akagawa, K., and Nishida, K, 1989, Flow pattern transition and heat-transfer of inverted annular-flow. International Journal of Multiphase Flow 15, 767-785.

Thome, J. R. and Hajal, J. E., 2003, Two-phase flow pattern map for evaporation in horizontal tubes: Latest version. Heat Transfer Engineering 24, 3-10.

Thompson, T. S., 1972, An analysis of the wet-side heat-transfer coefficient during rewetting of a hot dry patch. Nuclear Engineering and Design 22, 212-224.

Thompson, T. S., 1974, Process of rewetting a hot surface by a falling liquid –film. Nuclear Engineering and Design 31, 234-245.

Tian, W. X., Qiu, S. Z., and Jia D. N., 2006, Investigations on post-dryout heat transfer in bilaterally heated annular channels. Annals of Nuclear Energy 33, 189-197.

Tien, C. L., and Yao, L. S., 1975, Analysis of conduction-controlled rewetting of a vertical surface. ASME Journal of Heat Transfer 97, 161-165.

Van Dresar, N. T. and Siegwarth, J. D., 2001, Near-horizontal, two-phase flow patterns of nitrogen and hydrogen at low mass and heat flux. NASA TP 2001-210380.

Van Dresar, N.T., Siegwarth, J.D., and Hasan, M.M., 2002, Convective heat transfer coefficients for near-horizontal two-phase flow of nitrogen and hydrogen at low mass and heat flux. Cryogenics 41, 805-811.

Velat, C., 2004, Experiments in cryogenic two phase flow. Master thesis, University of Florida.

Westbye, C. J., Kawaji, M., and Antar B.N., 1995, Boiling heat transfer in the quenching of a hot tube under microgravity. AIAA Journal of Thermophysics and Heat Transfer 9, 302-307.

Wright, C. C., and Walters, H. H., 1959, Single tube heat transfer tests, gaseous and liquid hydrogen. WADC Technical Report 59, 423.

Xu, J. J., 1998, Flow boiling heat transfer in the quenching of a hot surface under reduced gravity conditions. Ph.D. dissertation, University of Toronto.

Xu, J. L., Wong, T. N., and Huang, X. Y., 2006, Two-fluid modeling for low-pressure subcooled flow boiling. International Journal of Heat and Mass Transfer 49, 377-386.

Yadigaroglu, G., 1978, The reflooding phase of the LOCA in PWRs. Part I: core heat transfer and fluid flow. Nuclear Safety 19, 20-36.

Yadigaroglu, G., Nelson, R. A., Teschendorff, V., Murao, Y., Kelly, J., and Bestion, D., 1993, Modeling of reflooding. Nuclear Engineering and Design 145, 1-35.

Yamanouchi, A., 1968, Effect of core spray cooling in transient state after loss of coolant accident. Journal of Nuclear Science and Technology 5, 547-558.

Yang, L., and Zhang, C-L., 2005, Two-fluid model of refrigerant two-phase flow through short tube orifice. International Journal of Refrigeration 28, 419-427.

Zivi, S. M., 1964, Estimation of steady state steam void-fraction by means of the principle of minimum entropy production. ASME Journal of Heat Transfer 86, 247–252.

Zoppou, C., and Roberts, S., 2003 Explicit schemes for dam-break simulations. Journal of Hydraulic Engineering 129, 11-34.

Zuber, N., 1958, On stability of boiling heat transfer, Transaction of ASME 80, 711-720.

Zuber, N., 1959, Hydrodynamic aspects of boiling heat transfer. Ph.D. dissertation, UCLA.

BIOGRAPHICAL SKETCH

Kun Yuan was born in Chongqing, China, on December 24, 1976. After receiving his Bachelor of Science in air-conditioning and refrigeration from the University of Science and Technology of China in 1999, he received a Master of Science degree in cryogenic engineering and refrigeration from the Chinese Academy of Sciences in 2002. In pursuit of a Ph.D. degree in mechanical engineering, Kun Yuan began his studies at the University of Florida in August 2002.